

Lars Olav Skrebergene

# Optimization and fabrication of a fiber-to-waveguide silicon-on-insulator grating coupler

Master's thesis in Nanotechnology

Supervisor: Astrid Aksnes

February 2020



Lars Olav Skrebergene

# **Optimization and fabrication of a fiber-to-waveguide silicon-on-insulator grating coupler**

Master's thesis in Nanotechnology

Supervisor: Astrid Aksnes

February 2020

Norwegian University of Science and Technology

Faculty of Information Technology and Electrical Engineering

Department of Electronic Systems



Norwegian University of  
Science and Technology





# Problem description

Optical fibers are able to confine and transport light across large distances with only minor losses, and waveguides provide similar features for integrated photonic devices. A major challenge, however, is to transfer light efficiently between these two structures. It is particularly difficult to couple light from an optical fiber to a single-mode waveguide due to a large mode-mismatch and a much smaller cross-sectional area.

The goal of this master's thesis is to optimize and fabricate a silicon-on-insulator (SOI) grating coupler that enables fiber-to-waveguide coupling with as high efficiency as possible. The grating coupler will be designed to be compatible with the lab-on-a-chip biosensing device currently being developed by the photonic research group at the Norwegian University of Science and Technology (NTNU).

Simulations will primarily be used to design and optimize grating couplers, and the most promising results will be verified by fabrication and characterization of physical prototypes. COMSOL Multiphysics is chosen as the main simulation platform, and all simulations will be limited to two dimensions to reduce memory and processing power requirements. Both simple uniform grating structures and more complex apodized structures will be examined in the simulations.

All fabrication will take place in the NTNU Nanolab cleanroom, and many different tools and instruments will be employed for nanofabrication. These include plasma-enhanced chemical vapor deposition (PECVD), electron-beam lithography (EBL) and inductively coupled plasma reactive-ion etching (ICP-RIE). Optical microscopy and scanning electron microscopy (SEM) will also be used for characterization purposes, in addition to a laser-based coupling measurement setup.



# Abstract

The development of miniaturized laboratory systems has become an important area of research for integrated photonics in recent years. Many of these systems are based on light-modulating structures that require sufficient amounts of light to function optimally. Unfortunately, significant losses are also associated with the process of coupling light into these structures. Since the use of high-intensity laser sources both increases production costs and has the potential to damage integrated structures, it is important to optimize coupling techniques such that low-intensity light sources can be used.

In this master's thesis, silicon-on-insulator grating couplers are examined through the use of COMSOL Multiphysics – a physics simulation software based on the finite-element method. Both uniform and apodized grating structures are considered, and optimizations are done to maximize the coupling efficiency between a single-mode optical fiber with a  $8.2\ \mu\text{m}$  core diameter and a strip waveguide featuring a  $220\ \text{nm} \times 500\ \text{nm}$  cross-section. All optimizations are done for TE-polarized light with a  $1550\ \text{nm}$  wavelength, and coupling efficiencies of 44 % and 62 % were demonstrated for uniform and apodized grating couplers, respectively.

Uniform grating coupler prototypes are fabricated using plasma-enhanced chemical vapor deposition (PECVD), electron-beam lithography (EBL) and inductively coupled plasma reactive-ion etching (ICP-RIE) techniques. Crystalline silicon wafer substrates with a  $1\ \mu\text{m}$  layer of thermally grown silica are used as starting points for the fabrication process and the highest coupling efficiency demonstrated for fabricated grating couplers is 19 %.



# Sammendrag

(Norwegian translation of the abstract)

Utviklingen av miniaturiserte laboratoriesystemer har blitt et viktig forskningsområde innen integrert fotonikk de siste årene. Mange av disse systemene baserer seg på lysmodulerende strukturer som krever tilstrekkelig med lys for å fungere optimalt. Betydelige tap er dessverre også assosiert med prosessen der lys kobles inn i disse strukturene. Siden bruken av høyintensitetslasere øker produksjonskostnader og potensielt også kan skade integrerte strukturer, er det viktig å optimalisere koblingsteknikker slik at lyskilder med lav intensitet kan benyttes.

I denne masteroppgaven blir silisium-på-isolator-baserte optiske gitterkoblinger undersøkt ved hjelp av COMSOL Multiphysics – en programvare som utfører fysikksimuleringer ved bruk av elementmetoden. Både uniforme og apodiserte strukturer blir betraktet, og optimaliseringer blir gjort for å maksimere koblingseffektiviteten mellom en singelmodusfiber med en  $8.2\ \mu\text{m}$  kjerne-diameter og en rektangulær stripebølgeleder med et  $220\ \text{nm} \times 500\ \text{nm}$  tverrsnitt. Alle optimaliseringer blir gjort for TE-polarisert lys med  $1550\ \text{nm}$  bølgelengde, og koblingseffektiviteter på henholdsvis 44 % og 62 % blir demonstrert for uniforme og apodiserte optiske gitterkoblinger.

Uniforme optiske gitterkoblinger blir også laget på et laboratorium ved bruk av teknikker som plasma-forsterket kjemisk dampavsetning fra gassfase (PECVD), elektronstrålelitografi og induktivt koblet plasma-basert reaktiv ione-etsing (ICP-RIE). Krystallinske silisiumsubstrater med et  $1\ \mu\text{m}$  tykt lag av termisk grodd silisiumdioksid blir brukt som utgangspunkter for fabrikkasjonsprosessen, og den høyeste koblingseffektiviteten som blir demonstrert for de tilvirkede strukturene er 19 %.



# Preface

This thesis is submitted as the finalization of the author's degree of Master of Science in Nanotechnology at the Department of Electronic Systems (IES) at the Norwegian University of Science and Technology (NTNU).

The work presented here is a continuation of a 15 ECTS specialization project completed in June 2019 [1], which focused on the design and optimization of a simulated uniform grating coupler. This preliminary project forms a basis for many of the designs explored here, and its theory chapter is also repeated here with minor changes.

Fabrication procedures followed in this thesis build on previous work by other members of the photonic research group at NTNU [2–5] for compatibility reasons. However, all results and material presented here are in its entirety the work of the author.





# Acknowledgements

I would first and foremost like to thank my supervisor, Astrid Aksnes, as well as my co-supervisors, Jong Wook Noh and Mukesh Yadav, for their invaluable help throughout my work with this thesis. They have all provided excellent advice and gone out of their way to assist me in any way they could, and for that I am forever grateful.

In addition, I would also like to thank:

- NTNU Nanolab and all its staff for offering equipment training and guidance whenever I had any questions about the cleanroom or its instruments.
- My wife, Ingerid Gjeitnes Hellen, for her exceptional proof-reading skills and for being a constant beacon of love, support and encouragement.
- The student association of the Nanotechnology study program, Timini, and all its members, for organizing countless events and activities and making my time in Trondheim very enjoyable.
- My parents, Lill Iren Johansen and Tom Skrebergene, as well as the rest of my family, for always being there for me and supporting me through all my endeavours.



## List of abbreviations

<b>2D</b>	Two-dimensional
<b>3D</b>	Three-dimensional
<b>a-Si</b>	Amorphous silicon
<b>c-Si</b>	Crystalline silicon
<b>CAD</b>	Computer aided design
<b>CIF</b>	Caltech Intermediate Format
<b>CMOS</b>	Complimentary metal-oxide-semiconductor
<b>CRT</b>	Cathode-ray tube
<b>CVD</b>	Chemical vapor deposition
<b>DI</b>	Deionized
<b>EBL</b>	Electron-beam lithography
<b>ECTS</b>	European Credit Transfer and Accumulation System
<b>EDS</b>	Energy-dispersive X-ray spectroscopy
<b>FDM</b>	Finite-difference method
<b>FIB</b>	Focused ion beam
<b>FEM</b>	Finite-element method
<b>FVM</b>	Finite-volume method
<b>HMDS</b>	Hexamethyldisilane
<b>ICP-RIE</b>	Inductively coupled plasma reactive-ion etching
<b>IES</b>	Department of Electronic Systems
<b>IPA</b>	Isopropyl alcohol
<b>LHS</b>	Left-hand side
<b>LOC</b>	Lab-on-a-chip
<b>MFD</b>	Mode-field diameter
<b>NA</b>	Numerical aperture
<b>NTNU</b>	Norwegian University of Science and Technology
<b>PDE</b>	Partial differential equation
<b>PEB</b>	Post-exposure bake
<b>PEC</b>	Proximity error correction
<b>PECVD</b>	Plasma-enhanced chemical vapor deposition
<b>PML</b>	Perfectly matched layer
<b>RF</b>	Radio frequency
<b>RHS</b>	Right-hand side
<b>RPM</b>	Rotations per minute
<b>SEM</b>	Scanning electron microscopy
<b>SOI</b>	Silicon-on-insulator

<b>TE</b>	Transverse-electric
<b>TEM</b>	Transverse-electromagnetic
<b>TM</b>	Transverse-magnetic
<b>VBA</b>	Visual Basic for Applications

# Contents

<b>Problem description</b>	<b>i</b>
<b>Abstract</b>	<b>iii</b>
<b>Sammendrag</b>	<b>v</b>
<b>Preface</b>	<b>vii</b>
<b>Acknowledgements</b>	<b>ix</b>
<b>List of abbreviations</b>	<b>xi</b>
<b>Contents</b>	<b>1</b>
<b>1 Introduction</b>	<b>4</b>
<b>2 Theory</b>	<b>6</b>
2.1 Guided-wave optics . . . . .	6
2.1.1 Light at an interface . . . . .	6
2.1.2 Planar dielectric waveguide . . . . .	8
2.1.3 Modes . . . . .	8
2.2 Waveguides . . . . .	10
2.2.1 Square waveguides . . . . .	10
2.2.2 Channel waveguides . . . . .	12
2.2.3 Optical fiber waveguides . . . . .	13
2.2.3.1 Field distribution in an optical fiber . . . . .	15
2.3 Coupling . . . . .	17
2.3.1 Butt coupling . . . . .	18
2.3.2 Top coupling . . . . .	18
2.3.3 Prism coupling . . . . .	20
2.3.4 Grating coupling . . . . .	20
2.3.5 Taper coupling . . . . .	21
2.4 Simulation techniques . . . . .	22
2.4.1 Finite element method . . . . .	22
2.4.2 Simplification to two dimensions . . . . .	23
2.4.2.1 Effective index method . . . . .	23
2.5 Electrical wave equation . . . . .	23

<b>3</b>	<b>Tools and procedures</b>	<b>25</b>
3.1	Simulation tools . . . . .	25
3.1.1	COMSOL Multiphysics . . . . .	25
3.1.2	MATLAB . . . . .	26
3.1.3	Model description . . . . .	26
3.1.3.1	Geometry and materials . . . . .	28
3.1.3.2	Ports . . . . .	29
3.1.3.3	Modeling the optical fiber . . . . .	31
3.2	Simulation procedures . . . . .	31
3.2.1	Meshing . . . . .	32
3.2.2	Gaussian beam diameter . . . . .	32
3.2.3	Uniform grating coupler . . . . .	33
3.2.4	Apodized grating coupler . . . . .	34
3.3	Experimental tools . . . . .	37
3.3.1	The silicon-on-insulator platform . . . . .	37
3.3.2	Plasma-enhanced chemical vapor deposition . . . . .	38
3.3.3	Scriber . . . . .	38
3.3.4	Ultrasonic bath . . . . .	39
3.3.5	Plasma cleaner . . . . .	40
3.3.6	Electron-beam lithography . . . . .	40
3.3.6.1	Vapor prime . . . . .	41
3.3.6.2	Spin coat . . . . .	41
3.3.6.3	Soft bake . . . . .	41
3.3.6.4	Alignment and exposure . . . . .	41
3.3.6.5	Post-exposure bake . . . . .	43
3.3.6.6	Development . . . . .	43
3.3.6.7	Hard bake . . . . .	43
3.3.6.8	Develop inspect . . . . .	43
3.3.7	Inductively coupled plasma reactive-ion etching . . . . .	43
3.4	Experimental procedures . . . . .	44
3.4.1	Thin film deposition . . . . .	46
3.4.2	Scribing . . . . .	46
3.4.3	Design preparation . . . . .	47
3.4.4	Application of resist . . . . .	47
3.4.5	Exposure . . . . .	48
3.4.5.1	Dose testing . . . . .	49
3.4.5.2	Grating coupler fabrication . . . . .	49
3.4.6	Development . . . . .	50
3.4.7	Etching . . . . .	50
3.4.8	Resist removal . . . . .	51
3.5	Characterization tools . . . . .	51
3.5.1	Optical microscopy . . . . .	51
3.5.2	Scanning electron microscopy . . . . .	52
3.5.3	Laboratory setup for coupling efficiency measurements . . . . .	53
3.6	Characterization procedures . . . . .	53
3.6.1	Resist and sample quality . . . . .	55

3.6.2	Dose tests . . . . .	55
3.6.3	Coupling efficiency . . . . .	56
<b>4</b>	<b>Results and discussion</b>	<b>57</b>
4.1	Simulation results . . . . .	57
4.1.1	Meshing . . . . .	57
4.1.2	Gaussian beam diameter . . . . .	58
4.1.3	Uniform grating coupler . . . . .	59
4.1.3.1	Wavelength and incidence angle . . . . .	59
4.1.3.2	Wavelength and grating dimensions . . . . .	61
4.1.4	Apodized grating coupler . . . . .	62
4.2	Fabrication results . . . . .	65
4.2.1	Resist and sample quality . . . . .	65
4.2.2	Dose tests . . . . .	65
4.2.3	Coupling efficiency . . . . .	71
4.3	Comparison: simulation and fabrication . . . . .	76
<b>5</b>	<b>Summary and conclusion</b>	<b>79</b>
5.1	Simulation . . . . .	79
5.2	Fabrication . . . . .	80
5.3	Future research . . . . .	80
5.4	Conclusion . . . . .	81
<b>A</b>	<b>Tutorial: COMSOL Multiphysics</b>	<b>82</b>
A.1	Initial setup . . . . .	82
A.2	Parameters . . . . .	83
A.3	Geometry . . . . .	84
A.4	Materials . . . . .	86
A.5	Perfectly matched layer . . . . .	86
A.6	Physics interface . . . . .	87
A.7	Meshing . . . . .	89
A.8	Study configuration . . . . .	90
A.9	Simulation and results . . . . .	91
A.10	Tips and tricks . . . . .	91
A.10.1	Automated domain and boundary assignment . . . . .	91
A.10.2	Interfacing with third-party software . . . . .	92
<b>B</b>	<b>Matlab code</b>	<b>93</b>
B.1	Analysis of line widths in SEM images . . . . .	93
	<b>References</b>	<b>97</b>

# Chapter 1

## Introduction

Over the course of the last few centuries our knowledge of medicine has improved tremendously. New pharmaceutical remedies have been developed, and modern tests and imaging techniques have augmented our diagnostic capabilities. One of the more recent trends is the development of miniaturized laboratory systems that can be used for portable and cheap measurements both in hospital settings and in the comfort of our own homes. These devices are often referred to as lab-on-a-chip (LOC) devices and can be designed for a wide range of applications. A typical example is the measurement of blood glucose levels in patients diagnosed with diabetes [6].

The photonics research group at the Norwegian University of Science and Technology (NTNU) is currently in the process of developing a LOC sensor that can measure concentrations in a large variety of fluids [2-4]. The device is primarily intended for biosensing applications and is based on photonic crystal structures, ring resonators and interferometer structures that modulate an optical input signal. The surface of these structures are functionalized to interact chemically with the substance we want to measure the concentration of, which causes a refractive index change that alters the way light is modulated. This allows concentrations to be determined by analyzing the optical output signal. The LOC device features narrow single-mode waveguides that are connected to the aforementioned structures, but it is challenging to couple light efficiently into the waveguide because of its submicron dimensions.

The accuracy of the sensor measurements is highly dependent on the intensity of the output. Since significant losses are associated with the light modulation, it is important that sufficient light is provided to the input port of the device. High-intensity laser sources could easily cause damage to small LOC structures, and it is therefore preferable to find an efficient way to transfer low-intensity light into the waveguide integrated on the device.

The research group at NTNU is currently using a laser source transmitted through an optical fiber, but a problem is that there is a large mismatch between the dimensions of the waveguide and the fiber. The waveguide has a rectangular  $220 \text{ nm} \times 500 \text{ nm}$  cross-section, while the fiber is cylindrical with a core radius of  $8.2 \mu\text{m}$ . This results in very high losses, since only a small fraction of the laser light enters the waveguide with the currently used butt coupling



techniques. Similar challenges also exist in other applications involving small optical structures.

The main focus of this master's thesis is to optimize and fabricate a grating structure that improves the coupling efficiency between the optical fiber and the waveguide. To ensure compatibility with the LOC sensor, the structure will be made using silicon-on-insulator (SOI) technology. Manufacturing complexity will also be taken into account, since it is important to keep production costs low.

The fundamentals of waveguides, coupling structures and simulation techniques will be covered in chapter 2, before we move on to describe the tools, methods and procedures that have been employed to simulate, fabricate and characterize our grating structures in chapter 3. Chapter 4 will be devoted to the presentation of our results and a detailed discussion of their validity and significance. A summary of this thesis will then be provided in chapter 5, which will culminate in our final conclusion.

To make it easier for other researchers to reproduce the results presented in this thesis, a detailed tutorial is provided in appendix A which demonstrates how a uniform grating coupler can be designed and simulated using COMSOL Multiphysics. One of the scripts we have used to analyze the width of lines imaged using scanning electron microscopy (SEM) is also provided in appendix B.

## Chapter 2

# Theory

In order to improve our understanding of the problem at hand, this chapter will provide the necessary theoretical background to describe relevant waveguide structures, coupling and simulation techniques. We will start by examining how light behaves at a dielectric interface in section 2.1, and from there expand our theory to explain the working principles of waveguides and modes. In section 2.2 we will examine different types of waveguides and study the case of an optical fiber.

We then shift our focus to the transfer of light between an optical fiber and a waveguide in section 2.3. Different coupling schemes will be considered before we look at the working principles of the grating coupler. In section 2.4 we will also briefly discuss the finite element method and how it connects numerical simulations to the physics that govern optical structures.

### 2.1 Guided-wave optics

#### 2.1.1 Light at an interface

Fermat's principle is a postulate of ray optics stating that *light rays travel along the path of least time* [7]. From this fundamental principle one can determine how light rays will behave when incident on the interface between two isotropic media. It turns out that the angle of refraction  $\theta_2$  can be easily calculated from the angle of incidence  $\theta_1$  and the refractive indices of the two materials. The relation is called Snell's law, and is given by

$$n_1 \sin \theta_1 = n_2 \sin \theta_2. \quad (2.1)$$

$n_1$  is here the refractive index of the medium in which the light is propagating and  $n_2$  is the refractive index of the medium the light ray is incident on [7, 8].

When a beam of light is incident on such an interface, it is usually partially transmitted and partially reflected. Due to phase matching conditions at the interface, the reflected angle will be the same as the incident angle,  $\theta_3 = \theta_1$ . The transmitted beam will transverse the interface and continue propagating at the angle of refraction  $\theta_2$ .

The fraction of light that is reflected and transmitted is dependent on its polarization. If the electric field is orthogonal to the plane of incidence, we call

it transverse-electric (TE) polarization, while it is called transverse-magnetic (TM) polarization if it is the magnetic field that has this orthogonality. All electromagnetic radiation consists of a combination of TE- and TM-polarized components. The reflectance and transmission coefficients are given by the Fresnel equations [7, 9],

$$r_{\text{TE}} = \frac{n_1 \cos \theta_1 - n_2 \cos \theta_2}{n_1 \cos \theta_1 + n_2 \cos \theta_2} \quad (2.2a)$$

$$t_{\text{TE}} = \frac{2n_1 \cos \theta_1}{n_1 \cos \theta_1 + n_2 \cos \theta_2} \quad (2.2b)$$

$$r_{\text{TM}} = \frac{n_2 \cos \theta_1 - n_1 \cos \theta_2}{n_2 \cos \theta_1 + n_1 \cos \theta_2} \quad (2.3a)$$

$$t_{\text{TM}} = \frac{2n_1 \cos \theta_1}{n_2 \cos \theta_1 + n_1 \cos \theta_2} \quad (2.3b)$$

The total power reflectance  $\mathcal{R}$  is given by the absolute square of the relevant reflection coefficient,  $|r|^2$ . The total power transmittance is given by  $\mathcal{T} = 1 - \mathcal{R}$ . In general,  $\mathcal{T}$  is not equal to  $|t|^2$ , as the two media have different impedances and the transmitted beam travels at a different angle [7]. Accounting for both these effects, it can be shown that

$$\mathcal{T} = \frac{n_2 \cos \theta_2}{n_1 \cos \theta_1} |t|^2. \quad (2.4)$$

Given  $\theta_1$ ,  $n_1$  and  $n_2$ , the value of the reflectance and transmittance coefficients can be found by rewriting  $\cos \theta_2$  in terms of  $\sin \theta_2$ ,

$$\cos \theta_2 = \sqrt{1 - \sin^2(\theta_2)} = \sqrt{1 - \left(\frac{n_1}{n_2}\right)^2 \sin^2(\theta_1)}, \quad (2.5)$$

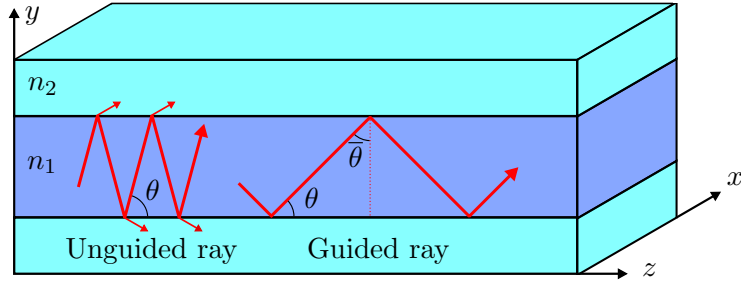
where (2.1) was used in the last step.

The interesting thing to note here is that the expression inside the square root can become negative, resulting in a purely imaginary value for  $\cos \theta_2$ . This happens when  $n_1 > n_2$  and the incident angle  $\theta_1$  is bigger than some critical angle  $\theta_c = \arcsin(n_2/n_1)$ . Calculating  $\mathcal{R}$  for  $\theta_1 \geq \theta_c$ , we find that the power reflectance is unity – that is, we have total reflection at the interface [7, 9]. It is this phenomenon that has allowed us to develop guided-wave optics, where light can be confined and transmitted along dielectric conduits, such as waveguides and optical fibers.

Another important thing to note is that a phase shift is imparted on the light ray as it undergoes reflection. The phase shift is different for TE and TM polarization, and it is calculated from the Fresnel reflection coefficients as  $\phi_r = \arg(r)$  [7], resulting in

$$\tan \frac{\phi_r}{2} = \begin{cases} \sqrt{\frac{\cos^2(\theta_c)}{\cos^2(\theta_1)} - 1} & \text{(TE)} \end{cases} \quad (2.6a)$$

$$\begin{cases} -\frac{1}{\sin^2(\theta_c)} \sqrt{\frac{\cos^2(\theta_c)}{\cos^2(\theta_1)} - 1} & \text{(TM)} \end{cases} \quad (2.6b)$$



**Figure 2.1:** Light rays propagating at different angles in a planar dielectric waveguide. The core is colored dark blue and the cladding light blue, and their refractive indices are  $n_1$  and  $n_2$ , respectively. For the ray on the left, the conditions for total reflection is not met at the interfaces, causing light to leak into the cladding. For the ray on the right the total reflection condition is met, and the ray is therefore guided within the waveguide. The angle  $\theta$  has different values for the two rays, but the same symbol has been used to be consistent with the theoretical treatment in this chapter. The figure is adapted from [7].

### 2.1.2 Planar dielectric waveguide

Let us now consider a thin layer of dielectric material sandwiched between a material of lower refractive index, as depicted in Figure 2.1. We will refer to these layers as the *core* and *cladding*, respectively. We examine a ray of light that is propagating within the core at an angle  $\theta$  relative to the interface normal. When the criterion for total reflection is met at both interfaces, the ray will bounce back and forth without any power loss to the cladding. Such a construction is called an optical waveguide, and this specific design is referred to as a planar dielectric waveguide.

Light entering this structure must do so at an angle that results in total internal reflection, accounting for the refraction that occurs at the interface between air and the core material. The sine of the maximum acceptance angle  $\theta_a$  is often referred to as the numerical aperture (NA) and can be found directly from (2.1). The light incident on the waveguide is assumed to travel in air with  $n_{\text{air}} = 1$ . We then find

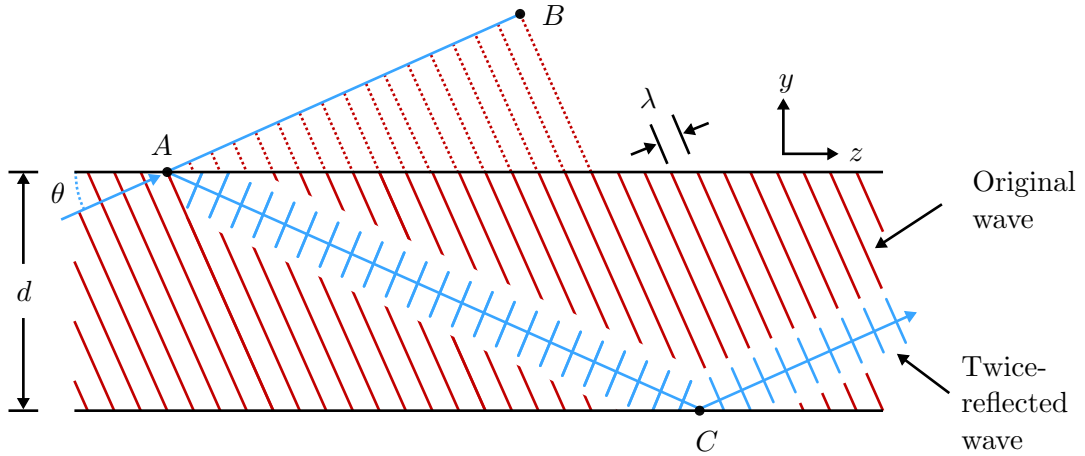
$$\text{NA} = \sin \theta_a = n_1 \sin \theta. \quad (2.7)$$

The numerical aperture can also be expressed purely in terms of the refractive indices [7, 9]. It is then given by:

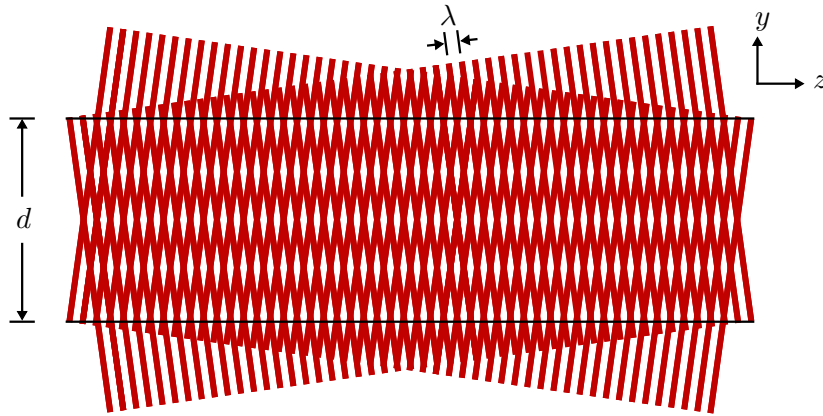
$$\text{NA} = \sqrt{n_1^2 - n_2^2}. \quad (2.8)$$

### 2.1.3 Modes

Ray optics cannot explain all observed effects in waveguides [7]. In the following discussion, we will therefore depart from this description of light and analyze our model from the viewpoint of electromagnetic optics. Instead of optical rays, we will consider a set of monochromatic transverse-electromagnetic (TEM) plane waves of wavelength  $\lambda = \lambda_0/n_1$ , whose sum constitutes the total electromagnetic field in the waveguide.  $\lambda_0$  is here the wavelength of the waves in vacuum.



**Figure 2.2:** Illustration of the self-consistency condition for modes in a planar dielectric waveguide. To increase clarity, only the local maxima of the plane waves propagating within it are shown. The plot shows the case where the self-consistency condition is fulfilled. The figure is adapted from [7].



**Figure 2.3:** Illustration of the field distribution for a mode in a planar dielectric waveguide. To increase clarity, only the local maxima of the plane waves propagating within it are shown. The figure is adapted from [7].

Each reflection of a plane wave is accompanied by a phase shift given by (2.6), resulting in a lot of destructive interference in the waveguide. To ensure successful propagation, we must therefore impose a self-consistency condition, requiring that each plane wave must reproduce itself upon being reflected twice – see Figure 2.2. This will result in only two distinct plane waves, and an electromagnetic field that maintains the same transverse distribution and polarization at all locations along the waveguide axis. Fields that satisfy this condition are called *modes* [7]. The field distribution for such a mode is illustrated in Figure 2.3.

Consider now the geometry in Figure 2.2. After two successive reflections, the path difference between the original and the twice-reflected wave  $\overline{AC} - \overline{AB}$  must be equal to  $2\pi$  to meet the requirement for constructive interference. Using the trigonometric identity  $\cos(2\theta) = 1 - 2\sin^2(\theta)$ , it can be shown that

$\overline{AC} - \overline{AB} = 2d \sin \theta$ , where  $d$  is the thickness of the core. When also accounting for the phase shift  $\phi_r$  due to total reflection at the interfaces we find that

$$\frac{2\pi}{\lambda} 2d \sin(\theta) - 2\phi_r = 2\pi m, \quad m = 0, 1, 2, \dots \quad (2.9)$$

Our discussion thus far has been valid for both TE and TM modes. We will now limit our focus to the TE case, which is the configuration that will be utilized throughout this thesis. Substituting  $\theta_1 = \pi/2 - \theta$  and  $\theta_c = \pi/2 - \bar{\theta}_c$  in (2.6a), we find

$$\tan\left(\frac{\phi_r}{2}\right) = \sqrt{\frac{\sin^2 \bar{\theta}_c}{\sin^2 \theta} - 1}. \quad (2.10)$$

Inserting this result into (2.9), we get the self-consistency condition expressed as a function of  $\sin \theta$  [7],

$$\tan\left(\pi \frac{d}{\lambda} \sin \theta - m \frac{\pi}{2}\right) = \sqrt{\frac{\sin^2 \bar{\theta}_c}{\sin^2 \theta} - 1}. \quad (2.11)$$

The solutions to this equation yield the bounce angles  $\theta_m$  of the supported modes. Also, given the wavelength and the core thickness  $d$ , one can find the number of supported TE modes in a dielectric planar waveguide by calculating the number of solutions to this equation. However, because this is a transcendental equation, we will rather study a plot of the left- and right-hand sides as a function of  $\sin \theta$ . This can be seen in [Figure 2.4](#) on page 11. From this figure, we can deduce that the number of modes  $M$  must be equal to the smallest integer greater than  $2d \sin \bar{\theta}_c / \lambda$ . That is,

$$M = \left\lceil \frac{2d \sin \bar{\theta}_c}{\lambda} \right\rceil, \quad (2.12)$$

where  $\lceil \dots \rceil$  denotes rounding up to the nearest integer ( $1.2 \rightarrow 2$ ,  $0.8 \rightarrow 1$ ,  $1 \rightarrow 2$ , etc.). Since  $\cos \bar{\theta}_c = n_2/n_1$ , we can use (2.8) to rewrite this in terms of the numerical aperture as

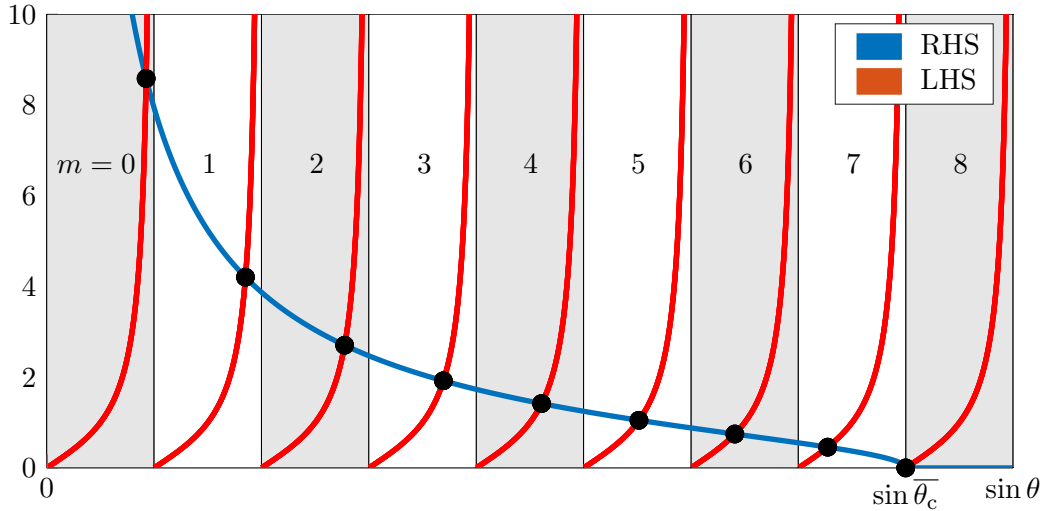
$$M = \left\lceil \frac{2d}{\lambda_0} \text{NA} \right\rceil. \quad (2.13)$$

## 2.2 Waveguides

The case we have been studying thus far is the planar dielectric waveguide, but there are also many other configurations in which light can be confined and transmitted along dielectric conduits. In this section we will discuss some other waveguide designs, and also extend our theory to two-dimensional waveguides.

### 2.2.1 Square waveguides

The planar dielectric waveguide has a finite core thickness in the  $\mathbf{y}$ -direction, but its extents are infinite in the two other dimensions. This allows for a



**Figure 2.4:** Plot of the left- and right-hand sides (LHS and RHS) of (2.11) for a waveguide supporting 9 modes. The solutions to the equation are given by the intersections marked with black circles. The colored areas all have a width  $\lambda/2d$ , and each of them contains exactly one black circle. The mode number  $m$  corresponding to each of these solutions are indicated in the figure as well. The figure is adapted from [7].

simpler theoretical treatment, but it is not a very practical design in real-life applications.

We will continue to model the core as infinitely long in the propagation direction ( $\mathbf{z}$ ), but will now consider both of the transverse directions to be of finite width. The principles of operation are essentially the same as for the planar dielectric waveguide, but the mathematical description is significantly longer and more complex to account for the additional phase matching restrictions in the x-direction. Our treatment will be simplified to the case of a square waveguide, where the width of the core is  $d$  in both of the transverse directions. The cladding is still assumed to be of infinite extent.

Consider a plane wave propagating within this square structure. Our self-consistency condition must now be applied to both transverse directions simultaneously. This can be written as a generalization of (2.9),

$$2k_x d - 2\phi_r = 2\pi m_x, \quad m_x = 1, 2, \dots \quad (2.14a)$$

$$2k_y d - 2\phi_r = 2\pi m_y, \quad m_y = 1, 2, \dots \quad (2.14b)$$

where  $k_x$  and  $k_y$  denote the wavevectors along the x-direction and y-direction, respectively. The propagation constant  $\beta = k_z$  can be found from the relation

$$k_x^2 + k_y^2 + \beta^2 = n^2 k_0^2, \quad (2.15)$$

where  $k_z$  is the wavevector along the  $\mathbf{z}$ -direction [7]. From this we see that the propagation constant assumes discrete values for a given wavelength  $\lambda_0 = 2\pi/k_0$ . The supported modes are then also discrete, and each mode is described by the two index parameters  $m_x$  and  $m_y$ . Due to symmetry, modes can have propagation in both the forward and backward directions. To find the number of

supported modes, we therefore only count the modes with positive values for  $\beta$ . The propagation constant must also be larger than zero, to ensure that the wave is actually propagating in the z-direction. This gives rise to the requirement

$$k_x^2 + k_y^2 \leq n^2 k_0^2. \quad (2.16)$$

However, a stricter requirement must also be imposed, as we must require that the propagation angle inside the waveguide results in total internal reflection. We can extend the above requirement in terms of the critical angle  $\bar{\theta}_c$  as

$$k_x^2 + k_y^2 \leq n_1^2 k_0^2 \sin^2 \bar{\theta}_c. \quad (2.17)$$

The number of supported modes is then given by the number of solutions to this inequality. The complexity of this equation, however, makes it difficult to find an analytical expression for the number of modes in the general case. We will instead derive an approximate expression.

A visualization of the  $k_x$  and  $k_y$  values for the supported modes can be seen in [Figure 2.5](#) on page 13. The modes are not spaced uniformly, but their average horizontal and vertical separations are approximately  $\pi/d$  [7]. We can therefore approximate the number of modes as the area of the quarter circle divided by the average area occupied by each mode,

$$M \approx \frac{(\pi/4)(n_1 k_0 \sin \bar{\theta}_c)^2}{(\pi/d^2)} \approx \frac{\pi}{4} \left( \frac{2d}{\lambda_0} \right)^2 \text{NA}^2, \quad (2.18)$$

where NA is the numerical aperture. The approximation is good for large values of  $M$ , and we see that the number of modes is roughly the square of the expression we found for the planar dielectric waveguide in [\(2.13\)](#).

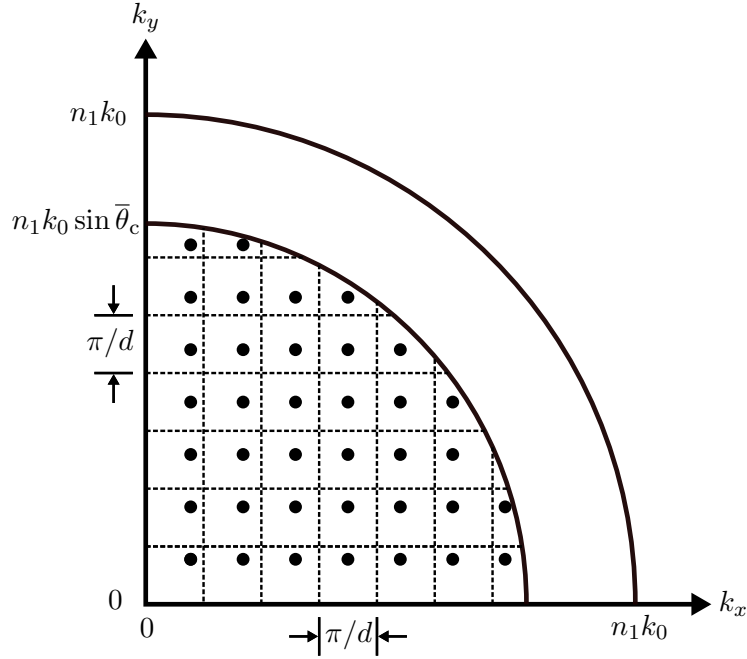
If the waveguide instead was rectangular, the corresponding illustration would be very similar to [Figure 2.5](#), but with a cylindrical boundary for the propagation constant requirement and more rectangular areas enclosed by the dotted lines [7]. An estimation of the number of modes in a rectangular waveguide can be found in [10].

### 2.2.2 Channel waveguides

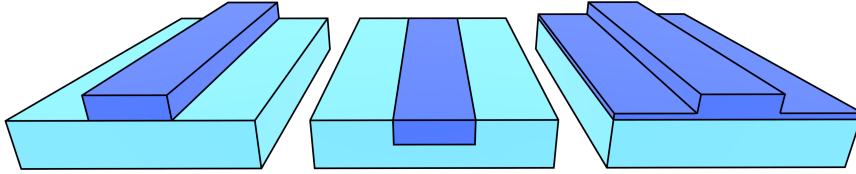
The waveguides we have been considering until now have all been surrounded by a cladding of infinite extent. We have mostly assumed this second material to be air with refractive index  $n_{\text{air}} \approx 1$  to simplify our calculations. In real designs, however, the waveguide is usually enclosed fully or partially in a second material with refractive index  $n_2$ .

A common choice of materials is silicon for the waveguide, placed on a silica ( $\text{SiO}_2$ ) cladding that has been grown on a silicon wafer substrate. This is often referred to as a silicon-on-insulator (SOI) design, and has the advantage that it is very compatible with existing semiconductor manufacturing technology. The refractive indices are  $n_{\text{Si}} \approx 3.48$  and  $n_{\text{SiO}_2} \approx 1.45$ , resulting in a quite high numerical aperture. We will cover the SOI platform in more detail in section [3.3.1](#).





**Figure 2.5:** The supported values of  $k_x$  and  $k_y$  for a square waveguide. Supported modes are marked with black circles, and the dotted grid indicates the average area occupied by each mode. Both of the requirements in (2.16) and (2.17) are indicated as quarter-circles. The latter provides a cut-off where supported values of  $k_x$  and  $k_y$  outside of the quarter-circle does not result in supported modes. The figure is adapted from [7].

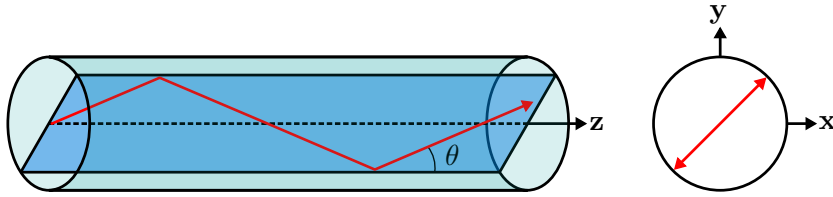


**Figure 2.6:** Different geometrical designs of waveguides with planar boundaries. Silicon core structures are colored dark blue, and the silica claddings are colored light blue. From left to right, the three designs are called strip, embedded strip and rib waveguides, respectively.

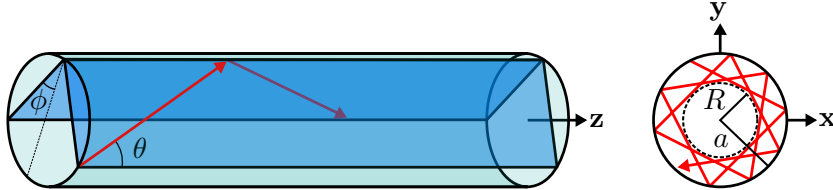
There are various geometrical configurations for waveguides that are partially covered with solid cladding materials and partially covered with air, some of which are illustrated in Figure 2.6. The analytical treatment of these designs become challenging, as one has to account for different phase shifts and critical angles at the different boundaries. This is especially true for the rightmost rib structure where the width of the waveguide is not constant. Total internal reflection is also accompanied by evanescent waves propagating in the cladding, causing additional deviations from ideal theory. The strip waveguide is the configuration that will be used throughout this thesis.

### 2.2.3 Optical fiber waveguides

Optical fibers are subject to the same fundamental physical principles as the planar and rectangular waveguides we have covered previously. The main dif-



**Figure 2.7:** Meridional propagation in an optical fiber where the light is confined to a single plane. Both a side view and a cross-sectional view is included. The figure is adapted from [7].



**Figure 2.8:** Skewed propagation where the azimuthal component of the light varies along the propagation direction. The angle  $\phi$  of the propagation planes relative to the radial direction is here a constant  $\neq 0$ . A cross-sectional view of the resulting helical trajectory is shown on the right. The inner and outer radii of the cylindrical shell in which the light is propagating are denoted  $R$  and  $a$ , respectively. The figure is adapted from [7].

ference is that optical fibers have cylindrical geometries, with a core that is fully enclosed in a concentric cladding. As before, we denote the refractive indices of the core and cladding  $n_1$  and  $n_2$ , respectively.

In the simplest case, the light propagating along the waveguide has transverse wavevector components that are purely radial. That is, the light waves are confined to a meridional plane and pass through the center of the cylinder between each reflection, as illustrated in [Figure 2.7](#). This configuration is essentially equivalent to that of the planar dielectric waveguide, which we have already covered. Equations derived for the planar design remain valid.

A more complex case arises when the transverse wavevectors also have azimuthal components. A propagating ray will then be subject to repeated reflections at constant incident angles  $\phi$ , as illustrated in [Figure 2.8](#). The resulting light then follows a helical trajectory and propagates within a cylindrical shell of inner and outer radii  $R$  and  $a$ , respectively, where  $a$  is the radius of the core. The simple case of meridional rays explained above is found when  $\phi = 0$ . When  $\phi \neq 0$ , we call it *skewed rays*. [7, 11]

Optical fibers are usually constructed with very small differences between the refractive indices of the core and cladding [7]. This is often achieved by very light doping of one of the materials, and allows us to approximate the fractional refractive index change as

$$\Delta \equiv \frac{n_1^2 - n_2^2}{2n_1^2} \approx \frac{n_1 - n_2}{n_1} \ll 1. \quad (2.19)$$

Denoting the acceptance angle of the fiber  $\theta_a$ , we can derive an expression for

the numerical aperture as before, using  $\cos \bar{\theta}_c = n_2/n_1$ ,

$$\text{NA} = \sin(\theta_a) = n_1 \sin(\bar{\theta}_c) = n_1 \sqrt{1 - \cos^2(\bar{\theta}_c)} \quad (2.20)$$

$$= \sqrt{n_1^2 - n_2^2} \approx n_1 \sqrt{2\Delta}. \quad (2.21)$$

### 2.2.3.1 Field distribution in an optical fiber

Let us now examine the field distribution inside an optical fiber in a bit more detail. All components of the electric and magnetic fields are governed by the Helmholtz equation,

$$\nabla^2 U(x, y, z) + n^2(r)k_0^2 U(x, y, z) = 0, \quad (2.22)$$

with  $k_0 = 2\pi/\lambda_0$  as before and  $U(x, y, z)$  being a field-describing function [7]. The refractive index is different in the core and cladding, and is therefore given by

$$n(r) = \begin{cases} n_1, & r < a \\ n_2, & r > a, \end{cases} \quad (2.23)$$

where  $a$  is the radius of the core. Transforming the Helmholtz equation to a cylindrical coordinate system, we find

$$\frac{\partial^2 U}{\partial r^2} + \frac{1}{r} \frac{\partial U}{\partial r} + \frac{1}{r^2} \frac{\partial^2 U}{\partial \phi^2} + \frac{\partial^2 U}{\partial z^2} + n^2 k_0^2 U = 0, \quad (2.24)$$

where  $U = U(r, \phi, z)$ . The propagation constant of the waves traveling in the  $\mathbf{z}$ -direction is  $\beta_m$ , and the  $z$ -dependence of  $U$  can therefore be found to be proportional to  $e^{-j\beta z}$ . The waves also have a  $\phi$ -dependent periodicity  $2\pi$ , and we can therefore write

$$U(r, \phi, z) = u(r) e^{-jl\phi} e^{-j\beta z}, \quad (2.25)$$

where  $l$  is an integer [7] and  $u(r)$  is the radial distribution of the fields in the optical fiber. Substitution into (2.24) then yields

$$\frac{d^2 u}{dr^2} + \frac{1}{r} \frac{du}{dr} + \left( n^2(r)k_0^2 - \beta^2 - \frac{l^2}{r^2} \right) u = 0. \quad (2.26)$$

The modal angles  $\theta_m$  must lie between 0 and  $\bar{\theta}_c$  for rays to be guided. The corresponding propagation constants  $\beta_m = n_1 k_0 \cos \theta_m$  must then lie between  $n_2 k_0$  and  $n_1 k_0$ . To simplify the following calculations, we therefore define two parameters  $\gamma$  and  $k_T$ , which will have real values and therefore positive squares when the mode is guided,

$$k_T^2 = n_1^2 k_0^2 - \beta^2 \quad (2.27)$$

$$\gamma^2 = \beta^2 - n_2^2 k_0^2. \quad (2.28)$$

Now, (2.26) must be fulfilled for the core and cladding separately. The two resulting differential equations both take the form of Bessel's differential equations, which are well-studied and are applicable to many different situations [7, 8]. Their solutions are known as Bessel functions. We find

$$u(r) \propto \begin{cases} J_l(k_T r), & r < a \\ K_l(\gamma r), & r > a. \end{cases} \quad (2.29)$$

$J_l(x)$  and  $K_l(x)$  are here the normal and modified Bessel functions of first and second kind, respectively.  $J_l(x)$  is an oscillating function with decreasing amplitude as  $x$  increases.  $K_l(x)$  decreases monotonically as  $x$  increases. We can then conclude that the distribution within and at the output of the optical fiber is given by the Bessel functions [7, 8].

Although electromagnetic diffraction is suppressed inside the fiber due to its guiding properties, it becomes important when examining the beam at the output of the fiber. We can consider the diffraction of the Bessel beam analytically, but a Gaussian distribution can often be employed instead [7, 9],

$$f(x) = \frac{1}{\sqrt{2\pi\sigma^2}} e^{-(x-\mu)^2/2\sigma^2}, \quad (2.30)$$

where  $\sigma$  is the standard deviation and  $\mu$  is the mean. The Gaussian distribution simplifies calculations and has a very close resemblance to the Bessel beam when the initial beam diameter in the Gaussian distribution is set equal to the mode-field diameter of the fiber [12]. The mode-field diameter (MFD) is the diameter of the part of the output distribution where the electromagnetic field strength is above  $1/e$  of its maximum value. The MFD is often slightly wider than the core diameter of an optical fiber and is usually given in fiber datasheets.

As for the planar and rectangular waveguides, we can find a characteristic equation for the supported modes in the fiber. It has a significantly more complex form than the ones we have considered previously and is found from Maxwell's equations and our radial distribution when requiring the continuity of certain electric and magnetic field components across the core-cladding interface. The characteristic equation is given by

$$X \frac{J_{l\pm 1}(X)}{J_l(X)} = \pm Y \frac{K_{l\pm 1}(Y)}{K_l(Y)}, \quad (2.31)$$

where  $X = k_T a$  and  $Y = \gamma a$  [7]. As before,  $a$  denotes the radius of the core. The number of supported modes is given by the number of solutions to this equation, which is difficult to solve analytically. It can be solved graphically by plotting both the right- and left-hand sides, and then counting the number of intersections. An approximate expression can be found for the number of modes,

$$M \approx \frac{4V^2}{\pi^2}, \quad (2.32)$$

provided that  $V$  is large. The  $V$ -parameter is often referred to as the *normalized frequency* and is given by  $V = \sqrt{X^2 + Y^2}$  [7]. It can also be expressed in terms

of the numerical aperture as

$$V = \frac{2\pi r_{\text{core}}}{\lambda_0} \text{NA}, \quad (2.33)$$

where  $r_{\text{core}}$  is the radius of the core. The numerical aperture is usually provided in the datasheets for optical fibers. It can be shown that when we have  $V < 2.405$ , the fiber supports only a single mode [9].

Our theoretical treatment of optical fibers has focused on step-index fibers only, where the refractive indices of the core and cladding are constant. There are also other designs, e.g. with a gradient refractive index in the core. These more complex designs aim to reduce dispersion by compensating for the different group velocities of different modes. Since step-index fibers will be used in this thesis, the analysis of such designs is omitted here, and the reader is instead referred to [7, 9] for a more in-depth description of waveguides and optical fibers.

## 2.3 Coupling

We have covered the basic principles of guided-wave optics and waveguides, and will now shift our focus to the main problem of this thesis: how can we transfer light from a relatively big optical fiber to a waveguide of much smaller dimensions as efficiently as possible? The interchange of optical power between two guided-wave structures is called *coupling*, and fraction of light that is successfully coupled into the second structure is called the *coupling efficiency*  $\mu_c$ .

To convey the coupling principle as simple as possible, we will discuss the case for a planar dielectric waveguide similar to that in [Figure 2.1](#) on page 8. As we have seen, light in waveguides propagates in specific modes. The superposition of these modes constitutes the total electric field within the waveguide, which is given by

$$E(y, z) = \sum_m a_m u_m(y) e^{-j\beta_m z}, \quad (2.34)$$

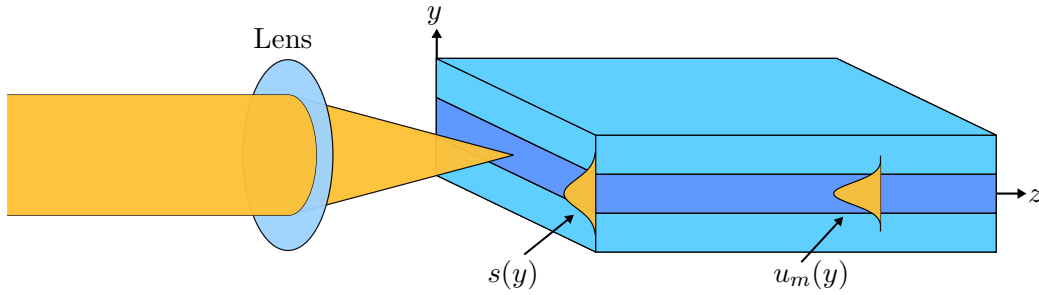
where  $\beta_m$  is the propagation constant of mode  $m$  as before,  $a_m$  is the amplitude and  $u_m(y)$  is the transverse modal distribution [7]. We now direct a source of some arbitrary distribution  $s(y)$  into the waveguide. Since propagation is only supported in specific modes, the fraction of power transferred from the source to the waveguide is dependent on the similarity between  $s(y)$  and  $u_m(y)$  [7]. Expanding  $s(y)$  in terms of the transverse modal distributions, we find

$$s(y) = \sum_m a_l u_m(y), \quad (2.35)$$

where the expansion coefficients  $a_l$  can be found by multiplying the above equation with  $u_l(y)$ , integrating with respect to  $y$ , and using the orthogonality of the modal distributions  $\int_{-\infty}^{\infty} u_l(y) u_m(y) dy = 0$ . After normalizing, the coefficients are then found to be

$$a_l = \int_{-\infty}^{\infty} s(y) u_l(y) dy, \quad (2.36)$$

and express the correlation between the source distribution and the modal distributions.



**Figure 2.9:** Butt coupling where a lens is used to focus the laser beam. The transverse distributions of the incident beam and the waveguide modes are marked  $s(y)$  and  $u_m(y)$ , respectively. The refractive index of the core is  $n_1$  and the refractive index of the cladding is  $n_2$ . The figure is adapted from [7].

### 2.3.1 Butt coupling

The most straight-forward coupling method is called butt coupling. It involves directing a laser beam directly at one of the ends of the waveguide, often focusing the laser beam using lenses. The method is shown in Figure 2.9. For a waveguide mode to be excited, the transverse distributions of that mode and the incident light should match, and the polarization must also be the same as that of the supported mode.

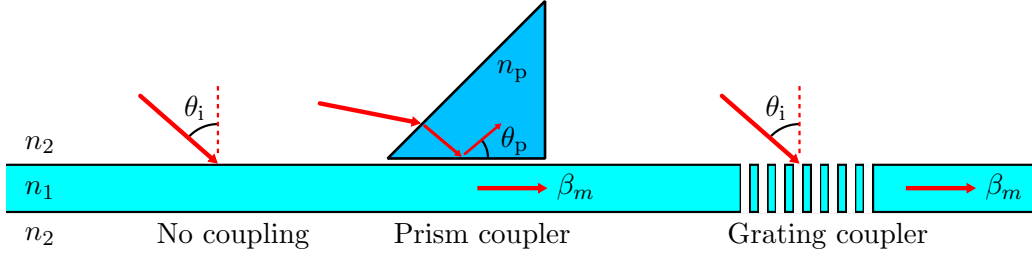
The coupling efficiency using butt coupling is not particularly good. According to [13], the typical theoretical coupling efficiencies for a Corning SMF-28 step-index fiber [14] will be less than 29%. In real-life applications, the efficiencies would likely be significantly lower.

Improvements can be made to increase the coupling efficiency. Losses from Fresnel reflection at the air-waveguide interface could be reduced by using an anti-reflective coating. Precise alignment systems would help ensure that the center of the source coincides with the center of the core, minimizing misalignment losses. Also, as we have seen previously, there is a maximum supported acceptance angle into the modes of the waveguide, given by the numerical aperture in (2.7). If we focus the source beam using a lens system, coupling efficiencies can be improved significantly. Using complex end-face geometries, efficiencies close to 65% have been achieved [15].

Unfortunately, the complexity and cost of these improvements can be high. Butt coupling techniques also require input ports to be located on sample sidewalls, which makes them vulnerable to contamination and damage. For integrated photonics applications, it is therefore often preferable to have input and output ports closer to the center of the samples, where the photonic structures are located. Since the goal of this thesis is to design a coupling structure for a SOI lab-on-a-chip biosensor, a design that allows coupling of light into the waveguide from above will rather be used.

### 2.3.2 Top coupling

Let us consider a ray of light that propagates in the cladding material with refractive index  $n_2$  and that is incident on the core from above at some incidence



**Figure 2.10:** Illustration of the prism and grating coupling techniques. The case where light is incident on the unmodified waveguide from above is also shown in the left side of the figure. The refractive indices of the core, cladding and prism are denoted  $n_1$ ,  $n_2$  and  $n_p$ , respectively. We have  $n_p > n_2$ , and also  $n_1 > n_2$  as before. Light being successfully coupled into the waveguide is indicated by red arrows inside the core. The figure is adapted from [7].

angle  $\theta_1 = \theta_i$ , as depicted on the left side of Figure 2.10. If the incident angle is larger than the critical angle for total reflection, no light will be transmitted into the waveguide. If the angle is less than the critical angle, the ray of light would be partially transmitted and partially reflected, resulting in some fraction of the ray entering the waveguide. Is it then possible to couple light into the waveguide from above? As it turns out it is not that simple.

The angle of refraction  $\theta_2$  is given by Snell's Law (2.1). We have previously discussed the requirement for modes and phase matching, but let us retrace and take a look at the most basic requirement for the ray to be guided: we must require that it propagates within the waveguide at an angle that results in total internal reflection. It is therefore vital that the transmitted ray is fully reflected upon reaching the bottom core-cladding interface.

If we interchange  $n_1$  and  $n_2$ , and  $\theta_1$  and  $\theta_2$  in (2.2a) on page 7, we find the corresponding reflection coefficient,

$$r_{\text{TE}} = \frac{2n_2 \cos \theta_2}{n_2 \cos n_2 + n_1 \cos \theta_1}. \quad (2.37)$$

Now, if we replace  $n_2 \cos \theta_2$  in the nominator using Snell's law (2.1), we find that the reflection coefficient is exactly the same as that of the first interaction, where the ray of light was incident on the core from above. And since we required that the light was at least partially reflected then, it must also be partially reflected now, and we do not have total internal reflection. The light entering the waveguide will therefore gradually leak out again, and there will be no coupling.

This can also be shown in terms of the propagation constant. We can express the phase matching condition for modal coupling as

$$n_2 k_0 \cos \theta_i = \beta_m. \quad (2.38)$$

As mentioned in section 2.2.3.1, the propagation constant must lie between  $n_2 k_0$  and  $n_1 k_0$  to be guided. Focusing on the lower limit, we must have  $\beta = \beta_m > n_2 k_0$ . We then see that it is not possible to fulfill the above equation, and coupling can therefore not occur [7].

There are, however, some techniques we can use to circumvent this problem, two of which are shown in [Figure 2.10](#). We will discuss these in the next two subsections.

### 2.3.3 Prism coupling

As can be seen in [Figure 2.10](#), placing a triangular prism in close proximity to the core and directing the incident light towards the inclined plane could allow coupling into the waveguide at certain angles [7, 8, 16]. However, this can only work if the refractive index of the prism  $n_p$  is higher than that of the cladding.

With the correct configuration, light entering the prism will be subject to total internal reflection at the bottom prism plane. The incident and reflected waves will then form a wave traveling towards the right, parallel to the interfaces. This wave will penetrate partially into the waveguide as an evanescent field that decreases exponentially with the vertical distance from the prism. If the propagation constant of the traveling wave is equal to one of the propagation constants of the waveguide modes, light can couple into the waveguide [7, 16].

The theoretical treatment of this effect is quite complicated and is based on solving Maxwell's equations for the different regions and using the boundary conditions to determine the modes of the system. Approximations based on perturbation theory can provide a simpler theoretical approaches, but is beyond the scope of this thesis. The interested reader is referred to [16] for a more extensive treatment of prism coupling techniques.

Prism couplers have been in use for several decades, and a theoretical efficiency of 80% was demonstrated already in 1970 [17]. They have high efficiencies in general and also give good control over which modes light is coupled into. However, they are quite complex to design using traditional complementary metal-oxide-semiconductor (CMOS) techniques. The need for a different refractive index than the cladding calls for additional manufacturing steps, and the inclined plane requires good control over processing techniques to get a sufficiently smooth surface. Alignment of the prism relative to the waveguide is also a significant issue. [8]

### 2.3.4 Grating coupling

An alternative way to enable coupling into a waveguide from above is based on the introduction of periodic defects. If a set of holes of sub-wavelength width are etched with sub-wavelength separation between them, we have essentially constructed a *diffraction grating* [18]. A simplified schematic of such a structure is included on the right-hand side of [Figure 2.10](#).

Diffraction gratings are optical components that modulate the phase and amplitude of the incident plane waves. The modulation causes output beams to propagate at different angles than the input, and these angles of diffraction are wavelength-dependent [16]. By tuning the geometry of the diffraction grating, one can therefore construct a component that changes the propagation constant to coincide with some modal propagation constant  $\beta_m$  [7, 16].



As the incident wave interacts with the grating, the phase of the incident light is modulated by phase factors  $2\pi q/\Lambda z$ , where  $q = \pm 1, \pm 2, \dots$  and  $\Lambda$  is the period of the grating structure [7, 8]. This corresponds to a change in the axial wavevector component of  $2\pi q/\Lambda$ . The phase matching condition for coupling into a mode can now be expressed as

$$n_2 k_0 \cos \theta_i + \frac{2\pi q}{\Lambda} = \beta_m. \quad (2.39)$$

This expression is very similar to that in (2.38), but the extra term now allows the requirement  $\beta_m > n_2 k_0$  to be fulfilled for certain periods. By proper tuning of the grating geometry, it is even possible to enhance the  $q = 1$  component, which tends to be of quite high intensity [7].

Simple grating couplers tend to have lower maximum efficiencies than prism couplers, but they are significantly easier to manufacture and align [8]. There are no additional manufacturing steps required, as the grating structure can be incorporated into the mask used to produce the waveguide. Certain complex grating designs show significantly higher coupling efficiencies, but are often more difficult to manufacture. Examples include apodized gratings with non-uniform widths and separations [19–21], reflective bottom metal layers [22, 23] and even stacked grating layers with relative horizontal offsets [24].

The two latter examples are interesting but complicate the manufacturing process. The apodized structure will not complicate the manufacturing significantly, but the design optimization process is still quite complex. When developing an apodized structure, it could therefore be beneficial to start out with an optimized uniform grating structure and then improve the design iteratively to arrive at the apodized solution.

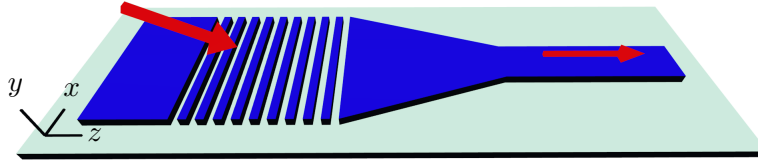
A principle that is important for the performance of coupling structures is the reciprocity theorem. It states that light traveling through a linear optical medium will travel along the exact same path if we reverse its direction and let it travel the opposite way through the structure [7, 18]. This has the consequence that any structure that couples light into the waveguide would also couple light out of the waveguide. It is therefore important that the grating coupler is not too long, as the light that is coupled in at one end would then be coupled out again before it has made it past the grating structure and into the normal waveguide [8].

### 2.3.5 Taper coupling

The beam diameter of an external laser source is usually significantly larger than the width of integrated waveguide structures. Using a grating coupler of the same width as the waveguide therefore results in significant losses, since much of the incident power will impact the areas to the side of the waveguide.

This can be solved by making the grating coupler significantly wider than the integrated waveguide, while using an additional construction to couple light from the gratings to the waveguide. A common technique is to construct a taper coupler [25–27], as illustrated in Figure 2.11 on page 22. A taper coupler is a gradual narrowing of the waveguide, forcing light to either be reflected or

coupled into the narrower waveguide. With a sufficiently slow and gradual narrowing, the coupling efficiency of a taper coupler can be made quite high [8, 25]. Its losses can be significantly smaller than the loss due to the source/waveguide dimension mismatch mentioned previously.



**Figure 2.11:** Conceptual schematic showing a taper coupler connecting a grating coupler and a waveguide. Dark blue areas represent the waveguide material, while the bright green areas represent the bottom cladding. Red arrows indicate the flow of light. Note that the arrow at the output is smaller than the arrow at the input due to coupling losses in the grating and taper couplers.

## 2.4 Simulation techniques

Due to the complexity of the grating structure, it is difficult to find optimized designs using a purely mathematical approach. It is then useful to turn to numerical methods and computational electromechanics. This allows us to run computer simulations on the behavior of electric and magnetic fields in structures and optical devices [28]. There are a vast range of such computational methods that all have their advantages and disadvantages. Many are specialized to handle specific types of geometries or materials, while others are more flexible.

One family of methods is called finite methods, which are based on discretization of differential equations at grid points or finite areas/volumes. They are classified into roughly three categories – finite-difference methods (FDM), finite-volume methods (FVM) and finite-element methods (FEM) [29, 30]. These methods are all fairly universal and can be applied to almost any kind of problem, provided that geometries and boundary conditions are configured properly [28]. The finite element method has been the method of choice in this thesis, and will therefore be the focus in following discussions.

### 2.4.1 Finite element method

A wide variety of physics problems can be described by partial differential equations (PDEs), in addition to initial and boundary conditions. The finite element method divides the geometry of the problem into small, finite elements (areas in 2D or volumes in 3D) [28]. These elements constitute a *mesh*, in which all elements have at least one boundary in common with another mesh element.

Through simplification of the PDEs, the geometry and physics of the simulation domain can then be expressed in terms of a high number of coupled equations. These equations then constitute matrix elements in a matrix equation that can be solved using efficient computational factorization methods.

Physical results can then be derived from the solved matrix equation during post-processing steps. [31, 32]

As with all numerical approximations, the final solutions are prone to error. For the finite element method, the error is highly dependent on the typical size of the mesh elements. Smaller mesh elements result in smaller errors, and therefore a more accurate solution [28, 31]. Unfortunately, smaller mesh element sizes also result in more mesh elements and therefore a larger matrix that must be solved to arrive at a solution. This requires more memory, processing power and simulation time.

### 2.4.2 Simplification to two dimensions

When simulating three-dimensional (3D) structures, the most accurate results are found by using 3D models and simulation domains as well. However, in order to reduce memory and processing power requirements, problems are often simplified to two-dimensional (2D) models instead. When the geometry in question has a dimension that can be considered to have infinite extent, it is often possible to collapse this dimension into a plane spanned by the two other dimensions.

This simplification drastically reduces the complexity of the simulation but will also introduce errors. The relative size of these errors is highly dependent on the geometry in question, and on how much the real situation differs from the infinite-extent model.

#### 2.4.2.1 Effective index method

A common problem when working with sub-wavelength structures is that the electromagnetic waves cannot be completely confined within the waveguides. This is due to the wave nature of light, where the electromagnetic fields extend into the adjacent cladding and air. The modes in the waveguide will then propagate as if the effective refractive index  $n_{\text{eff}}$  of the core is a weighted average of the refractive indices of the core *and* the surrounding materials. This is especially important to take into account when a simplification is made from 3D to 2D. For a more detailed description of the effective refractive index method, see [33].

## 2.5 Electrical wave equation

When considering the case of light interacting with an optical gratings structure, the relevant physics are the Maxwell equations, which take the following form

in a charge-free medium [33, 34]:

$$\nabla \times \mathbf{H} = \sigma \mathbf{E} + \frac{\partial \epsilon \mathbf{E}}{\partial t} \quad (2.40a)$$

$$\nabla \times \mathbf{E} = -\frac{\partial \mu \mathbf{H}}{\partial t} \quad (2.40b)$$

$$\nabla \cdot (\epsilon \mathbf{E}) = 0 \quad (2.40c)$$

$$\nabla \cdot \mu \mathbf{H} = 0 \quad (2.40d)$$

The four equations are coupled, and are known individually as Maxwell-Ampère's law, Faraday's law, Gauss's law and Gauss's magnetic law, respectively [34].  $\epsilon$  is here the electric permittivity,  $\mu$  is the magnetic permeability and  $\sigma$  is the electric conductivity.  $\mathbf{E}$  and  $\mathbf{H}$  denote the electric and magnetic fields, respectively.

Maxwell's equation can be used to derive a wide range of important laws in optics. We have already discussed some of them, such as Snell's law and the principle of reciprocity. The speed of light, a fundamental constant of nature, can also be found from Maxwell's equations [35]. We can also derive a second-order PDE that describes how electromagnetic waves propagate in a medium. The derivation is based on [34] and assumes a time invariant material. This allows us to move  $\mu$  outside of the derivative in (2.40b) and take the curl of both sides. Using (2.40a), we find,

$$\nabla \times (\mu^{-1} \nabla \times \mathbf{E}) = -\frac{\partial \nabla \times \mathbf{H}}{\partial t} = -\frac{\partial}{\partial t} \left( \sigma \mathbf{E} + \frac{\partial \epsilon \mathbf{E}}{\partial t} \right) \quad (2.41)$$

$$= -\sigma \frac{\partial \mathbf{E}}{\partial t} - \epsilon \frac{\partial^2 \mathbf{E}}{\partial t^2}, \quad (2.42)$$

where we have assumed  $\epsilon$  to be time independent. Collecting the terms on one side, we find

$$\nabla \times (\mu^{-1} \nabla \times \mathbf{E}) + \sigma \frac{\partial \mathbf{E}}{\partial t} + \epsilon \frac{\partial^2 \mathbf{E}}{\partial t^2} = 0. \quad (2.43)$$

In free space, we have  $\sigma = 0$ ,  $\mu = \mu_0$  and  $\epsilon = \epsilon_0$ , and we can write

$$\nabla \times (\nabla \times \mathbf{E}) + \epsilon_0 \mu_0 \frac{\partial^2 \mathbf{E}}{\partial t^2} = 0. \quad (2.44)$$

Using Gauss's law in free space and that the speed of light in vacuum is given by  $c_0 = (\epsilon_0 \mu_0)^{-1/2}$ , as well as the vector identity

$$\nabla \times \nabla \times \mathbf{E} = \nabla(\nabla \cdot \mathbf{E}) - \nabla^2 \mathbf{E} = \nabla^2 \mathbf{E}, \quad (2.45)$$

we find a second order electromagnetic differential equation

$$\nabla^2 \mathbf{E} - \frac{1}{c_0^2} \frac{\partial^2 \mathbf{E}}{\partial t^2} = 0. \quad (2.46)$$

This equation is the electrical wave equation, which can be used to describe the behavior of electromagnetic waves. A similar equation can also be derived for the magnetic field. These equations, or their more generalized counterparts, are typical PDEs that can be solved for a geometry using the finite element method.

## Chapter 3

# Tools and procedures

This chapter will begin by describing the physics simulation software that has been used extensively in this thesis: COMSOL Multiphysics. It will describe the construction of our model geometry, meshing and the configuration of the relevant physics interfaces that has been used to simulate our grating structures. This will also include modeling of the laser source and our use of the programming language MATLAB.

Section 3.2 will be dedicated to a discussion of the iterative methods that has been used in the simulation-based optimization process. In section 3.3 the different instruments and techniques that have been utilized throughout the experimental part of this thesis will be described. Detailed descriptions of experimental procedures can be found in section 3.4. Characterization tools and procedures that were used to examine the manufactured grating coupler prototypes are presented in sections 3.5 and 3.6.

The first paragraph of sections 3.1, 3.1.3 and 3.1.3.1 and the two first paragraphs of section 3.1.1 are all taken from the project thesis [1] with only minor changes.

### 3.1 Simulation tools

The design of complex physics simulations can be very time-consuming. Models must be constructed that contain information about the simulation domains, geometries, materials, etc. The finite element method must be implemented, along with all initial and boundary conditions, and the partial differential equations that describe the physics of the problem must be found and applied. Fortunately, since many of these steps are quite similar for a wide variety of problems, software solutions have been developed that aim to provide all of this through simple and intuitive graphical interfaces.

#### 3.1.1 COMSOL Multiphysics

COMSOL Multiphysics has been chosen as the primary simulation tool to perform grating coupler optimizations in this thesis. According to COMSOL themselves, the software is a “general-purpose simulation software for modeling de-

signs, devices and processes in all fields of engineering, manufacturing and scientific research” [36].

COMSOL is primarily FEM-based and contains a full-fledged model builder and many different physics modules that are designed to work with a wide range of physics simulations. Different modules and physics interfaces can also be combined to account for several physical phenomena simultaneously. In addition, COMSOL interfaces with a lot of useful third-party software, such as MATLAB and computer aided design (CAD) programs [36].

The electromagnetic wave optics module is the most relevant for our waveguide and grating coupler simulations. It consists of four separate physics interfaces that are designed to work for different model types and wavelengths. To ensure compatibility between our grating structure and the sensor devices being developed by the photonic research group at NTNU [2], we will be using a laser source of wavelength  $\lambda_0 = 1550$  nm and a waveguide of dimensions  $220$  nm  $\times$   $500$  nm. According to [37], the frequency-domain interface is best suited for such a model and we will therefore use it for all simulations. This interface implements the finite element method using the frequency-domain form of Maxwell’s equations (2.40), and solves the electromagnetic wave equation (2.46) for the electric field [38].

### 3.1.2 MATLAB

Although COMSOL has built-in features that allow iteration over different parameter values, it does not natively support highly dynamic and customizable parameter sweeps. Fortunately, COMSOL does provide interfaces with different third-party solutions – such as MATLAB [39].

MATLAB is a programming language that is specialized for matrix and array mathematics [40]. Throughout this thesis, we have used MATLAB extensively to run dynamic simulations, validate results, make plots and generate design files for prototype manufacturing. We will not discuss every MATLAB script we have used in detail, and will instead focus on explaining the iterative methods and algorithms we have used in our optimizations.

### 3.1.3 Model description

The coupling structure we would like to design closely resembles that of the combined grating and taper coupler in Figure 2.11 on page 22. To simulate this as accurately as possible, we would have to build a 3D model and run COMSOL simulations on those structures. However, due to memory requirements and limited processing power, we will restrict our simulations to two dimensions. That is, we will assume all geometries in Figure 2.11 to be of infinite extents in the x-direction.

When performing such a simplification, it is important to think about the potential consequences this will have for the accuracy of our simulations. In this case, we must be aware that the effective refractive index of our simulated structures could deviate from that of pure silicon due to them being surrounded

by air. Most of the surrounding air will be accounted for by our 2D model, but not along the dimension that we assume to be of infinite extent.

Now, the width of the waveguide is 500 nm, which is significantly less than the wavelength. It would therefore seem like we have to apply the effective index method described in section 2.4.2.1. However, since we plan on using a grating coupler and then guiding the coupled light through a taper structure, this should not be necessary. The grating coupler will be made slightly wider than the mode-field diameter (MFD) of the optical fiber we will be using, which is 10.4  $\mu\text{m}$  [41]. This is significantly more than the wavelength, and our approximation should therefore be good enough even when the effective index method is not applied.

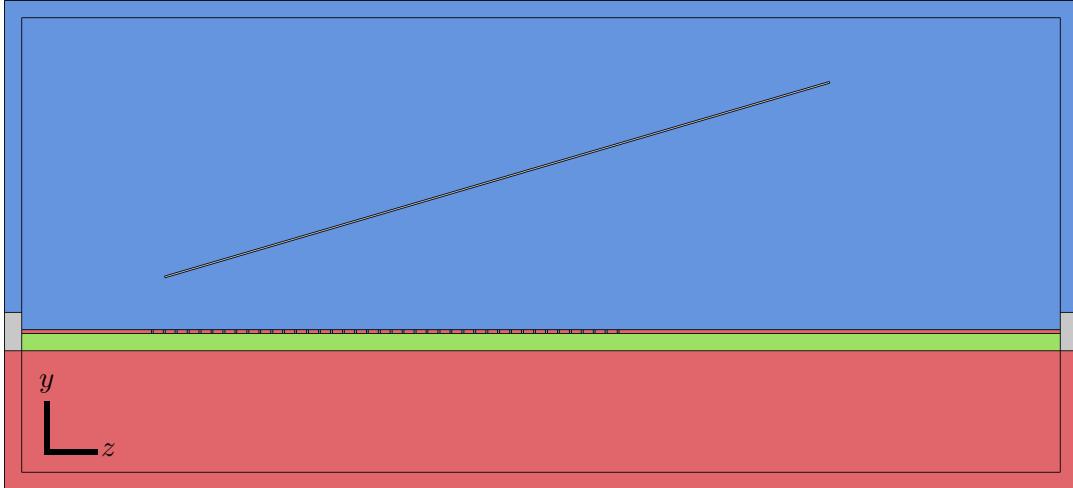
Since the taper coupler narrowing happens in the x-dimension, we cannot include the taper coupler in our 2D model. Losses in the taper structure will therefore not be accounted for in our simulations, and this should be kept in mind when comparing the performance of manufactured devices to the simulation results. According to [25], the losses in our taper should be negligible as long as the narrowing occurs over a sufficiently long distance ( $> 300 \mu\text{m}$ ), but this will of course also be dependent on the manufacturing methods used.

Because the coupling structure should be designed to work with the biosensing devices currently being developed by the photonics research group at NTNU, there are some requirements and limitations that we must keep in mind when designing our model. These requirements ensure compatibility with equipment and other components currently under development. Some of the most important criteria are listed below:

- The grating coupler should be compatible with the output from a single-mode Corning SMF-28 optical fiber [41].
- The waveguide should have a strip design, as illustrated on the left side of Figure 2.6 on page 13.
- The grating coupler should be optimized for a wavelength of  $\lambda_0 = 1550 \text{ nm}$ .
- Light should be coupled into a waveguide with a 500 nm width and a 220 nm thickness, which are defined along the x- and y-directions, respectively. These dimensions are commonly chosen for integrated photonics devices, and ensure that only a single mode of each polarization is supported at a wavelength of 1550 nm [42].
- The coupling structures should be made on top of a 1  $\mu\text{m}$  thick silica ( $\text{SiO}_2$ ) cladding that has been grown on a 500  $\mu\text{m}$  thick silicon wafer substrate.
- The grating coupler should be able to couple TE-polarized incident light. This polarization is chosen since its evanescent components do not extend too far into the silica cladding [42] – allowing good confinement even for a 1  $\mu\text{m}$  oxide layer.

As mentioned in the preface, this Master’s thesis is a continuation of the work in my project thesis [1]. The COMSOL models described in the following





**Figure 3.1:** An overview of the geometry of our COMSOL model, where colors are used to indicate which materials are assigned to the different regions. Air regions are colored blue, silicon regions are colored red and silica regions are colored green. The gray regions are not actively simulated areas, and are therefore not assigned any material. Note that the long, narrow rectangle inside the air domain represents the fiber source, and that the interior of this rectangle is colored gray as well. The air gratings in the thin silicon waveguide are colored blue.

sections were initially developed as part of this previous work, but alterations have been made to allow iterative optimization of the individual grating dimensions and the separation between them.

The next section will provide an overview of the geometry of our model, as well as material definitions, physics configurations and modelling of the optical fiber source. We will not cover how this model can be designed in COMSOL, and the reader is instead referred to the COMSOL tutorial provided in [Appendix A](#) on page 82. This appendix features step-by-step instructions on how to make a simple, uniform grating coupler in COMSOL.

### 3.1.3.1 Geometry and materials

The geometry of our COMSOL model is depicted in [Figure 3.1](#), where different colors are used to indicate which materials are assigned to the different model domains. The silicon wafer substrate is colored red, and can be seen at the bottom of the figure. On top of it we find the silica cladding, which is  $1\ \mu\text{m}$  thick and is colored green. The waveguide can be seen as a thin red line between the green cladding and the blue air domain above it. Small, blue air gratings are also present as periodic defects along the waveguide.

Inside the big air domain, there is a thin rectangle that will be used to model the fiber source. The interior of this rectangle, as well as the small rectangles at the endpoints of the waveguide, are not actively simulated areas and are colored gray.

All domains with the same color are also configured with the same material properties. The refractive indices of the silicon, silica and air regions are  $n_{\text{Si}} \approx 3.48$ ,  $n_{\text{SiO}_2} \approx 1.45$  and  $n_{\text{air}} \approx 1$ , respectively [\[43\]](#). These values are theo-



retical, and may deviate slightly from the refractive indices of the materials we will use in manufacturing. The exact properties of the materials used by the research group have not yet been accurately determined due to lack of suitable characterization equipment.

The dimensions of the waveguide and cladding are mostly the same as those given in the requirement list above. However, since we have restricted ourselves to two dimensions, the width of the waveguide is simulated as essentially infinite. The thickness of the substrate is set to  $7\ \mu\text{m}$ , which was found to be sufficient to ensure negligible interactions between electromagnetic fields in the waveguide and the edges of our model geometry. In a real device the silicon substrate would likely be several hundred micrometers thick, but this would require extremely powerful computers to simulate at the mesh resolution we need to ensure simulation accuracy.

The length of the waveguide is also restricted due to processing power and memory requirements, and is set to  $60\ \mu\text{m}$ . This is enough to allow the inclusion of a very high percentage of the optical fiber distribution, as we will discuss in more detail in section 3.1.3.3. It is also sufficiently long to allow a reasonable placement of about 40 gratings – which has been shown to be sufficient to ensure a stable solution in previous work [1].

As with all the other geometry parameters, the size of the air region is restricted by computational limitations. The height of this domain is set to  $25\ \mu\text{m}$ , which is enough to make room for a tilted fiber input at angles up to approximately  $25^\circ$ . This height is also more than enough to ensure negligible interactions between the electric fields and the domain edges, and we will therefore reduce it slightly to allow faster simulations when the incidence angle of the fiber is small.

In a real device, light that is transmitted through or reflected off our grating structures and that is incident on the outer bounds of our model geometry would mostly continue to propagate within the material in the same direction. To ensure that the same situation does not cause light to be reflected off the exterior edges of our model, perfectly matched layer (PML) domains are included at the edges of the air and silicon regions. These PML domains essentially absorb all radiation that is incident on it by virtue of having a complex-valued permittivity and permeability [44].

### 3.1.3.2 Ports

As explained in section 3.1.1, we will be using the frequency domain physics interface in COMSOL. This interface allows us to define *ports*, which can be used to emit or absorb electromagnetic radiation. Ports can be assigned to domain boundaries in our model geometry, and they are capable of measuring the amount of radiation incident on them.

We will be using a total of three such ports in our model. Two of the ports are used to measure the amount of light that is coupled into the waveguide, and are assigned to the waveguide-adjacent boundaries of the gray rectangles on the right and left hand sides of Figure 3.1. These ports are not configured

to emit any radiation, and will only absorb and measure the radiation incident on them.

The coupling of light into the forward direction (positive z-direction) has resulted in higher efficiencies than backward-coupling in previous work [1], and this will therefore be the focus in this thesis as well. The left port is therefore not expected to measure any significant fraction of the total incident light, but is included to verify that this remains correct throughout the simulations in this thesis.

Ports in COMSOL are configured to measure the incident radiation from specific modes in the model geometry. This ensures that we only include light coupled into the waveguide in our measurements, and not light that is simply propagating through the structure, e.g. from above. To find the supported waveguide mode(s), COMSOL can be configured to do automatic boundary mode analyses for specified frequencies and refractive indices.

The ports on the left- and right-hand side of [Figure 3.1](#) are significantly taller than the waveguide itself. This is to ensure that we also include any evanescent components of the electromagnetic fields of the radiation propagating within the waveguide. A concern is then that the ports could include radiation propagating outside of the waveguide mode, but the mode-matching capabilities of the ports in COMSOL makes sure that this is not the case. We can therefore include the evanescent components without worrying about increased noise.

The third port is used to model the fiber output, and is assigned to the bottom boundary of the tilted, gray rectangle inside the air domain in [Figure 3.1](#). The model geometry is configured in such a way that this port can be rotated freely, and makes sure that a normal at center of the port is always pointing towards the exact same location in the grating structure for all angles. The separation between the bottommost part of the fiber and the waveguide is also constant for all angles, and is set to  $3\ \mu\text{m}$ . This separation was shown not to impact coupling efficiencies significantly in [1], and an arbitrary value that placed the fiber fairly close to the waveguide was therefore chosen.

The fiber port is configured to both emit and absorb radiation. In addition to simulating the optical fiber output, we also want to measure the amount of light that is reflected back towards the optical fiber by the grating structure. This allows us to check if coupling losses primarily are caused by back-reflection or if it is mostly due to leakage to other parts of the structure. This will not be a very accurate measurement, as light will likely also be reflected towards parts of the air domain that is not covered by the fiber, but it could at least give an indication of relative losses between runs.

There are no waveguides present in the close vicinity of the fiber source, only air. Since the air region supports much more than a single mode, we have configured the boundary mode analysis to find all available modes for propagation in air. In practice, this will allow light originating from the fiber to propagate relatively freely towards the grating structure. In the next section, we will discuss how the optical fiber source has been modeled in terms of its field distribution.

### 3.1.3.3 Modeling the optical fiber

As mentioned in the beginning of section 3.1.3, the optical fiber we will be basing our simulations on is the SMF-28 optical fiber from Corning Incorporated. It is a single-mode, step-index optical fiber with a mode-field diameter  $MDF = (10.4 \pm 0.5) \mu\text{m}$  and a numerical aperture  $NA = 0.14$  [41]. We can verify that the fiber supports only a single mode by inserting the numerical aperture and  $\lambda_0 = 1550 \text{ nm}$  into (2.33). We then find  $V \approx 2.33 < 2.405$ , fulfilling the single-mode requirement presented in section 2.2.3.1 on page 15.

In section 2.2.3.1 we explained how a Gaussian distribution can be a good approximation for the field distribution within an optical fiber. It is significantly easier to work with than the more accurate Bessel functions, and has therefore been chosen to represent the optical fiber output in our models.

A circularly symmetric 2D Gaussian distribution has been defined where the mode-field diameter of the optical fiber is used as the initial beam diameter, as mentioned in section 2.2.3.1. The distribution is centered at the midpoint of the boundary assigned to the fiber port in our model, ensuring a representative Gaussian for all fiber rotations. The use of relative model coordinates also makes sure that the fiber configuration is correct for all rotations and displacements from its initial position.

As mentioned in section 3.1.3, our structures should be optimized for TE-polarized light. The fiber source is therefore configured to only have non-zero components of the electric field along the x-direction.

Now, like most probability distributions, the Gaussian distribution does not reach zero before we approach infinite y- and z-coordinates. In order to include the entire distribution, we would therefore need an infinitely long fiber port, which is not possible due to memory and processing power requirements. This is an important point, since COMSOL calculates the coupling efficiency as a ratio of the intensity of the input beam and output ports. The inclusion of only a small fraction of the distribution would result in a beam with a small spot size that would be easier to couple into the waveguide. This would artificially improve our end-results, and should therefore be done with care.

Because the majority of the Gaussian distribution is located close to the mean, we can cut off the distribution at some points where the excluded portion of the distribution is only a negligible fraction. We have chosen a fiber port width of  $40 \mu\text{m}$  in our model, which should account for over 99% of the total distribution. This can be shown by integration of the Gaussian distribution (2.30).

## 3.2 Simulation procedures

In this section we will briefly discuss how we have utilized the simulation tools presented in the previous section, discuss the problems we will be trying to solve and explain the iterative methods we have applied to these problems. Section 3.2.1 will cover how the physics of our model has been discretized and how we can verify the validity of this discretization. We then move on to describe the

simulations we have run on two different grating structures in sections 3.2.3 and 3.2.4.

### 3.2.1 Meshing

As mentioned in section 3.1.1, COMSOL applies the relevant PDEs that describe our physics through the use of the finite-element method. Now, as we know from our theoretical discussion in section 2.4.1, this method is prone to errors when the size of the mesh elements is too large. Before we run any data-gathering simulations, we must therefore ensure that our mesh elements are not so big that they to cause inaccurate and unstable solutions.

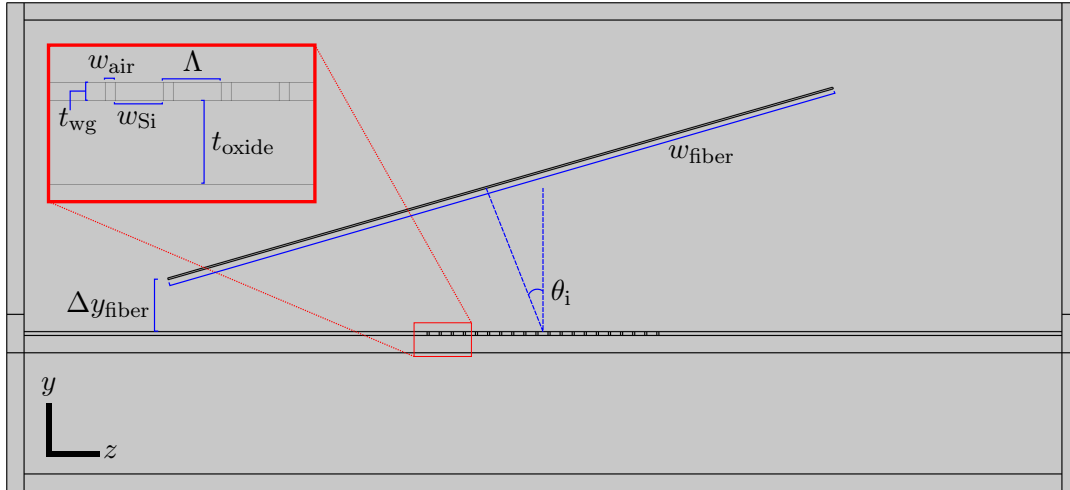
COMSOL has five different parameters that affect how the mesh is constructed. These are the maximum and minimum mesh element sizes, the minimum number of mesh elements across narrow simulation domains, the relative size difference between neighboring elements and a curvature factor that affects meshing at curved boundaries. The values of these parameters are initially set by the software based on the size of the total simulation area and the wavelength, but it is always a good idea to make sure that the mesh is sufficiently detailed.

To ensure accuracy in the finite-element method, the most important parameter is the one that determines the maximum element size. This will therefore be our primary focus when we validate our meshing procedure. We will also set the minimum number of mesh elements across narrow regions to 6, which was found to be more than sufficient to avoid unstable solutions due to edge effects in previous work [1].

The other three parameters will be left at their default values, which was initially suggested by COMSOL based on the model size: 80 nm for the minimum mesh element size, 0.2 for the curvature factor and 1.1 for the relative size difference between neighboring elements. The curvature factor will not affect our model to any significant degree, since we only use rectangular geometry elements. The default values for the last two parameters have also seemed to work reasonably well during initial testing. The three parameters do not seem to have a big impact on our simulations as long as an adequate values are chosen for the maximum element size and the minimum number of mesh elements across narrow regions.

### 3.2.2 Gaussian beam diameter

In section 3.1.3.3 we mentioned that the fiber source in our simulations is based on an SMF-28 optical fiber with a 10.4  $\mu\text{m}$  mode-field diameter. This is the same type of optical fiber that will be used in our laboratory setup for coupling efficiency measurements, which we will cover in more detail in section 3.5.3. However, the fibers in this setup also feature lensed tips, which are taper-like structures that focuses the fiber output on a much smaller area – essentially reducing the beam diameter of the output. The *beam diameter* is analogous to the mode-field diameter, but is used to describe a freely propagating beam rather than the field distribution at the output of an optical fiber.



**Figure 3.2:** Overview of the COMSOL model geometry of the uniform grating coupler discussed in section 3.2.3. The inset shows a zoomed in version of the leftmost part of the grating structure. Important parameters are indicated using blue lines. A description of the different parameters can be found in Table 3.1 on page 34.

To examine the effect of changes to the Gaussian-distributed source, we will therefore run parametric sweeps over different mode-field diameters to see how this affects the coupling efficiency. It is intuitive to think that a more focused beam should be easier to couple into our submicron structures, but it is also possible that adjustments would have to be made to the grating dimensions to accommodate for changes in the input source configuration.

### 3.2.3 Uniform grating coupler

The first model we will run simulations on is depicted in Figure 3.2. The figure includes an overview of the most important parameters that can be adjusted in this model, and a description of these parameters is also provided in Table 3.1 on page 34.

The uniform grating coupler is a grating structure where each air grating has the exact same width and the separation between each grating is the same. This design has already been developed and optimized in previous work [1], where the best coupling efficiency achieved for a completely uniform structure was 44%. We will not repeat the same optimizations here, and will instead build on the results from the project thesis. The simulations on this type of grating coupler will therefore be limited to the verification of experimental results.

Because of this, the simulations we will run on the uniform grating coupler closely resembles the characterization procedures presented in section 3.6.3. We will examine the dependency of the coupling efficiency on the incident angle, the wavelength and the grating dimensions. Further details will be covered as part of the fabrication and characterization discussion later in this chapter.

**Table 3.1:** Important model parameters for the uniform grating coupler. Most of the parameters are also indicated in [Figure 3.2](#).

Parameter	Description
$w_{\text{air}}$	Width of the air gratings
$w_{\text{Si}}$	Width of the silicon sections between the gratings
$\theta_i$	Incident angle
$\Lambda$	Total grating period
$t_{\text{wg}}$	Waveguide thickness
$t_{\text{cl}}$	Cladding thickness
$\Delta y_{\text{fiber}}$	Vertical position of the fiber relative to the waveguide
$\Delta z_{\text{fiber}}$	Horizontal position of the fiber relative to the center of the grating structure
$w_{\text{fiber}}$	Width of the fiber port
$n_{\Lambda}$	Number of gratings

### 3.2.4 Apodized grating coupler

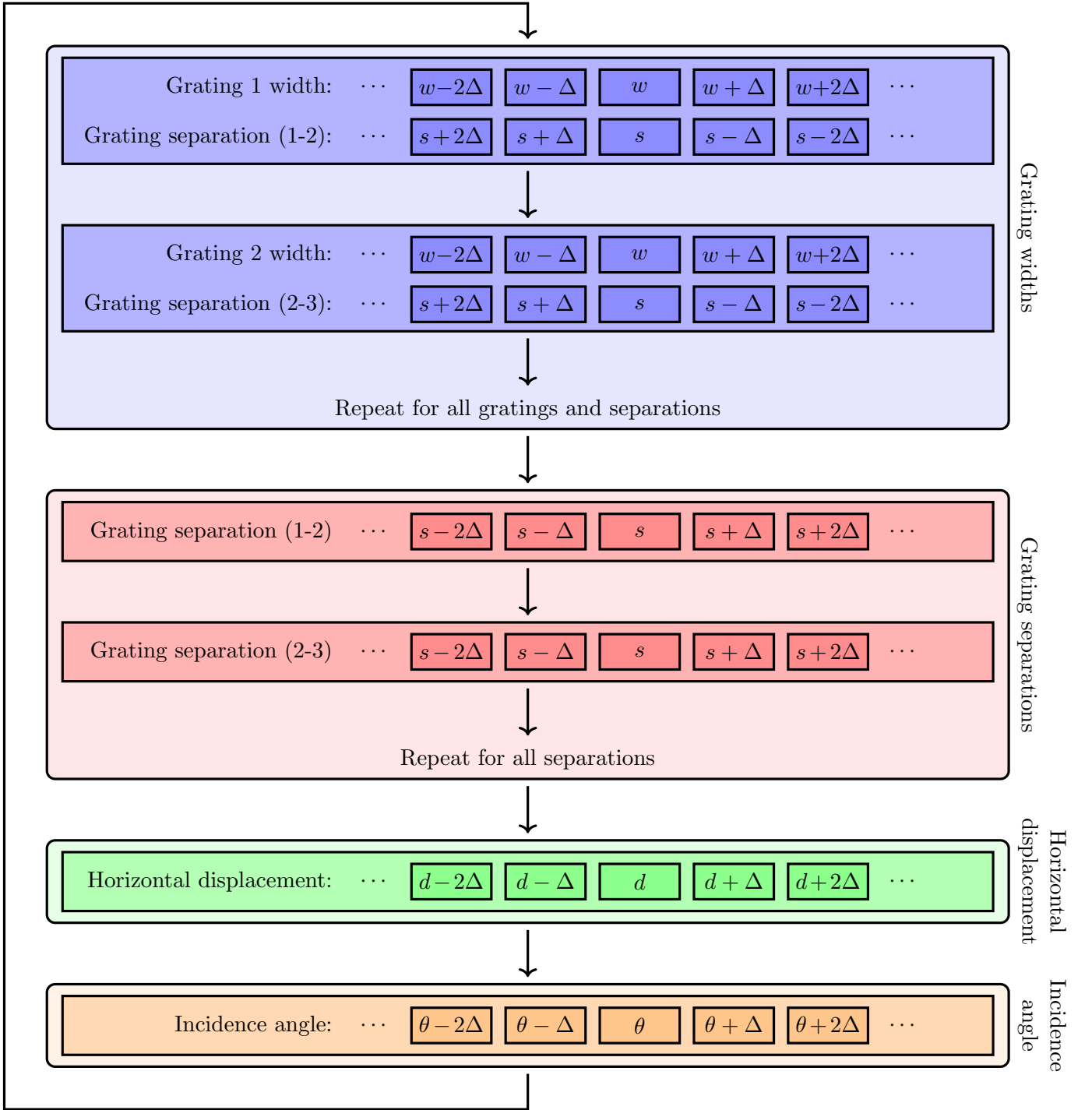
The optimization of an apodized grating coupler has been the main focus for our simulations in this thesis. An *apodized* grating structure refers to a design where the width of every single air grating and the separation between them have been optimized individually. The optimization of such a structure requires a more refined iterative algorithm than a completely uniform grating structure.

The approach we have chosen is illustrated in [Figure 3.3](#) on page 35. We iterate over three sets of parameters that are somewhat related: the individual grating widths, the individual separation between adjacent grating pairs and the horizontal displacement of the grating structure as a whole relative to the focus point of the optical fiber source. A sweep is also done over the angle of incidence for the fiber source.

Two different starting points have been examined for our optimization procedure, both based on the best results found in the project thesis [1]:

1. The first starting point was a uniform grating structure optimized for a  $10^\circ$  incidence angle that featured a 39.8% coupling efficiency. The initial values of the design parameters were  $w_{\text{air}} = 88 \text{ nm}$ ,  $w_{\text{Si}} = 565 \text{ nm}$ ,  $\Delta z_{\text{fiber}} = -8710 \text{ nm}$ ,  $\Delta y_{\text{fiber}} = 3 \mu\text{m}$  and  $\theta_i = 10^\circ$ .
2. The second starting point was a mostly uniform grating structure, but the rightmost air grating was significantly narrower than the rest. This was found to improve the coupling efficiency compared to a purely uniform structure during the project thesis [1]. We will refer to this rightmost grating as the *endslot*. The design used for this second starting point was optimized for a  $16^\circ$  incidence angle and featured a 48.7% coupling efficiency. The initial values of the design parameters were  $w_{\text{air}} = 110 \text{ nm}$ ,  $w_{\text{air,endslot}} = 40 \text{ nm}$ ,  $w_{\text{Si}} = 580 \text{ nm}$ ,  $\Delta z_{\text{fiber}} = -8740 \text{ nm}$ ,  $\Delta y_{\text{fiber}} = 3 \mu\text{m}$  and  $\theta_i = 16^\circ$ .

The COMSOL model used for these simulations has been modified extensively to allow us to change the widths of the gratings and the separation be-



**Figure 3.3:** Flowchart illustrating the optimization process for the apodized grating coupler that we will follow in this thesis. The rounded, light-colored boxes each illustrate the iterations performed to optimize a set of parameter values. The medium-sized boxes within them each correspond to the optimization of a single geometry element or parameter in our model. The smallest, dark-colored boxes each represent a single simulation in the iterative procedure. A detailed explanation of the optimization process can be found in section 3.2.4.



tween them individually. In order to reduce the runtime of each simulation, the number of gratings was reduced to  $n_\Lambda = 21$  by removing the 19 leftmost gratings. Based on previous work, this should only result in a relative change in coupling efficiency of 1 to 2% [1].

Let us now take a more detailed look at the optimization procedure illustrated by the flowchart in [Figure 3.3](#). We start by iterating over some values for the width of the leftmost air grating. The width,  $w$ , is changed slightly by adding some value  $\Delta$ , and the separation between the leftmost grating and the second leftmost grating,  $s$ , is reduced correspondingly to ensure that the rest of the grating structure remains stationary. This last point is important, since a horizontal displacement of the grating structure affects the coupling efficiency as well. The process is repeated for all widths in the range  $\{w - 10\Delta, w - 9\Delta, \dots, w + 9\Delta, w + 10\Delta\}$ . The associated grating separation is changed accordingly. Ignoring the initial value that we have data for already, this amounts to a total of 20 simulations per grating.

The width that results in the highest coupling efficiency is then passed along to the next iteration step, where the width of the second leftmost grating is optimized. The procedure continues until all 21 gratings have been optimized individually.

Now, since we adjust the grating separations to compensate for the grating width changes, we have to iterate over all the grating separations individually as well. In this case, we will only change the separation, and will not alter the width of the gratings at all. These iterations works in the same way: changing the separations one-by-one and checking the coupling efficiency for all values in the range  $\{s - 10\Delta, s - 9\Delta, \dots, s + 9\Delta, s + 10\Delta\}$ , where  $s$  represents the initial values for the grating separations. The parameters that give the best coupling results are passed along to the next iteration steps, as before.

The third parameter that we consider is the horizontal displacement of the entire grating structure relative to the incidence point of the center of the Gaussian-distributed optical fiber source. Every time the separation between two gratings is changed, a fraction of the grating structure is displaced slightly relative to this point of incidence. Failure to compensate for this displacement could reduce the maximum coupling efficiency we can find with this iterative method significantly.

The iteration over this horizontal displacement functions similarly to the previous iterations. The coupling efficiency is tested for all displacement values in the range  $\{d - 10\Delta, d - 9\Delta, \dots, d + 9\Delta, d + 10\Delta\}$ , where  $d$  is the initial displacement.

Any of the above changes can also result in a minor change in the optimal angle of incidence, and we therefore perform a sweep over different angles as well. We check all values in the range  $\{\theta - 10\Delta, \theta - 9\Delta, \dots, \theta + 9\Delta, \theta + 10\Delta\}$ , where  $\theta$  is the initial incidence angle.

At this point we will have iterated over different values for the width of 21 individual gratings, 20 individual grating separations, the horizontal displacement of the grating structure as a whole and the incidence angle. Each value results in 20 simulations, amounting to a total of  $(21 + 20 + 1 + 1) \cdot 20 = 880$



simulations that each takes a couple of minutes to run on the available hardware. A single run over the blue, red, green and orange blocks in [Figure 3.3](#) therefore takes about 25 hours to complete.

This whole process is already quite time-consuming, and a single run is unfortunately not nearly enough to fully optimize the structures. Many sequential runs are required, where the best result from the previous run is continuously fed into the next iteration.

### 3.3 Experimental tools

In this section we will give a brief introduction to the various tools we have used to fabricate our grating coupler prototypes. The descriptions will not be overly detailed, but are intended to familiarize the reader a bit with the instruments before we discuss how we have employed them in our laboratory procedures in [section 3.4](#) on [page 44](#). Since we will be working on silicon-on-insulator (SOI) structures, we will start this section by discussing the advantages and disadvantages of the SOI platform.

#### 3.3.1 The silicon-on-insulator platform

A wide range of materials can be used to confine and transmit light along dielectric conduits. The materials all have their advantages and disadvantages, and it is important to choose the most suitable materials for the problem at hand.

The silicon-on-insulator platform has been used extensively in industry for decades, and has therefore become a highly attractive material in photonic device manufacturing [[7](#), [42](#)]. This is also the platform we will be working with in our experimental procedures. Our primary motivation for this choice is to ensure compatibility with the sensors currently being developed by the photonic research group at NTNU, but we will nevertheless discuss some advantages and disadvantages of this platform to understand better why it was chosen by the group in the first place.

Crystalline silicon (c-Si) features an exceptionally low absorption at wavelengths around 1550 nm [[42](#)], resulting in very low material losses in our coupling and waveguide structures. It is, however, virtually impossible to grow high-quality c-Si on top of amorphous surfaces [[45](#)]. Since the silica cladding used is thermally grown and amorphous, we must therefore turn to amorphous silicon (a-Si) instead.

The properties of a-Si are mostly the same as that of c-Si, but the absorption is significantly higher for the relevant wavelengths due to dangling Si-bonds [[45](#)]. This can be somewhat remedied by hydrogenation of the bonds if silane-based (SiH<sub>4</sub>) plasma-enhanced chemical vapor deposition (PECVD) techniques are used for the a-Si growth [[45](#)]. We will discuss this further in [section 3.3.2](#) on [page 38](#).

A great advantage of the SOI system is that there is a very high contrast between the refractive indices of silicon and silica. According to [[42](#)], the contrast

is in fact higher than any other material system presently utilized for integrated photonics, which results in several favorable properties. First of all, the dimensions of the waveguide can be made extremely small. As mentioned previously, our waveguide dimensions will be 220 to 500 nm, whilst e.g. glass waveguides structures needs to be on the order of 10  $\mu\text{m}$  to confine the same light [42].

Since our SOI structures have sub-wavelength dimensions, the evanescent components of the light propagation within them will interact with any adjacent materials – which changes the effective refractive index of the waveguide material, like we discussed in section 2.4.2.1. This is essential for the research group, as it is the basis for the working principle of the biosensors being developed [2–4]. The high refractive index contrast also results in a more wavelength-dependent refractive index, which strengthens the biosensing capabilities of the sensors.

The ease of manufacturing scalability is very important for device development. It is therefore very beneficial that the SOI platform is compatible with existing CMOS manufacturing processes [7]. Mass production is readily facilitated through the use of thoroughly-researched, well-established fabrication tools and procedures – shortening the path from functioning prototype to commercially viable product.

### 3.3.2 Plasma-enhanced chemical vapor deposition

Plasma-enhanced chemical vapor deposition (PECVD) is a technique used to deposit thin films of many different materials, such as silicon dioxide ( $\text{SiO}_2$ ), silicon carbide ( $\text{Si}_3\text{N}_4$ ) and a-Si [46]. The instrument features a vacuum chamber into which precursor gases are pumped. Parallel conducting plates generate radio frequency (RF) power which energizes and ionizes the precursors molecules to create plasma. The resulting plasma then consists of highly reactive radicals that react chemically with the wafer substrate, forming a thin film through bond formation and diffusion [46].

The use of plasma to energize precursors allows the PECVD to operate at significantly lower temperatures than regular chemical vapor deposition (CVD) processes. This allows more flexibility in the choice of thin films and substrates, and the ability to use cold-wall reactors also reduces particle contamination in the chamber [46]. PECVD supports high deposition rates, and features good uniformity, adhesion, step coverage and low pinhole density overall [47].

### 3.3.3 Scriber

*Scribers* are tools that are used to cut and break wafers into smaller pieces along straight lines. They come in many different shapes and sizes, and some are even integrated in more sophisticated automatic systems. Their working principle is very simple, and involves scratching a shallow straight line on the surface of a wafer substrate using a diamond tip. This introduces a weakness in the material, which causes the sample to break along the line when sufficient pressure is applied [48].

Their use is slightly different for crystalline and non-crystalline samples. In the former case, the anisotropy of the material causes it to break more easily along specific crystal planes. A small line defect along this plane is then sufficient to break the sample efficiently, and it is unnecessary to scratch a line across the entire sample. In the non-crystalline case, on the other hand, there are no crystalline planes. It is therefore important to ensure that the weakness spans across the entire substrate before breaking it. Otherwise, the sample is likely to shatter or break along random directions.

A challenge with scribes is that one often has to touch the surface on both sides of the substrate to break it efficiently. This could damage the sample and any existing structures, as well as introduce impurities. The sudden movement of the sample when it breaks could also cause damage to fragile structures, such as high-aspect ratio gratings. It is therefore often preferred to use automated systems that are designed to minimize damage to the sample or scribe samples before any fragile structures are grown on them.

There is a somewhat different scribe available in NTNU Nanolab as well, which functions more like an automated diamond saw. Sawing the substrate instead of breaking it drastically reduces the risk of damage to the sample. It is also more predictable, since we do not rely on the crystalline material to break in a straight line by itself along the crystal planes. In the case of cutting a sample for butt-coupling, however, the sawing technique could be more destructive to the waveguide than the aforementioned scratching and breaking.

The diamond tip of all scribing systems has a tendency to deteriorate when used, especially when applied to harder materials. This can be especially problematic in a multi-user environment where scribes are used for many different materials daily, and where everyone has different requirements and expectations. It is therefore important to take great care when handling the scribe tips.

### 3.3.4 Ultrasonic bath

An ultrasonic bath is an instrument that enables efficient cleaning of wafer substrates by submersion in a liquid that is agitated by high-frequency acoustic waves. Acoustic vibrations result in microstreaming of the liquid at the surface of the wafer, which has been shown to be efficient at removing particles that are 0.3  $\mu\text{m}$  or bigger [49].

The formation and collapse of microcavities in the fluid have been found to cause damage to sample structures, but this should not be a serious issue when working with unpatterned silicon wafers. The interested reader is referred to [50] for a more in-depth explanation of the mechanisms behind ultrasonic cleaning.

Ultrasonic baths usually feature containers with quite high volumes, which could make it impractical and expensive to fill them with the ideal sample-cleaning solvent. It is therefore common to place the sample in a small beaker filled with this solvent, and then submerge the beaker partially in a ultrasonic bath filled with deionized (DI) water. This both reduces the amount of solvent needed and avoids water contaminating the content of the beaker.

### 3.3.5 Plasma cleaner

We have already discussed the plasma-based PECVD in section 3.3.2. Plasma cleaners function in a similar manner, by using RF energy to ionize a low-pressure gas to form a highly-energized plasma. The big difference between the two instruments is that they use different gases: the ionized PECVD precursors react with the sample to form a thin film while the ionized gases in the plasma cleaner form highly destructive radicals that can etch various materials, strip photoresist and condition wafer surfaces [50] for subsequent processing.

O<sub>2</sub> is a gas that is used frequently for plasma cleaning. When partially ionized by the RF source, it dissociates to form reactive species such as O<sub>2</sub><sup>-</sup>, O<sup>-</sup>, O<sub>2</sub><sup>+</sup> and O<sup>+</sup>, as well as oxygen radicals and species energized to higher quantum states [50]. The high reactivity of these species allow photoresist to be removed at a quite fast rate.

### 3.3.6 Electron-beam lithography

*Lithography* is a manufacturing process that enables the construction of patterned geometries on top of wafer substrates using controlled exposure to different types of radiation [46]. This is achieved through the use of materials that undergo drastic changes in their solubility properties when being subject to electromagnetic radiation or electron beams. We call these materials *resists*.

The traditional form of lithography is *photolithography*, which is based on light-sensitive resists. It is still very attractive due to its low cost and high throughput for mass fabrication, but the maximum resolution that can be achieved is restricted by the diffraction limit of light [51]. Light-based techniques also require *masks* to be created, which protect the regions of the resist that should not be exposed to light. These masks add additional fabrication steps, and are not very well suited for explorative prototyping.

Lithography techniques based on electron beams provide much better resolution limits [52], and instruments can be constructed that use electric fields to scan across the entire sample without the use of masks. We call this technique *electron-beam lithography*, or EBL for short. The abbreviation is also used to refer to the instruments themselves. EBLs are very practical for prototyping purposes, since they can expose resist patterns based on computer-made design files. They are also often used to produce masks for other lithography techniques.

The lithography process consists of many steps, and the exact procedure is highly dependent on the choice of material and photoresist, as well as the pattern design. We will outline the main process steps here, but will not discuss the details of our lab procedures. The specific process parameters that we have used in the experimental part of this thesis will instead be covered in section 3.4.

The number of steps in the lithography process varies a bit between textbooks, but we will follow the 8-step model that is presented in [46]. The referenced book primarily focuses on photolithography, but the basic procedural principles are mostly the same for EBL. The book is also the primary source

for all material presented in sections 3.3.6.1-3.3.6.3 and 3.3.6.5-3.3.6.8.

### **3.3.6.1 Vapor prime**

This first step focuses on preparing the wafer substrate for subsequent processing. The wafer is cleaned to get rid of any contaminants and dust particles, for example through the use of an ultrasonic bath. Plasma cleaning could also be employed to get rid of any residues or bigger particles.

In addition to the removal of particles it is also important to ensure that the wafer surface is dry and that it contains a minimal amount of water molecules. This improves adhesion between the wafer surface and the resist, and is important to achieve a good result. The wafer is therefore often subject to a dehydration bake after it has been cleaned. This involves placing the wafer on a hot-plate at high temperatures for a few minutes. As a final step, the wafer surface is often primed with an adhesions promoter, such as hexamethyldisilane (HMDS).

### **3.3.6.2 Spin coat**

After the sample has been thoroughly cleaned and dried it is time for the application of resist. This is done by placing the wafer sample on a vacuum chuck that can spin at several thousand rotations per minute (RPM). A small amount of liquid resist is applied to the center of the sample and it is then spun at high-RPM for some time, causing the resist to spread out and form a thin film on the surface. The speed and duration of the rotation determines the thickness of the resulting resist layer. The thickness is inversely proportional to the square root of the spin speed, and spin curves are usually provided in resist datasheets.

Spin coating is particularly prone to defects, as even a single particle can ruin the quality of the resulting resist film. Long time delays between the application of resist and spinning can also result in defects if the resist starts drying quickly. A careful and consistent procedure is therefore necessary to ensure good results.

### **3.3.6.3 Soft bake**

To further improve adhesion between the wafer and the resist, the sample is placed on a hot plate immediately after spin coating. This also serves to relieve stresses in the film and evaporate excess solvents from the resist. Soft bake processes typically occur at about 100 °C for about a minute, but this varies from resist to resist. Inadequate soft baking can result in resist cracking, adhesion problems, increased susceptibility to particle contamination and low solubility contrast between exposed and unexposed areas.

### **3.3.6.4 Alignment and exposure**

Alignment of the sample can be a major challenge in many lithography systems, but is fairly straightforward in an EBL. The resist-coated wafer is simply placed on a mounting stage which has predefined slots where the sample can be

fastened. The mounting stage is then transported to the main chamber, where the exposure occurs. It is important to ensure that the sample is clean on the backside to avoid tilt, but the mounting procedure is otherwise simple.

Loading of the sample is done in a load-lock in order to maintain a constant vacuum in the main EBL chamber. This is important to reduce contamination and ensure beam stability. Once the sample is loaded into the main chamber the risk of further contamination of the resist film is therefore very low.

As mentioned previously, the EBL is configured using computer-generated design files. The initial design is first made in a layout editor, such as CleWin [53], and is then processed in various ways to improve the accuracy of the exposure. When a design layout is made, it is important to ensure that we do not have overlapping design elements, as this could cause excessive exposure of these areas. This can easily be corrected by software such as Beamer [54].

More sophisticated corrections can also be made to account for proximity effects, which is a scattering-induced widening of the electron beam that can cause resist outside the intended area to be exposed [3]. This is called proximity error correction (PEC), and can also be performed in Beamer provided that we input the relevant resist exposure analysis. Such an analysis can be calculated using e.g. TRACER [55], which performs a Monte Carlo simulation to determine the behavior of the electron beam upon impact with the resist.

Now, the EBL exposure itself works by scanning over the resist with an electron beam that iteratively focuses on a matrix of spots that partially overlap. The size of these spots and their separation can be changed, but there is a trade-off between the resolution and duration of the lithography process. For designs with very small critical dimensions, the resolution is the primary concern and smaller beam widths are therefore preferred, but it is also helpful to reduce the duration of the process to allow more efficient fabrication.

The movement of the electron beam is achieved by the use of electric fields that deflect the negatively charged electrons. When the deflection is too high, however, the angle of the beam can cause undesired effects, such as skewed structures. EBLs therefore operate with *write fields*, which restrict the areas the deflected beam can cover before the sample and the electron source have to be physically moved relative to each other. The dimensions of the write fields are usually customizable, and the number of spots in the focus spot matrix for the electron beam is specified on a write field basis. Stitching errors at the write field edges have been a major problem for lithography processes, but improved corrections in modern EBLs have reduced this problem significantly [56].

We have already mentioned how the resist undergoes solubility changes. This occurs locally in the EBL where the resist is bombarded by electrons from the electron beam. The chemistry of the resist is designed in such a way that its solubility in a special solvent, referred to as a *developer*, either increases or decreases when the electron beam is incident on it. If exposure increases the solubility we call it a *positive resist*, and conversely a *negative resist* if the solubility decreases upon exposure. This is the phenomenon that allows us to remove parts of the resist and thereby forming a pattern.



### **3.3.6.5 Post-exposure bake**

Some resist types require a baking step after exposure to catalyze and complete the chemical reactions that affect the solubility in the exposed regions. This step can be omitted for most resist types, but is included here for completeness.

### **3.3.6.6 Development**

In this sixth step, the sample is submerged in a developer that dissolves the exposed areas for a positive resist and the unexposed areas for a negative resist. The remaining resist then forms a pattern that can be used as a protective mask for the underlying structures in subsequent processing, e.g. during etching, ionization, metallization or other deposition processes.

The duration of the development needs to be optimized, since excessive or insufficient development can result in over- or underdeveloped structures, respectively. In an ideal world, there should be a very abrupt solubility change between the exposed and unexposed areas, but this change is usually more gradual due to the proximity effects discussed in section 3.3.6.4. Suboptimal development can result in defects such as inclined side-walls and resist residues remaining in areas that should have been fully developed.

### **3.3.6.7 Hard bake**

A post-development baking step is used for some resists to further improve adhesion and evaporate solvents. The heat dehydrates the sample, removing both water molecules and developer residues, and hardens the resist to make it more resistant to any subsequent etching procedures.

### **3.3.6.8 Develop inspect**

This final step simply involves inspection and characterization of the resist layer to ensure that the quality is adequate. If this is not the case, the resist layer can easily be removed by a resist-stripping chemical and the process can be started all over again. Characterization tools and procedures we have used in this thesis will be covered in detail in sections 3.5 and 3.6.

## **3.3.7 Inductively coupled plasma reactive-ion etching**

Inductively coupled plasma reactive-ion etching, or ICP-RIE for short, is a dry-etching technique that is widely used for anisotropic material removal in semiconductor manufacturing [46]. It uses both physical ion bombardment and active chemical processes to etch away material, and features a low-pressure reactor that is capable of producing highly anisotropic sidewall profiles even for high-aspect ratio structures.

Inside the etch reactor, samples are placed on an RF-powered electrode that is parallel to the grounded electrode at the top of the reactor. The electric field resulting from the high voltage difference between the two electrodes causes charged ions to accelerate rapidly towards the wafer, gradually etching their

**Table 3.2:** An overview of the models and manufacturers of the instruments that have been used in the experimental part of this thesis. Apart from the scriber, all instruments are located in the NTNU Nanolab cleanroom.

Instrument	Model	Manufacturer
PECVD	PlasmaLab System 100 PECVD	Oxford Instruments
Scriber	DAD3220	DISCO Corporation
Ultrasonic bath	–	PM Plast Sweden AB
Plasma cleaner	Femto	Diener Electronics
EBL	ELS-G100	Elionix
ICP-RIE	PlasmaLab System 100 ICP-RIE 180	Oxford Instruments

way into the material. The electric field also provides a strict directionality for the ions, which enables the highly anisotropic etching [46].

There are several different types of reactive-ion etching reactors. The ICP-reactor uses a spiral coil to generate plasma through partial ionization of the etching gases. The use of both an RF-source and the spiral coil allows individual control over the ion density and ion energies [57], facilitating process optimizations.

The etch rate of the ICP-RIE process depends heavily on both the material being etched and the chemical species introduced into the process chamber. It is therefore possible to design a process where one material is etched significantly more than another. The relative etch rates of two materials is usually referred to as the *selectivity* and is usually given as a ratio.

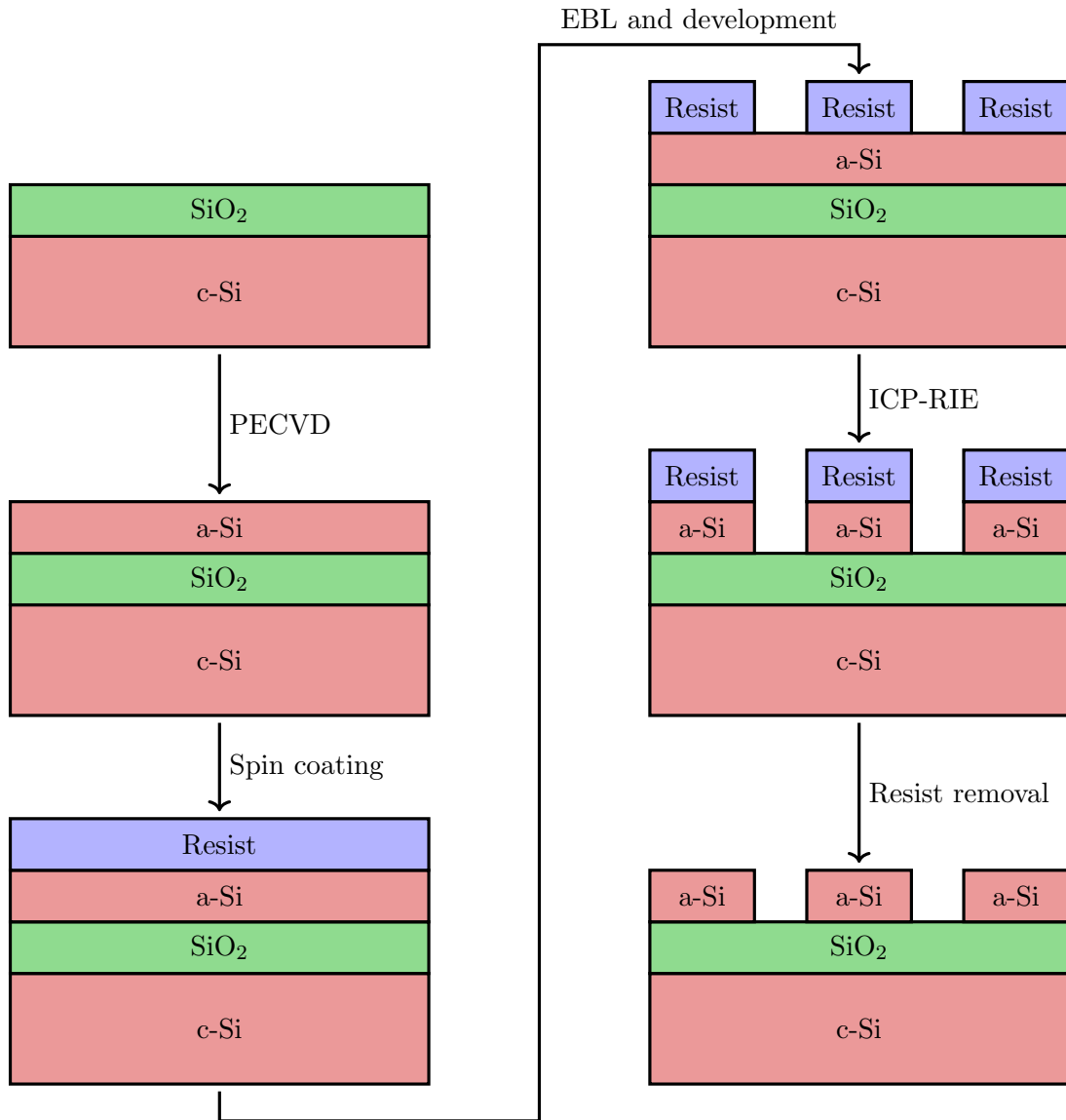
### 3.4 Experimental procedures

We have now covered the basics of the tools and instruments we will be using in this thesis. This section will be devoted to a detailed description of the experimental procedures we have followed while developing our grating coupler prototypes. To make the discussion easier to follow, we have included a schematic outline of the fabrication process, which can be seen in [Figure 3.4](#) on page 45.

The starting point for our grating coupler fabrication procedure is a 500  $\mu\text{m}$  thick crystalline silicon wafer with a 4 inch diameter and a 1  $\mu\text{m}$  layer of thermally grown silica. Because of difficulties depositing an oxide layer of sufficient quality, the silica-covered wafer was bought from a third-party vendor.

Apart from the saw-based scriber, all the instruments we have used for fabrication in this thesis are located in the NTNU Nanolab cleanroom, which is a part of The Norwegian Micro- and Nanofabrication Facility [58]. An overview of the specific models of the instruments we have used is provided in [Table 3.2](#), and all process parameters we will discuss in the following sections refer to the parameters as they are defined within the respective instruments' user manuals and software.





**Figure 3.4:** Schematic outline of the process used to fabricate patterned silicon structures in this thesis. Arrows indicate the order in which the steps are performed, and the main techniques and instruments used are also included. Resist layers are colored blue, silica (SiO<sub>2</sub>) layers are colored green and silicon layers are colored red. Note that there are both crystalline and amorphous silicon layers, marked c-Si and a-Si, respectively. Also note that the relative widths and thicknesses of the layers are not to scale.

**Table 3.3:** A summary of the values of the most important parameters used during the PECVD procedure. This deposition recipe should result in a 220 nm thick layer of a-Si.

Parameter	Value
LF Power	200 W
Pressure	500 mTorr
Stage temperature	300 °C
Gas flow SiH <sub>4</sub>	50 sccm
Gas flow Ar	150 sccm
Growth time	170 s

### 3.4.1 Thin film deposition

The wafer samples were cleaned thoroughly prior to any deposition processes by submerging them in acetone-filled beakers and placing them in an ultrasonic bath for 1 min. They were then immediately rinsed in isopropanol (IPA) to avoid any residues forming as the acetone evaporated, and were then blow-dried using N<sub>2</sub> gas.

Nanolab is a multiuser environment, which results in a wide range of different materials being processed in the same instruments on a weekly, or even daily, basis. It was therefore deemed necessary to run conditioning steps prior to all deposition processes. A conditioning step simply involves running the recipe we are planning to use on a dummy wafer first to ensure that there are no residues left in the PECVD chamber from the previous users. Nanolab also enforces a strict policy that requires all PECVD recipes to include thorough pumping and N<sub>2</sub> purging steps to minimize any chamber contamination from previous processes. We are therefore quite confident that this type of contamination should not be a significant problem. The pumping and purging steps also function as a safety measure to avoid exposure to process gases.

The deposition of a thin layer of a-Si was done using the PECVD process parameters listed in Table 3.3. This process recipe has been optimized by the photonic research group at NTNU to yield an approximately 220 nm thick silicon layer, which should ensure single-mode propagation. The conditioning step was run using the same parameters, with the exception of the growth time, which was increased to 3 minutes to make sure that the chamber was properly conditioned.

### 3.4.2 Scribing

Initial testing of the entire fabrication procedure was done on smaller wafer fragments that were scribed manually from a full-size wafer using handheld, pen-shaped scribers provided by Nanolab. We later transitioned to an automated scribing system that allowed us to scribe entire 4 inch wafers into 10 mm × 10 mm pieces using a diamond saw. This automated scribing process was carried out by Nanolab staff due to instrument licencing requirements. Attempts were made with a different automated scribing tool that we did have

a licence for, but problems with a damaged diamond tip caused us to stick to the saw-based instrument for the majority of the thesis.

### 3.4.3 Design preparation

The transition from a COMSOL model to a process file that is compatible with the EBL system involved several different steps. We first needed to make a two dimensional layout that marked the areas that should be exposed to the electron beam. This was done using CleWin [53], which is a layout editing software designed for mask creation and other similar purposes.

Initial designs were made using CleWin, but it quickly became cumbersome to manually make many similar, but slightly different designs. Luckily, one of the file formats supported by CleWin, Caltech Intermediate Format (CIF) [59], is based on plain text. Using the combination of CleWin and a simple text editor, this allowed us to reverse-engineer the way geometry elements were defined and write our own mini-library for MATLAB that we could use to generate geometry elements more efficiently. By writing some more MATLAB scripts, we used this to generate layout files that included many variations of our grating coupler structures.

The generated layout files were imported to a software called Beamer [54], which was used to fix any overlapping geometries, divide the design into EBL write fields and apply proximity error corrections (PEC). The PECs were based on a resist exposure analysis from a different piece of software, Tracer [55], which was configured to run a Monte Carlo simulation on our material stack for one million incident electrons. After all corrections were finished, the resulting design files were saved in the Elionix CON format, which is fully compatible with the EBL system.

The EBL used in this thesis comes with a layout editing and job scheduling software called WecaS. It provides much of the same functionality as CleWin and Beamer, but is more cumbersome to work with and lacks some useful features that these other two programs can provide – such as PEC. We have therefore chosen to only use WecaS for job scheduling, and have instead included most process parameters and configurations in the CON-file exported by Beamer. We will discuss these parameters and configurations in more detail in section 3.4.5.

### 3.4.4 Application of resist

All samples were extensively cleaned prior to spin coating. Similarly to the 4 inch wafers we started with, they were submerged in acetone and placed in an ultrasonic bath for 1 minute. They were also rinsed in IPA immediately afterwards and blow-dried with N<sub>2</sub> gas, as before. Samples were then plasma cleaned at a 50% oxygen flow and 50% power for 2 minutes to remove any remaining contamination.

To improve adhesion between the wafer and the resist, all samples were subject to a dehydration bake at 150 °C for 5 minutes. A standard hotplate was used for this purpose, and a clean 4 inch silicon wafer was used between samples and the hotplate to avoid contaminants.

**Table 3.4:** A summary of the values of the most important parameters used during the EBL exposure procedure.

Parameter	Value
Area dose	150 $\mu\text{C cm}^{-2}$
Dot number	1,000,000
Write field size	500 $\mu\text{m} \times 500 \mu\text{m}$
Beam current	1 nA
Aperture size (OLAP)	120 $\mu\text{m}$
Beam diameter	2.3 nm

Samples were transferred from the hotplate to the vacuum chuck of the spin coater and centered. Two drops of positive resist were applied to the center of the sample using a clean pipette, and it was then spun at 4000 RPM for 60 s, with an acceleration of 1000 RPM/s. The resist used was a mixture of 17.059 g CSAR 62 [60] and 12.063 g anisole. A second batch of diluted resist was also used, which was made from 8.5 g CSAR 62 and 6.0 g anisole.

After spin coating the backside of the samples were immediately cleaned using a swab with IPA to remove resist traces, before they were placed on a hotplate and soft baked at 150 °C for 1 minute. After a quick optical inspection to verify the quality of the resist layer, they were placed in clean wafer carriers to protect them from contamination.

### 3.4.5 Exposure

Prior to exposure, all samples were carefully placed on an EBL-compatible metal stage and fastened using pre-mounted clamping mechanisms. The metal stage is shared among all Nanolab users, and its layout has been mapped in the EBL software to facilitate alignment and exposure. The EBL itself is extremely sensitive to noise, and is therefore located on a solid block that is not in contact with the surrounding floor tiles. This avoids vibrations from cleanroom users walking nearby. It is also enclosed in its own room by glass walls to minimize disturbances due to air flow.

All samples were exposed individually to allow development and subsequent processing to be completed immediately afterwards. This should reduce contamination and allow us to inspect and characterize our grating structures before more samples are processed. Adjustments can then be made to the recipe or the grating design to correct any observed defects or suboptimal fabrication results.

A summary of the values we have used for the most important EBL parameters is provided in Table 3.4. We have already discussed the write fields in section 3.3.6.4 on page 41, and the dot number refers to the number of spots along each dimension of the focus spot matrix mentioned there. The total number of spots the electron beam focuses on per write field is therefore given by the square of the dot number.

The values listed in Table 3.4 have been constant throughout all grating

coupler fabrication procedures, and have been chosen to ensure compatibility with the biosensing device being developed by the photonic research group at NTNU. The only parameter we have varied is the area dose, which we have iterated over to perform a dose test.

#### 3.4.5.1 Dose testing

We are limited to the processing parameters used by the research group for compatibility reasons, but we have nevertheless examined the effect of the area dose on our fabricated structures. This was done both to get a better understanding of the lithography process and to assess whether or not  $150 \mu\text{C cm}^{-2}$  was an optimal value for this manufacturing process.

To examine the effect of changing the area dose, we made a design that featured a set of 12 straight silicon lines with thicknesses ranging from 20 nm to 1000 nm. Their vertical heights were 220 nm, similar to our grating structures. Now, a total of 13 such sets of lines were combined into a single design file, where each set was configured with different area doses. Linearly spaced values were used, ranging from  $120 \mu\text{C cm}^{-2}$  to  $180 \mu\text{C cm}^{-2}$ . All structures were also subject to a PEC step to accommodate for any proximity errors during exposure. Since we planned to use PECs for our grating coupler designs, it was important that this was included for the dose test as well to ensure that the fabrication processes were as similar as possible.

#### 3.4.5.2 Grating coupler fabrication

In our simulations we have focused on two different grating designs: uniform structures and apodized structures. When transitioning to fabrication, we have primarily chosen to work with the uniform grating structures. Even though this design was expected to feature lower coupling efficiencies, its simplicity should make it significantly easier to optimize the fabrication procedure and find optimal values for the grating dimensions and the separation between them.

The starting point for our fabrication was the uniform grating coupler with the highest coupling efficiency that was found during the project thesis [1]. As mentioned in section 3.2.4, this structure had air grating widths  $w_{\text{air}} = 110 \text{ nm}$  and separations between them  $w_{\text{Si}} = 580 \text{ nm}$ . A total of 30 gratings per grating coupler was used, which was found to be sufficient in [1].

Now, slight deviations from the intended dimensions should be expected. Our simulations do not account for issues such as surface roughness or slanted sidewalls, which is likely to be present to some degree in a physical device. Many steps in the fabrication process will also be conducted manually, which will likely result in minor procedural discrepancies from device to device. Suboptimal values for the EBL area dose could also cause grating widths to become too wide or too narrow, at the expense of the grating separation.

To account for such deviations, we therefore included an array of uniform grating couplers on each sample with slightly different dimensions. The grating period  $\Lambda$  was kept constant at 690 nm for all our structures, while we iterated over the widths  $w_{\text{air}}$  and  $w_{\text{Si}}$ .

In order to make a structure that is compatible with the biosensing LOC device being developed by the research group, we have to include taper couplers in our designs as well. Losses in taper structures have not been covered in our simulations, but Fu et al. have previously shown that the losses in a linear taper structure should be less than 1.7% if the length of the structure is more than 300  $\mu\text{m}$  [25]. We have used a length of 500  $\mu\text{m}$  to ensure even lower losses.

Now, it is difficult to measure the amount of light that is propagating within a narrow waveguide. It was therefore deemed practical to use one grating coupler and one taper coupler at each endpoint of the waveguide. This would allow light to couple into our grating and taper structures, propagate along the waveguide and then couple out of the device in a similar manner. The in-coupling and the out-coupling should feature the same coupling efficiency due to the reciprocity theorem, which was discussed in section 2.3.4. The length of the waveguide was chosen to be 2 mm, which should be long enough to ensure that we can couple light in and out of our devices without unwanted reflections causing noise and affecting measurements.

### 3.4.6 Development

All samples were developed immediately following the EBL exposure to minimize dust accumulation and contamination in general. The developer AR 600-549 from ALLRESIST GmbH [61] was used, and samples were submerged in this developer for one minute with gentle stirring. To stop the development process, samples were then immediately moved to an IPA-filled beaker where they were kept for one minute. This step also featured gentle stirring, and some additional clean IPA was carefully sprayed on the sample afterwards to wash off any remaining traces of the developer. Samples were then blow-dried with  $\text{N}_2$  gas.

### 3.4.7 Etching

Prior to etching, all developed samples were subject to plasma cleaning at 50% oxygen flow and 50% power for 30 seconds to reduce contamination and get rid of residues at the bottom of the resist trenches. Only a very thin layer of resist will be removed by this short cleaning step, and the damage to the unexposed areas of the resist should therefore be negligible. Afterwards, samples were then loaded into the ICP-RIE and processed using the parameters listed in Table 3.5 on page 51.

This recipe should etch approximately 250 nm of silicon, which is 30 nm more than the height of our coupling and waveguide structures. This was done intentionally to include a margin of error and should not affect the underlying silica layer significantly due to the relatively high selectivity of the etch. According to [3], the selectivity should be 5.1:1, meaning that the etch rate of the oxide layer should be only  $1/5.1 \approx 19.6\%$  of the etch rate of silicon.

**Table 3.5:** A summary of the values of the most important parameters used during the ICP-RIE procedure. This recipe should etch approximately 250 nm of silicon.

Parameter	Value
RF power	40 W
ICP power	600 W
Pressure	15 mTorr
Table temperature	20 °C
Gas flow SF <sub>6</sub>	7.5 sccm
Gas flow CHF <sub>3</sub>	50 sccm
Etch time	47 s

### 3.4.8 Resist removal

Our structures are essentially finished after the etching step, but they are still partially covered by a protective resist layer. The removal of this layer is traditionally done by submerging the sample in a resist-stripping solution, but the research group have previously experienced some damage to high aspect-ratio structures using this method. Even though our structures feature lower aspect-ratios, we have therefore chosen to use a different method for compatibility reasons – namely plasma cleaning.

Our samples were plasma cleaned at 100 % oxygen flow and 100 % power for 15 minutes to remove the entire resist layer. Simple optical inspections were done to ensure that this was sufficient and that there were no residues remaining. Samples were then placed in clean sample holders to protect them from contamination until they could be property tested and characterized.

## 3.5 Characterization tools

In this section we will describe the instruments we have utilized to inspect and characterize our samples, as well as the laser setup we have used to measure the coupling efficiencies of our structures. We will start by describing the optical microscope in section 3.5.1, before we move on to discuss the scanning electron microscope in section 3.5.2. Both of these instruments are located within the Nanolab cleanroom facility, while our laser laboratory is located at the Faculty of Information Technology and Electrical Engineering at NTNU. The laser setup will be covered in 3.5.3.

### 3.5.1 Optical microscopy

Optical microscopes are instruments that use light and lens systems to enable imaging of small objects and structures. They have been widely used in semiconductor manufacturing to inspect wafer surfaces and look for defects – such as scratches and particle contamination [46]. The resolution of these microscopes depends on the lens systems used, but is fundamentally limited by the wave nature of light. This limitation is often discussed in terms of the Rayleigh



criterion, which dictates when we should consider two light components in a diffraction pattern to be resolved [62].

Despite their limitations, optical microscopes are frequently used for a wide range of applications. They are quick, versatile and provide a simple way to inspect many different types of samples. The typical magnification of optical microscope systems is usually less than 1000 times [46], but better resolutions can be achieved by more sophisticated systems. For high-resolution imaging of submicron structures it is nevertheless often necessary to use electron-based microscopy techniques.

### 3.5.2 Scanning electron microscopy

The scanning electron microscope (SEM) has been the dominant imaging tool for submicron structures for over 20 years [46]. It functions by creating a high-velocity focused beam of electrons that is scanned across the sample of interest. Upon impact, these electrons are scattered and excite atoms close to the sample surface. Backscattered electrons, as well as *secondary electrons* being emitted from these excited atoms, are analysed by detectors inside the SEM chamber. X-rays and other photons are also emitted in the process, but play no part in the SEM imaging [46]. They are, however, important for other imaging techniques that are often combined with the SEM – such energy-dispersive X-ray spectroscopy (EDS) [63], which enables mapping and analysis of the elemental composition on the sample surface, and focused ion beam (FIB) tools [64].

The velocity of backscattered electrons is dependent on the masses of the nuclei that they interact with, increasing contrast between lighter and heavier elements. Backscattered electrons also penetrate deeper into the sample than secondary electrons, providing more information about the bulk. This does however reduce contrast when imaging surface structures. Both types of electrons are detected by the SEM, and it is often possible to adjust the acceleration voltage and current of the electron beam to optimize image quality.

The use of an electron beam enforces some restrictions on both instrument and samples. Both magnetic lenses and electrostatic focusing elements are required to create the high-energy beam, and a vacuum chamber is required to ensure beam stability. Samples have to be conductive to avoid overheating, and non-conductive samples will therefore often have to be covered with a thin metallic layer before imaging. Highly magnetic samples are also problematic, as they can distort the electron beam and reduce image quality. In some cases, magnetic samples can even cause damage to the instrument.

For non-magnetic, conductive samples the SEM is phenomenal for characterization and inspection. It can achieve magnifications of 100,000 to 300,000 times, and provides resolutions on the order of 4 to 5 nm [46]. The imaging technique is also usually non-destructive, allowing subsequent processing or characterization to take place. Drivers and software often provide a simple way to adjust focus and beam parameters, making the SEM a practical and powerful characterization tool.



### 3.5.3 Laboratory setup for coupling efficiency measurements

In this section we will describe the laboratory setup used to characterize our grating coupler prototypes. To make it easier for the reader to understand how everything is connected we have included a flowchart in [Figure 3.5](#) on page [54](#) that shows the main components and how different types of signals flow between them. An overview of the model names and manufacturers of the various components in our setup is also listed in [Table 3.6](#) on page [55](#).

Our laser kit is capable of producing wavelengths between approximately 1480 nm and 1620 nm [[65](#)], but this range is dependent on the input power provided by the laser diode driver. Tuning is achieved by adjustment of the cavity mirror using a motorized actuator, which is controlled from a computer using a compatible motor controller. To avoid overheating, a temperature controller is also connected to the kit.

The laser output is initially unpolarized, and is therefore sent through a polarizer to ensure that only the TE-polarized components remain. The laser light then continues propagating along a single-mode optical fiber until it reaches the lensed fiber endpoint, which is directed towards a sample stage. The angle of the fiber is adjustable, allowing different angles of incidence to be tested during characterization procedures.

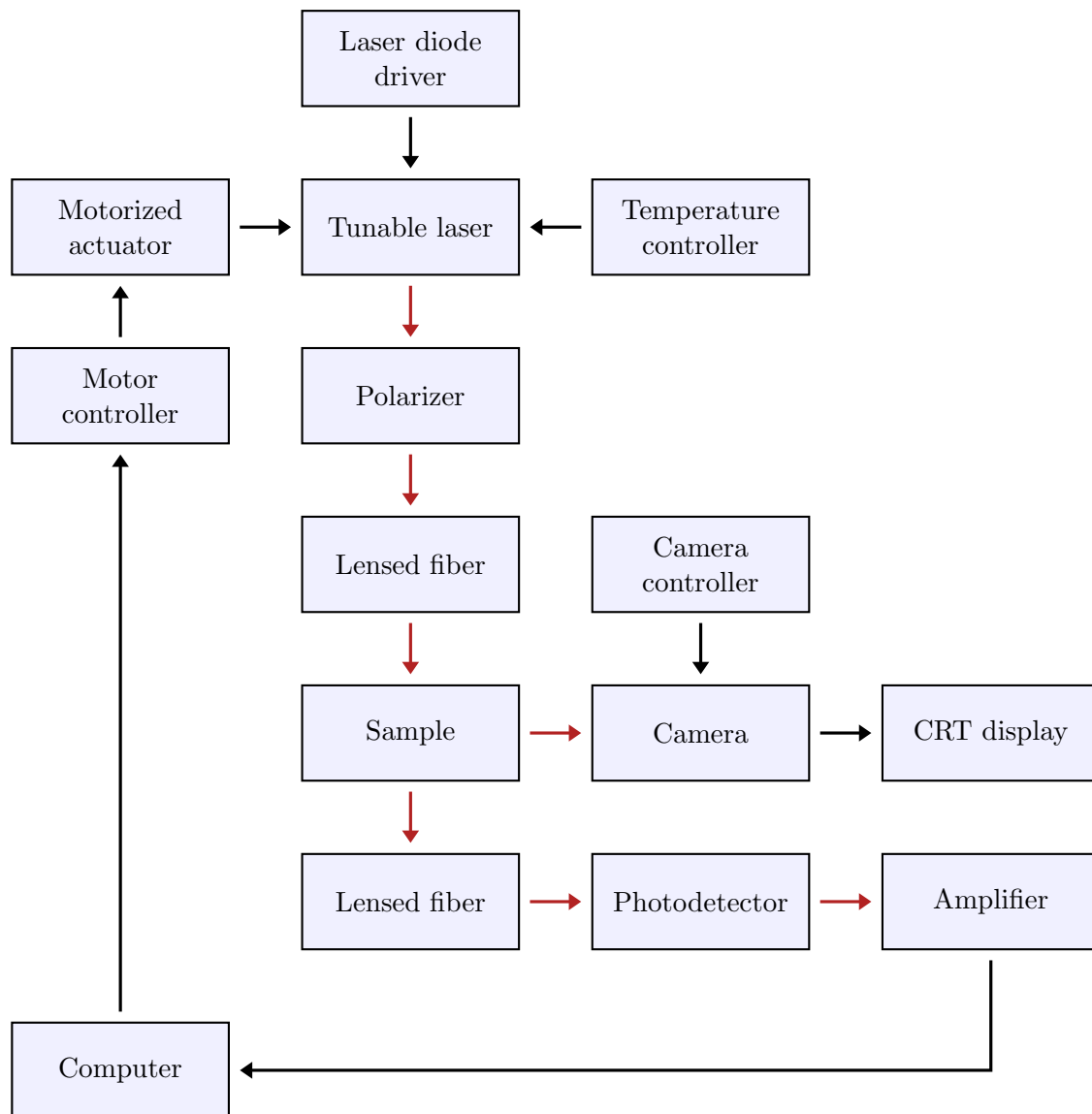
A second lensed fiber tip is directed towards the sample as well, and can be positioned to coincide with any out-coupled beams originating from the sample. The angle of this fiber can also be adjusted, to ensure similar conditions for both in-coupling and out-coupling. It might seem counterintuitive to use a lensed fiber to catch the output beam, but this is necessary to ensure similar fiber-to-waveguide and waveguide-to-fiber coupling efficiencies – as governed by the reciprocity theorem discussed in section [2.3.4](#).

The fraction of the output beam that is successfully coupled into the second fiber is guided through a photodetector and an amplifier to enhance the signal quality and convert light to electric signals. It is then input to a computer where the signal strength is plotted against the wavelength of the laser source and the results are stored.

To facilitate alignment of the lensed fibers, an infrared camera is mounted on a laterally adjustable stage and directed towards the sample. The camera is driven by a camera controller, and is connected to a cathode-ray tube (CRT) display. The lensed fibers are also mounted on stages that can be adjusted both laterally and vertically, providing a simple way to align the lensed endpoints with the grating structures on our samples.

## 3.6 Characterization procedures

In this section we will discuss the procedures we have used to characterize fabricated samples. We will start by briefly explaining how we have inspected the quality of our samples both during and after the lithography process in section [3.6.1](#). Section [3.6.2](#) will cover imaging and analysis of the lines of our dose tests and in section [3.6.3](#) we will mention how we have structured our



**Figure 3.5:** Flowchart illustrating the laser setup we have used to characterize our grating couplers. Red arrows indicate flow of light, while black arrows indicate information flow by electrical signals. An overview of the components' model names and their manufacturers can be found in [Table 3.6](#) on page 55.

**Table 3.6:** Overview of the model names and manufacturers of the components used in our laser-based grating coupler optimization setup. A flowchart illustrating how the different components are interconnected can be found in [Figure 3.5](#) on page 54.

Component	Model	Manufacturer
Amplifier	PDA200C	Thorlabs
Camera	–	Hamamatsu
Camera controller	C2400	Hamamatsu
CRT display	–	Hitachi
Laser diode driver	505	Newport
Motor controller	TDC001	Thorlabs
Motorized actuator	Z812	Thorlabs
Optical fibers	SMF-28 Ultra	Corning
Photodetector	DET10C2	Thorlabs
Polarizer	FPC560	Thorlabs
Lensed fiber	TSMJ-X-1550-9/125-0.25-7-2.5-14-2	OZ Optics
Temperature controller	325	Newport
Tunable laser kit	TLK-L1550M	Thorlabs

coupling efficiency measurements.

### 3.6.1 Resist and sample quality

Many of the steps in the lithography process are very sensitive to contamination, which accumulates over time – even in a cleanroom environment. It is therefore in general not a good idea to perform a lot of time-consuming characterization procedures during the lithography process, unless they can be done in a vacuum chamber. We have therefore tried to restrict optical inspections to a minimum, but have not been able to eliminate the need for these inspections completely.

The application of resist is very prone to defects, and all samples were therefore subject to a quick optical inspection using a simple magnifying glass after soft baking. If incomplete coverage, holes or significant protruding defects were observed, the sample in question was stripped for resist and recoated.

More thorough inspections were performed after samples were fully processed and all resist had been removed by plasma cleaning. Optical microscopy was used to look for bigger defects, and SEM imaging was used to measure grating and waveguide dimensions, as well as to look for resist residues on top of our silicon structures. If residues were observed, samples were subject to an additional plasma cleaning step.

### 3.6.2 Dose tests

As described in section 3.4.5.1, our dose test design consisted of lines of various thicknesses that were subject to different area doses during exposure. Even though we are limited to a  $150 \mu\text{C cm}^{-2}$  dose for compatibility reasons, we wanted to see how well the width of the fabricated structures corresponded with the width of the lines in our design files. This should give us an indication

of how much the dimensions in our design files should be adjusted to account for any discrepancies.

All lines were therefore imaged using an SEM at a constant zoom level. To minimize noise, each image was taken as an average of 8 individual image frames, where the SEM software accounted for any drift effects. MATLAB was then used to analyze each image by comparing the individual pixel values and measuring the width of the lines based on a contrast threshold. To ensure that defects and slight variations in line thicknesses did not affect the result significantly, each width was calculated as an average over each horizontal line of pixels in the image. The MATLAB code used for this image analysis is provided in appendix B.1 on page 93.

After line thickness measurements, dose test samples were also scribed perpendicular to the lines in the design and their cross-section was imaged using an SEM. This was done to check that our samples did not feature very slanted sidewall profiles, which could affect coupling efficiency significantly. The sidewall inclination was only inspected qualitatively by visual inspection of the SEM images, and no quantitative analysis was conducted.

### 3.6.3 Coupling efficiency

All fabricated grating coupler prototypes that were not found to have significant defects during the inspections discussed in section 3.6.1, were tested extensively in the laser-based laboratory setup described in section 3.5.3.

Our samples included arrays of grating couplers with slightly different dimensions, as mentioned in section 3.4.5.2. All of these couplers were tested individually by iterative adjustments of the position of the lensed input and output fibers. Alignment was made easier by the lateral adjustment knobs on the fiber mounts, but it was nevertheless difficult to ensure optimal alignment every time.

The coupling efficiency of many different grating couplers was tested by sweeping over different wavelengths and incidence angles. Angular adjustments of the fibers were not automated, and a limited set of angles were therefore tested in the vicinity of  $16^\circ$ , which was the angle our structures had been optimized for in the project thesis simulations [1]. The measured output intensity was compared to the intensity of the laser source after it had passed through the polarizer, and the coupling efficiency per grating coupler could then be calculated as the square root of the coupling efficiency of the whole structure. This metric does not include any other sources of losses, which we will discuss further in section 4.2.3.

## Chapter 4

# Results and discussion

This chapter will be devoted to the presentation of the results we have found in this thesis, as well as a detailed discussion of their validity and significance. We will start by examining our simulation results in section 4.1 before we move on to discuss results from our fabrication and characterization procedures in section 4.2. Simulation and fabrication results will then be compared in section 4.3 to assess similarities and differences between them.

### 4.1 Simulation results

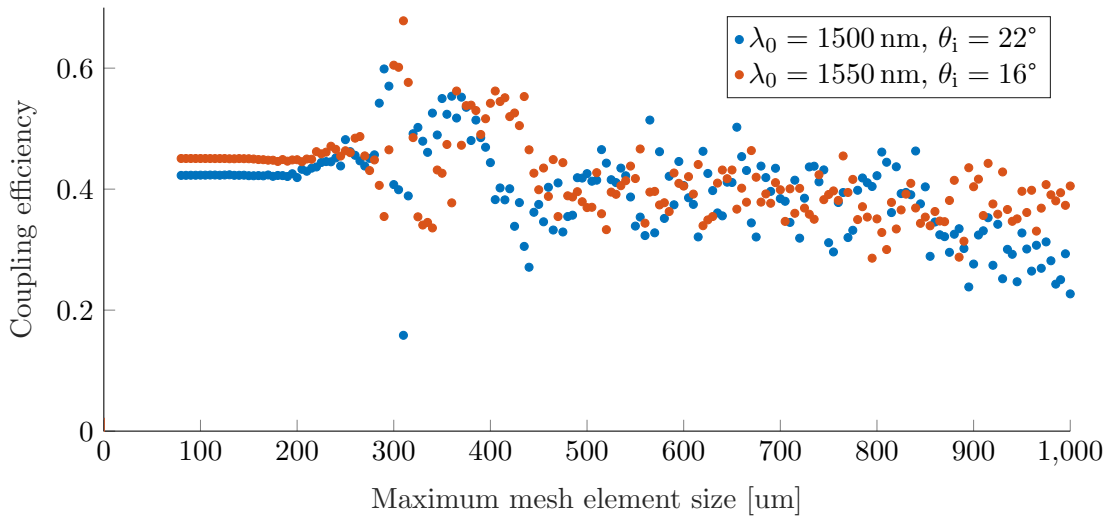
#### 4.1.1 Meshing

Over the course of this project, meshing parameters have been optimized and verified several times to account for geometry and wavelength changes. As mentioned in section 3.2.1, the accuracy of the finite-element method is highly dependent on the maximum mesh element size, and we have therefore run sweeps over this parameter to examine its affect on our solution stability. The results from two of these sweeps can be seen in [Figure 4.1](#) on page 58.

From this figure it is clear that the coupling efficiency varies significantly for large maximum mesh element sizes, despite all other simulation parameters being held constant. This indicates that the mesh is not sufficiently detailed for the finite-element method to produce accurate results.

Both of the plots flatten and become less erratic once the maximum mesh element sizes fall below a certain threshold. The location of this threshold varies slightly, due to different incident angles and wavelengths used. The stable region is located below  $\approx 170$  nm for the model with a 1550 nm wavelength and a  $16^\circ$  incidence angle, and below  $\approx 160$  nm for the 1500 nm wavelength and  $22^\circ$  incidence angle case.

To be on the safe side, we have chosen a value of 130 nm for the maximum mesh element size for all simulations throughout this thesis. Similar mesh stability checks have been conducted for both uniform and apodized grating models, and this value has been found to be sufficient for all wavelengths and geometries used in this thesis. With this configuration, our mesh should therefore be sufficiently detailed to ensure that the finite-element method yields valid results within the bounds of the simplifications we have made in our 2D model.



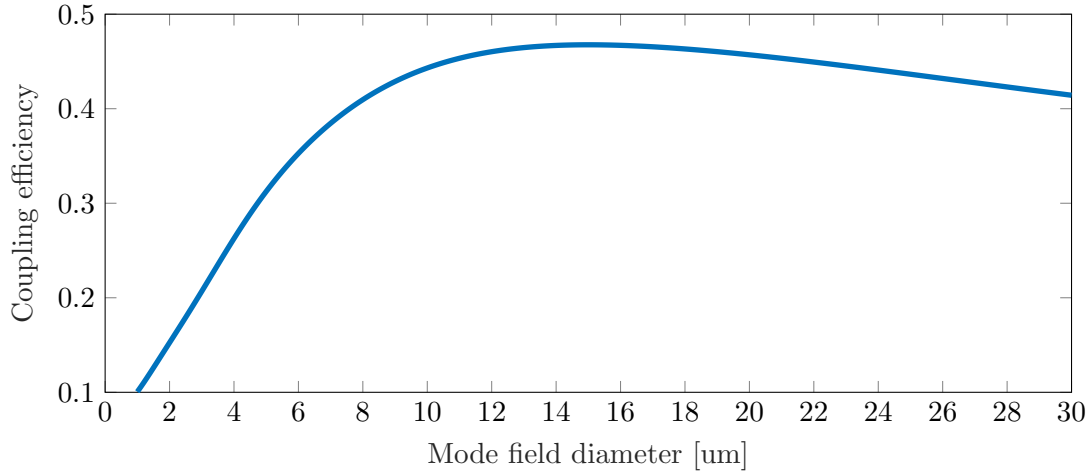
**Figure 4.1:** Scatter plot showing the relation between the maximum mesh element size and the coupling efficiency for two samples at different wavelengths and incidence angles. Convergence of the solution can be seen for small mesh element sizes, where the plots flatten. Each dot represents a single simulation run, and all simulations were conducted using the uniform grating coupler model with grating dimensions  $w_{\text{Si}} = 580 \text{ nm}$  and  $w_{\text{air}} = 110 \text{ nm}$ , number of gratings  $n_{\Lambda} = 40$ , vertical fiber offset  $\Delta y_{\text{fiber}} = 3 \mu\text{m}$  and horizontal fiber offset  $\Delta z_{\text{fiber}} = -8.65 \mu\text{m}$ . The waveguide and cladding thicknesses were  $220 \text{ nm}$  and  $1 \mu\text{m}$ , respectively. The wavelengths and incidence angles used for the two data series are listed in the figure legend.

#### 4.1.2 Gaussian beam diameter

In section 3.2.2 we briefly discussed how the beam diameter of the beam originating from the lensed fiber tips that we used in our characterization setup deviates significantly from the mode-field diameter we have used to model the Gaussian source in our simulations. A parametric sweep was therefore run to make it easier to compare the coupling efficiency of simulated and fabricated structures. The result of this sweep can be seen in Figure 4.2 on page 59.

We see from the figure that the coupling efficiency is significantly lower for small mode-field diameters, contrary to our initial assumption. If we compare the coupling efficiency for the mode-field diameter used in our simulations ( $10.4 \mu\text{m}$ ) to that of the beam diameter at the focus point of the lensed fiber tips ( $\approx 2.5 \mu\text{m}$ ), we see that the coupling efficiency is reduced by approximately 60%. Any coupling efficiencies that we find for our fabricated grating coupler prototypes could therefore potentially be  $0.4^{-1} \approx 2.5$  times higher than measured if a non-lensed fiber is used instead.

Now, a Gaussian beam focused by simple lenses, such as our lensed fiber tips, will become gradually narrower until it reaches the focus point where the beam diameter is at its smallest. The beam will then broaden as it propagates beyond this point. The results in Figure 4.2 could therefore be difficult to relate to the coupling efficiency measured for our grating coupler prototypes, unless the distance between the lensed fibers and our samples can be adjusted very accurately. We will discuss this further in section 4.3 after we have presented our results from the fabrication and characterization procedures.



**Figure 4.2:** Plot of the coupling efficiency as a function of the mode field diameter of the Gaussian fiber source in our simulations. Simulations were conducted using the uniform grating coupler model with grating dimensions  $w_{\text{Si}} = 580$  nm and  $w_{\text{air}} = 110$  nm, number of gratings  $n_{\Lambda} = 40$ , vertical fiber offset  $\Delta y_{\text{fiber}} = 3$   $\mu\text{m}$  and horizontal fiber offset  $\Delta z_{\text{fiber}} = -8.65$   $\mu\text{m}$ . The waveguide and cladding thicknesses were 220 nm and 1  $\mu\text{m}$ , respectively. The wavelengths and incidence angles were 1550 nm and  $16^\circ$ , respectively.

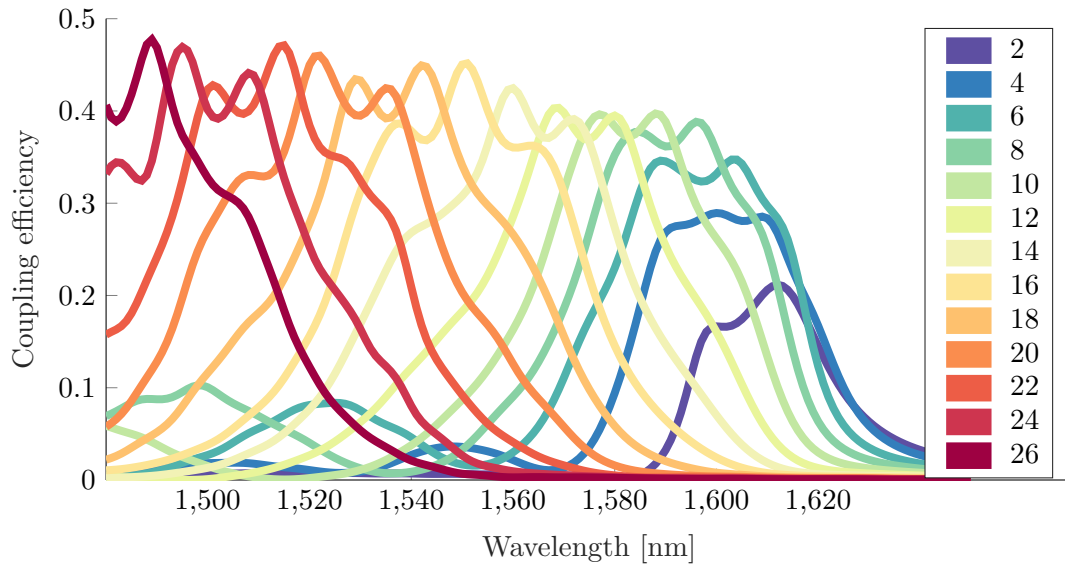
### 4.1.3 Uniform grating coupler

#### 4.1.3.1 Wavelength and incidence angle

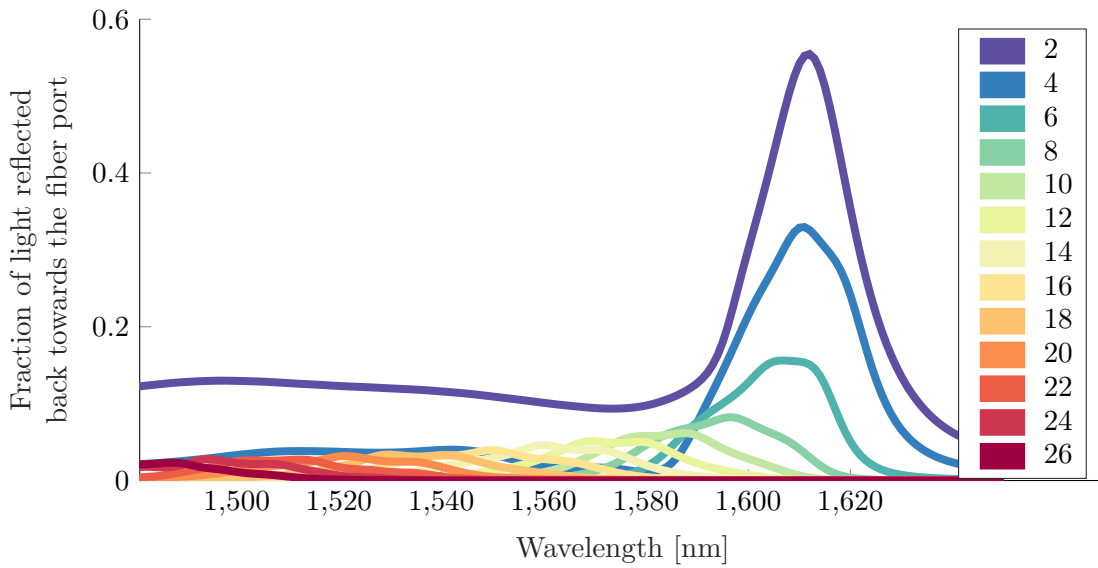
To examine the dependency of the coupling efficiency on the wavelength and the incidence angle of our fiber source, parametric sweeps were conducted over many different combinations of these parameters. Wavelengths between 1480 nm and 1650 nm and incidence angles between  $2^\circ$  and  $22^\circ$  were examined, and the results can be seen in [Figure 4.3a](#) on page 60.

The results show that the maximum coupling efficiency for this grating structure remains quite high across a wide range of wavelengths, as long as the incidence angle is adjusted accordingly. If our fabricated devices have higher coupling efficiencies for different wavelengths than the 1550 nm wavelength we are aiming for, we can therefore likely adjust the incidence angle to shift their peak towards 1550 nm. Since there are no compatibility requirements that restrict our choice of incidence angle, this could potentially make it easier to optimize our fabrication procedures.

We note from the figure that the maximum coupling efficiency is significantly reduced for incidence angles below  $8^\circ$ . This makes sense since light rays impacting our structures at near-normal incidence would not interact with the sidewalls of our grating structure to any significant degree. The rays would mostly be reflected back in the opposite direction or transverse the silicon-silica or air-silica interfaces and continue propagating within the silica and/or the silicon substrate. We have included a plot of the fraction of light that is reflected back towards the fiber port in [Figure 4.3b](#). Comparing this figure to [Figure 4.3a](#) we clearly see that reflection is indeed the likely culprit for the reduced coupling efficiency at small incidence angles.



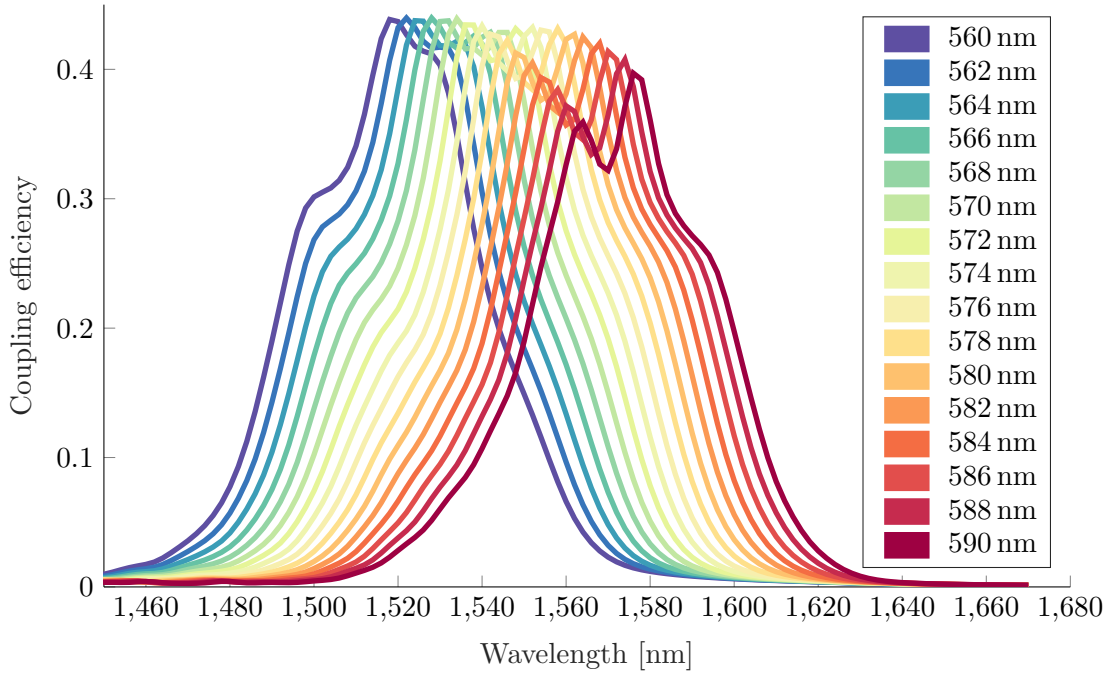
(a) Coupling efficiency as a function of wavelength and incidence angle.



(b) Fraction of light reflected back towards the fiber port as a function of wavelength and incidence angle.

**Figure 4.3:** Plots of the coupling efficiency and the fraction of reflected light as functions of the wavelength and incidence angle. Simulations were conducted using the uniform grating coupler model with grating dimensions  $w_{\text{Si}} = 580 \text{ nm}$  and  $w_{\text{air}} = 110 \text{ nm}$ , number of gratings  $n_{\Lambda} = 40$ , vertical fiber offset  $\Delta y_{\text{fiber}} = 3 \mu\text{m}$  and horizontal fiber offset  $\Delta z_{\text{fiber}} = -8.65 \mu\text{m}$ . The waveguide and cladding thicknesses were  $220 \text{ nm}$  and  $1 \mu\text{m}$ , respectively.





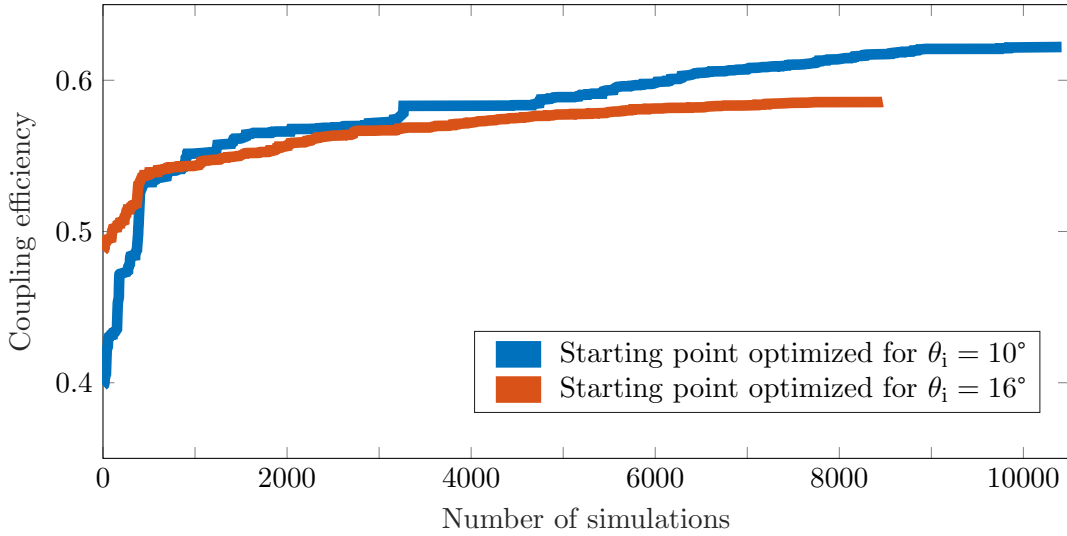
**Figure 4.4:** Plot of the coupling efficiency as a function of the wavelength and grating dimensions. The total grating period is held constant at 690 nm for all simulations and colors are used to represent different values of the silicon grating width  $w_{\text{Si}}$ . Simulations were conducted using the uniform grating coupler model with a number of gratings  $n_{\Lambda} = 40$ , incidence angle  $\theta_i = 15^\circ$ , vertical fiber offset  $\Delta y_{\text{fiber}} = 3 \mu\text{m}$  and horizontal fiber offset  $\Delta z_{\text{fiber}} = -8.65 \mu\text{m}$ . The waveguide and cladding thicknesses were 220 nm and 1  $\mu\text{m}$ , respectively.

A  $10^\circ$  incidence angle is often used for grating couplers in literature [21, 66, 67]. According to [67] this angle is chosen because it is sufficient to avoid reflections, which seems to agree nicely with our simulation results.

#### 4.1.3.2 Wavelength and grating dimensions

In addition to examining the wavelength and incidence angle, we have also looked at how the grating dimensions affect our coupling results. Parametric sweeps have been conducted over different grating dimensions and wavelengths, and this has been repeated for  $15^\circ$ ,  $18^\circ$  and  $21^\circ$  incidence angles as well. The results for the  $15^\circ$  case can be seen in Figure 4.4. The results for  $18^\circ$  and  $21^\circ$  incidence angles were similar, but were shifted to different wavelengths due to the change in incidence angle (see section 4.1.3.1).

We see that the maximum coupling efficiency does vary a bit for different grating dimensions, but the relative difference is only about 10 % for the  $w_{\text{Si}} = 560 \text{ nm}$  and  $w_{\text{Si}} = 590 \text{ nm}$  cases. The gradual reduction in the height of the peaks for increased silicon grating widths does seem to indicate that there is a limit to how wide the silicon gratings should be in our design. The highest coupling efficiency we found was for  $w_{\text{Si}} = 566 \text{ nm}$  at a 1528 nm wavelength. Parametric sweeps over a much broader range of values for  $w_{\text{Si}}$  would have to be conducted to determine if better coupling efficiencies can be achieved for



**Figure 4.5:** Plot showing the gradual increase in coupling efficiency that we found throughout our optimization processes for two apodized grating couplers. The starting points of the optimization processes were mainly uniform grating couplers that were optimized for  $10^\circ$  and  $16^\circ$  incidence angles in the project thesis [1]. These angles were used as starting points in these optimizations as well, and are used to identify the two data series in the figure legend. A detailed description of the model parameters used for the two starting points can be found in section 3.2.4.

different grating dimensions, but this would also bring us quite far from our desired 1550 nm wavelength. We have therefore not examined this further in this thesis.

A very interesting thing to note from Figure 4.4 is that the grating dimensions cause a wavelength shift for the coupling efficiency peaks, similar to the effect of changing the incidence angle that we found in section 4.1.3.1. When optimizing fabrication procedures and our grating coupler prototypes we should therefore be able to use both of these parameters to shift the supported wavelengths of our devices to the desired range around 1550 nm.

#### 4.1.4 Apodized grating coupler

The approach we have used to design and optimize our apodized grating structures was covered in detail in section 3.2.4. More than 8000 simulations were run for each of the two starting points and a plot of the gradual increase in coupling efficiency that occurred throughout these simulations is provided in Figure 4.5.

Both of the data series in Figure 4.5 feature rapid improvements of the coupling efficiency during the first 500 simulations, and then slower and more gradual increases throughout the rest of the optimization process. A single sweep over all the parameters consists of 880 simulations, and it does seem reasonable that the improvements would be biggest in the beginning when all parameters can be adjusted to more optimal values than the uniform widths and separations used for the starting points.

The gradual improvements seen after the first 880 simulations is likely caused by the optimal values for some parameters being outside the initial  $\pm 10\Delta$  range that was checked for each parameter. It is also likely that changes to some parameter values will cause the optimal value for other parameters to change, which would also contribute to this gradual improvement over time. The value of  $\Delta$  was set to 2 nm for all grating widths, grating separations and horizontal displacements of the grating structure. For the incidence angle sweeps, a value of  $\Delta = 0.1^\circ$  was used.

The best coupling efficiencies found were 58.9% for the apodized structure where the starting point was optimized for a  $16^\circ$  incidence angle and 62.2% for the apodized structure where the starting point was optimized for a  $10^\circ$  incidence angle. One might initially think that it would be natural for the two optimization processes to converge towards a single, optimal solution, but it is unfortunately not that simple.

To explain why this is, let us consider a landscape with different mountains, hills and valleys. Say that we want to optimize our altitude in this landscape in a similar manner to the optimization procedures we have used in this thesis. We start at some arbitrary location and sample the altitude at this location and at 10 different locations along the north-south axis. We then move to the location with the highest altitude and repeat the same procedure for the east-west axis afterwards. We then repeat the whole process over and over again. Depending on where we sample from, and the distance between each of the 10 locations sampled, we might not hit the tallest mountain in the area at all, but rather end up on the top of some hill at a lower altitude.

Now, the optimization procedure we have used is dependent on much more than two variables. We end up with a 43-dimensional coupling efficiency “landscape” where it is extremely unlikely that we will find the tallest “mountain”. We will find a local maximum, analogous to the “hill” above, but it is unlikely that this is the location with the highest coupling efficiency in the entire 43-dimensional landscape. It is also unlikely that two starting points, analogous to two people at different locations, will end up on the same “hill” when performing the same optimization procedure.

Because of this, we cannot in any way conclude that we have found the best possible apodized grating structure within the bounds of the parameters we have defined. It is even possible that the results we have found could be further improved by continuing the same optimization process. The process was halted when the relative improvement was small over a high number of simulations, but it is definitely possible that this was not the real endpoint of the process.

To find the endpoint of our optimizations, we would have to continue running simulations until we could iterate over all parameters without finding any improved coupling efficiencies. This would not indicate that we had found the best result in our coupling efficiency landscape, but it would constitute an endpoint for our optimizations for the particular starting point used.

In addition to choosing different starting points, the results of our optimization process would likely be changed significantly by changing the value of  $\Delta$ . It is very difficult to say what the best value for this parameter is, but it could

**Table 4.1:** Overview of the parameter values for the apodized grating structure with a 62.2% coupling efficiency that was found using the optimization procedure presented in section 3.2.4. The starting point used to find this result was the uniform grating structure optimized for a 10° incidence angle in [1].

Parameter	Value(s)
Width of air gratings (from left to right) [nm]	206 114 126 108 84 94 120 154 108 84 88 88 104 102 108 104 94 92 84 66 62
Grating separations (from left to right) [nm]	561 553 550 559 564 554 564 564 555 565 563 553 548 564 575 556 562 569 584 590
Horizontal displacement of the grating structure [nm]	-8769
Incidence angle [°]	9.7

potentially be a good idea to start out with a quite high value for  $\Delta$  and then gradually reduce it as the optimization progressed. This could make it easier to find any “plateaus” in the coupling efficiency landscape with higher coupling efficiencies on average.

What we can conclude from our results is that it is possible to find an apodized grating structure with at least a 62.2% coupling efficiency, which is comparable to results found in literature [19–21, 68]. This is of course only a theoretical result, limited by the accuracy of our model. Whether or not such a design would work in manufactured devices can only be fully established through fabrication and testing of manufactured devices.

The parameter combination used for the apodized grating structure with a 62.2% coupling efficiency is provided in Table 4.1. We will not discuss these parameter values in detail, but it is interesting to note that the widths of the rightmost gratings are gradually decreasing towards the right. The starting point for the optimization leading to this solution did not feature an endslot that was narrower than the rest of the gratings, but the optimization process has nevertheless resulted in such a configuration. This is a strong indication that the hypothesis put forth in the project thesis [1] has some merit, and that it is indeed beneficial to have a more gradual effective refractive index change in the transition between grating structure and waveguide.

Several improvements can be made to the optimization algorithm we have used in this thesis. We have already mentioned how the  $\Delta$  parameter could be gradually reduced to find higher efficiency results, but other approaches exist as well. The use of semi-randomized  $\Delta$ -values could for example allow our algorithm to sporadically look for high-efficiency results beyond the  $\pm 10\Delta$  restraint that we have initially imposed on it. Our algorithm could also be made to have significantly faster solution convergence on computer systems with multiple processing cores or that support hyperthreading if support for parallel processing was to be included.

## 4.2 Fabrication results

### 4.2.1 Resist and sample quality

Inspections of the resist quality were conducted using a simple magnifying glass, as mentioned in section 3.6.1, and high-resolution images of the resist are therefore not included here. Approximately half of the samples that were coated with resist featured one or multiple defects and were therefore stripped of resist, cleaned and recoated. The other half of the samples featured either no defects or had only minor defects in areas of the sample that were not to be patterned and exposed, and were therefore used in subsequent processing.

### 4.2.2 Dose tests

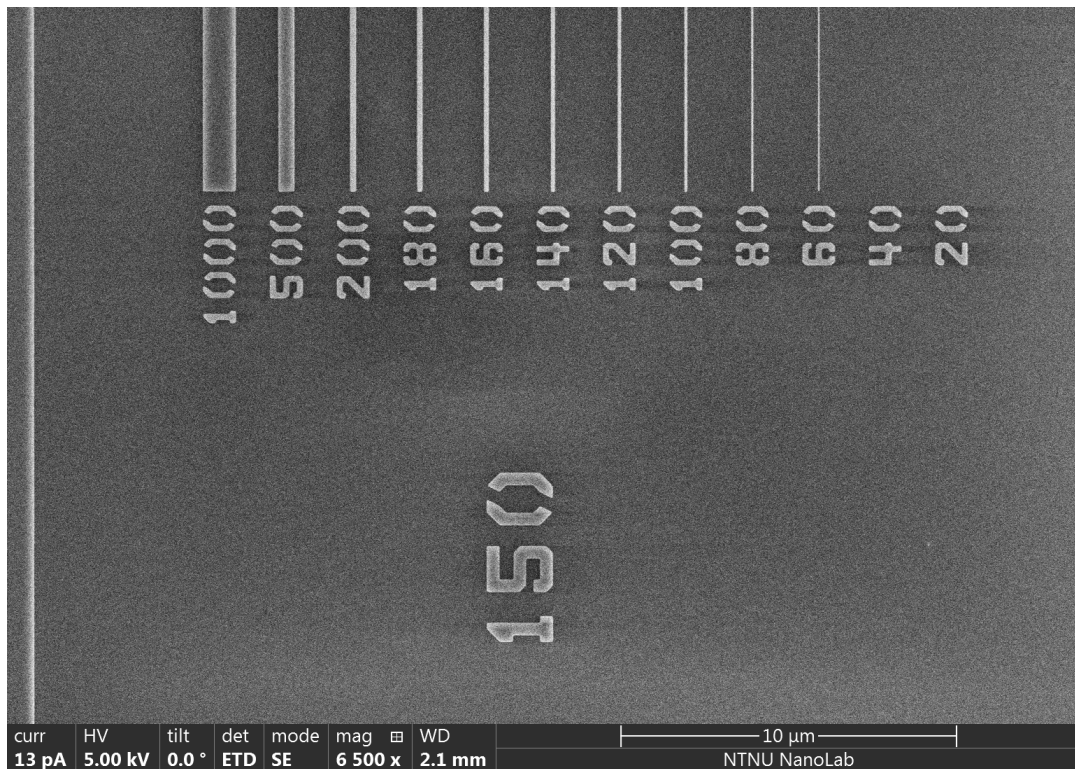
Our fabrication procedure has been restricted to a  $150 \mu\text{C cm}^{-2}$  EBL exposure dose for compatibility reasons, but dose tests have nevertheless been conducted to independently verify if this is a reasonable parameter value. The design and area doses used for these tests were described in detail in section 3.4.5.1 and will not be repeated here.

To ensure that we have sufficient data to analyze the line widths properly, individual SEM images were taken of all lines for all doses. The majority featured very uniform widths, but some of the thinnest lines were of poor quality or completely missing, especially for high area doses. Images were therefore also taken to get an overview of the quality of our lines for different exposure doses. An example of such an image is provided in Figure 4.6 on page 66.

From this figure we can clearly see that the 20 nm and 40 nm lines are missing, while the rest of the lines seem to be successfully manufactured and feature quite uniform widths. The rest of our SEM images show that the 40 nm line is missing for all area doses that are higher than  $140 \mu\text{C cm}^{-2}$ . For area doses between  $125 \mu\text{C cm}^{-2}$  and  $140 \mu\text{C cm}^{-2}$  the line is present, but is of poor quality. Only at the lowest dose tested,  $120 \mu\text{C cm}^{-2}$ , is the 40 nm line fairly uniform and of good quality.

A summary of the quality of the different lines manufactured with different area doses can be seen in Table 4.2 on page 67. Green circles are here used to represent lines of good quality, orange circles are used for lines of poor quality and red circles indicate lines that are completely missing for the given dose. Note that the analysis of the SEM images is based on a qualitative visual inspection and that only 6 to 7  $\mu\text{m}$  of the 5 mm long lines have been examined. The results presented here are therefore not necessarily representative for all sections of the lines, but should give an indication of the overall relation between line quality and the area dose.

We can see from Table 4.2 that higher doses seem to result in lower line quality for the thinnest lines manufactured. This makes sense, since higher doses will result in more proximity effects during exposure – which effectively increases the area of the exposed regions and reduces the area of the unexposed regions. Since the lines in our design are unexposed and unetched areas, higher area doses would result in reduced line thicknesses. It does not seem unreasonable



**Figure 4.6:** SEM image showing the endpoints and labels of some of the lines present on our dose test sample. The silica cladding is shown as dark regions and silicon structures are shown as bright regions. The big label that reads “150” indicates that these lines were exposed using an area dose of  $150 \mu\text{C cm}^{-2}$ , while the smaller labels that are located closer to the lines indicate the line widths in nanometers that were specified for the respective lines in the design files. We see that the 40 nm and 20 nm lines are completely missing from the sample. The image was taken at a magnification of 6500 times.

**Table 4.2:** Summary of the line quality on the sample used for our dose tests. Green circles indicate lines with uniform widths and good overall quality, orange circles denote lines of poor quality and uniformity and red circles are used for lines that were completely missing for the given dose. The results presented in this table are based on a qualitative visual inspection of SEM images, and are therefore not necessarily representative for all sections of the manufactured lines.

Area dose [ $\mu\text{C cm}^{-2}$ ]	Width of line in design file [nm]											
	20	40	60	80	100	120	140	160	180	200	500	1000
120	●	●	●	●	●	●	●	●	●	●	●	●
125	●	●	●	●	●	●	●	●	●	●	●	●
130	●	●	●	●	●	●	●	●	●	●	●	●
135	●	●	●	●	●	●	●	●	●	●	●	●
140	●	●	●	●	●	●	●	●	●	●	●	●
145	●	●	●	●	●	●	●	●	●	●	●	●
150	●	●	●	●	●	●	●	●	●	●	●	●
155	●	●	●	●	●	●	●	●	●	●	●	●
160	●	●	●	●	●	●	●	●	●	●	●	●
165	●	●	●	●	●	●	●	●	●	●	●	●
170	●	●	●	●	●	●	●	●	●	●	●	●
175	●	●	●	●	●	●	●	●	●	●	●	●
180	●	●	●	●	●	●	●	●	●	●	●	●

that making the thinnest lines even thinner could cause them to become so fragile that they are damaged during the development procedure.

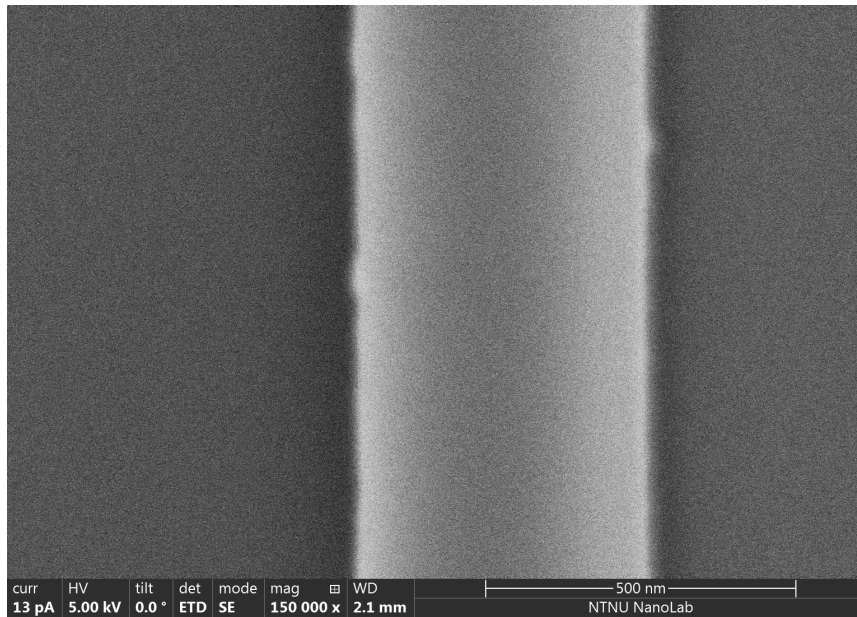
Let us consider the results for the  $150 \mu\text{C cm}^{-2}$  area dose that we will be using for our fabrication procedures. As mentioned previously, the 20 nm and 40 nm lines were completely missing for this area dose. The 60 nm line seemed to be of good quality, but since the quality of the same line was poor for both  $145 \mu\text{C cm}^{-2}$  and  $155 \mu\text{C cm}^{-2}$  area doses it is also unlikely that the entire line is of good quality for the  $150 \mu\text{C cm}^{-2}$  case.

The 80 nm line and all thicker lines seem to be of good quality for the entire range of area doses tested, and it is therefore likely that this is also true for the entire line at a  $150 \mu\text{C cm}^{-2}$  area dose. Great care should be taken when attempting to make structures with critical dimensions that are smaller than 80 nm using our fabrication procedure and a  $150 \mu\text{C cm}^{-2}$  area dose.

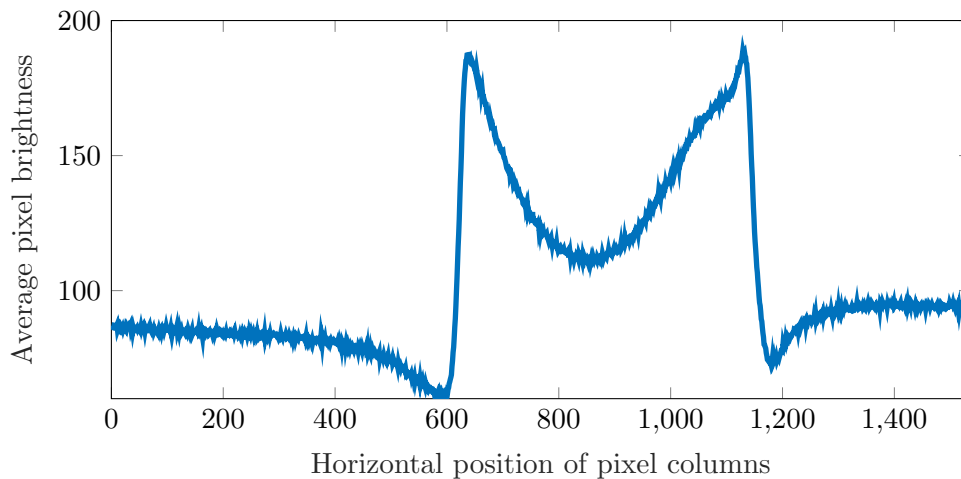
Now, the results we have presented thus far have only been qualitative and cannot be used to accurately determine the widths of the lines in our dose test. Image analysis techniques have therefore been used to analyze 108 SEM images of the individual silicon lines. This characterization procedure was described in section 3.6.2 and the MATLAB-script used for the image analysis is available in appendix B.1. All images were taken at a 150,000 times magnification, and an example of one such image can be seen in Figure 4.7 on page 68.

The resolution of our SEM images are quite good, but it is still difficult to determine within a few nanometers exactly where the edges of the lines are located – especially based on visual estimates. The brightness values for all





**Figure 4.7:** SEM image of a fraction of the 500  $\mu\text{m}$  thick line in [Figure 4.6](#) at a higher magnification. The silica cladding is shown as dark regions and silicon structures are shown as bright regions. The line is part of a dose test and was made using a  $150 \mu\text{C cm}^{-2}$  EBL area dose. The image was taken at a magnification of 150,000 times.



**Figure 4.8:** Plot of the average brightness of each column of pixels in [Figure 4.7](#). The analyzed SEM image uses a 8 bit grayscale color model, and the pixel brightness values therefore range from 0 (white) to 255 (black). The horizontal position of the pixel columns in the image is denoted on the horizontal axis, and the figure is aligned with [Figure 4.7](#) to make it easier to compare this plot with the SEM image.



pixels in the images were therefore imported to MATLAB and average values were calculated for all columns of pixels in the images. A plot of the resulting data for the image in [Figure 4.7](#) is provided in [Figure 4.8](#). The two figures are placed on the same page and are aligned with each other to make it easier for the reader to relate the horizontal positions of the pixel columns in [Figure 4.8](#) to the SEM image in [Figure 4.7](#).

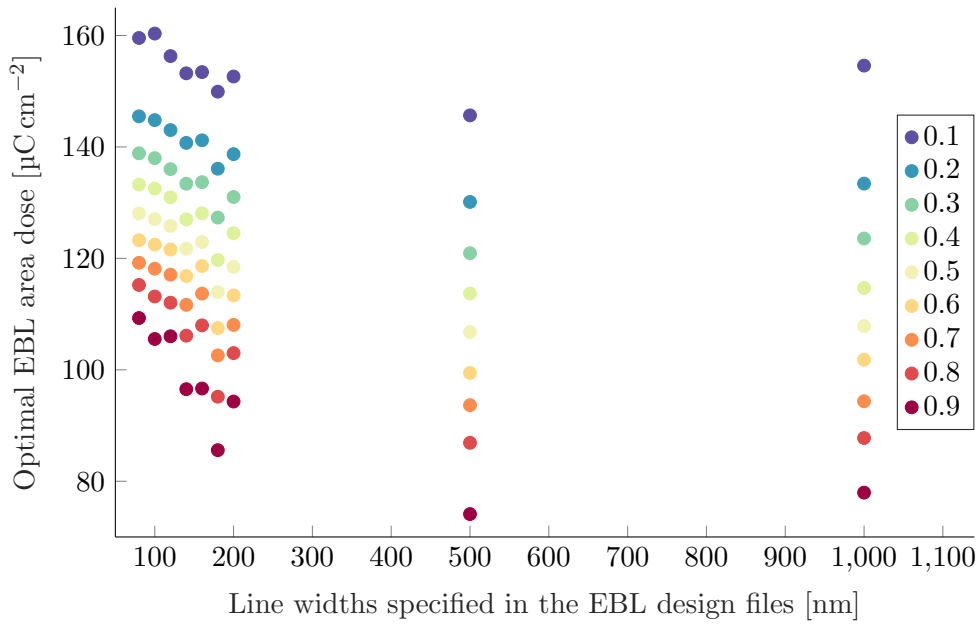
The edges of the silicon line is easily identifiable from [Figure 4.8](#) as two abrupt changes in the pixel brightness. However, the transitions between darker and brighter pixels at the edge of the silicon line are not perfectly vertical, and to determine the width of the silicon line we must therefore decide which pixel brightness value we want to use as a threshold when measuring the distance between the two near-vertical lines in the plot.

To examine this further, we considered how different choices for this threshold value would affect the calculation of an optimal area dose. In the following discussion, we will use the value 1 to refer to the average brightness value of the two peaks in [Figure 4.8](#), and similarly the value 0 to refer to the average brightness value of the bottommost points of the valleys that are directly adjacent to the transition regions on both sides of the silicon line in the plot. Widths of the silicon lines measured at a threshold value of 0.5 will therefore refer to a measurement across a horizontal line placed at the midpoint between peaks and valleys. Average values for the brightness of the peaks and valleys are used to minimize the effect of any sample tilt.

Now, the width of each silicon line in our dose test was calculated based on plots similar to that in [Figure 4.8](#) for nine different threshold values, ranging from 0.1 to 0.9. For each of these thresholds, and for each of the line widths specified in the design file, a linear regression analysis was run to find a relation between the measured width and the area dose used. From this, the optimal area dose was calculated for different combinations of threshold values and widths of the lines in the design files. The results are plotted in [Figure 4.9](#) on page 70. Each dot in this image shows the area dose that should be used for the silicon line to have the exact same width as the width specified in the design file.

From [Figure 4.9](#) we can see that the choice of threshold has a huge impact on which area doses are found to be optimal. Although it might seem logical to choose a threshold value of 0.5, it is not possible to determine if that is the most accurate choice without acquiring images of our structures with significantly higher resolutions and better focus. Such images would require better imaging instruments than the SEM model we have used in this thesis, and a definite conclusion on the optimal area dose can therefore not be provided here. What we can say is that an area dose of  $150 \mu\text{C cm}^{-2}$  is likely a bit too high, based on the fact that more than 90% of the dots in [Figure 4.9](#) have optimal area doses located below this value.

[Figure 4.9](#) also seems to show a trend where the optimal dose becomes lower and lower as the width of the lines increases. The only exceptions to this are the 1000 nm lines, which have almost the same optimal doses as the 80 nm lines. Now, as explained in section 3.3.6.4, scattering-induced widening of the electron beam can cause resist outside of the intended areas to be exposed during EBL



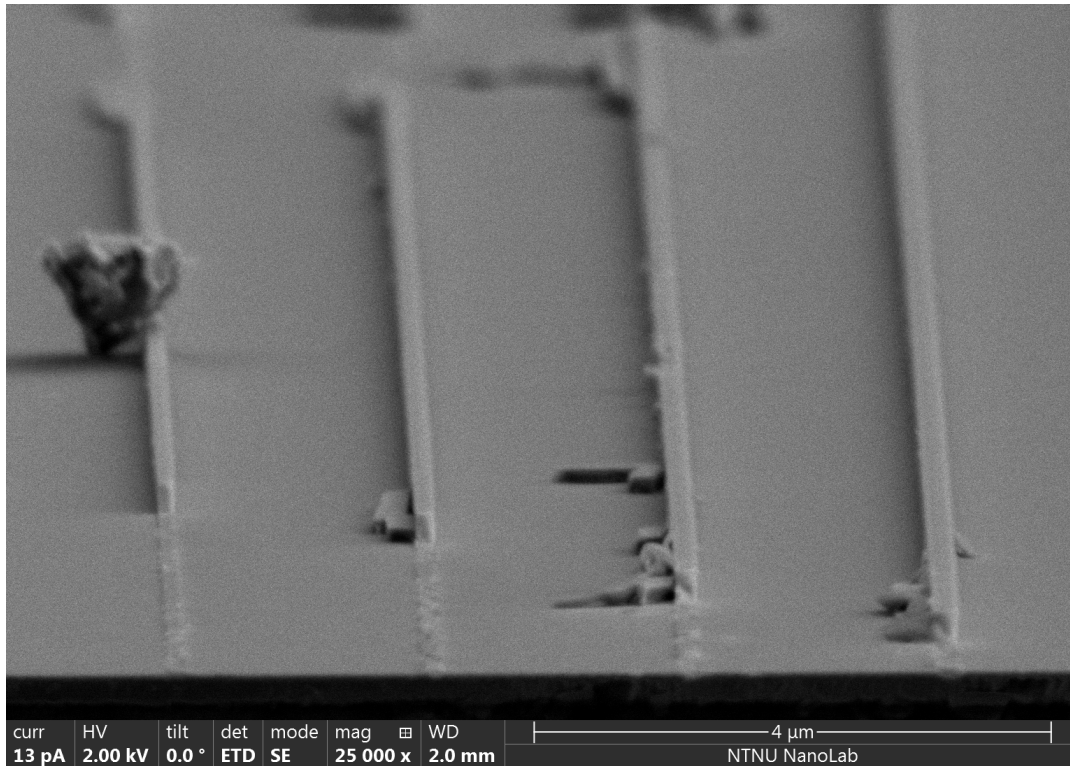
**Figure 4.9:** Plot of the optimal EBL area doses as a function of the line widths specified in the EBL design files and the brightness threshold value used when measuring the widths of each individual line from the SEM images. The “optimal area dose” here refers to the area dose that ensures that the measured line widths should be equal to the line widths specified in the design files. Colors are used to represent different threshold values, and the mapping between color and threshold value is provided in the figure legend.

processes. The penetration depth of this scattering should be fairly similar for all structures, which causes thinner lines to be more affected by proximity effects than their thicker counterparts.

The lines we have analyzed are parts of the unexposed regions, and it therefore makes sense for the optimal dose to be lower for *thinner* lines – which is the opposite of the trend observed in most of [Figure 4.9](#). This can however be explained by the PEC steps that were applied to the design files during the EBL preparations, which adjust the area doses in different regions of the design to counteract proximity effects. If the PEC was optimally configured, all dots with the same thresholds should have the same optimal area dose in [Figure 4.9](#). Since this is not the case, we can therefore conclude that the PEC procedure could be further optimized.

An important thing to note is that our grating structures feature both narrow silicon lines surrounded by etched regions and narrow etched lines surrounded by silicon regions. To fully examine the optimal area dose, tests should therefore also be conducted on etched lines of varying thicknesses surrounded by silicon. Due to time limitations this has unfortunately not been done during this master’s thesis, but it would be interesting to examine this in future work.

Before we wrap up this section on dose test results, we will briefly discuss the cross-sectional profiles of the silicon lines in our dose test. To ensure that the sidewalls of the silicon lines are not overly slanted, the dose test sample was scribed and its cross-section was imaged in the SEM as well. An image of



**Figure 4.10:** SEM image showing silicon lines made for our dose testing procedures. The image is taken from the side to enable visual inspection of the sidewalls, which appear to be very vertical. The lines were exposed using an area dose of  $150 \mu\text{C cm}^{-2}$ , and were defined to be 140 nm, 160 nm, 180 nm and 200 nm wide (from left to right) in the design files. The image was taken at a magnification of 25,000 times. Damaged lines, contamination and loose line fragments are a result of the scribing of the wafer.

four of the silicon lines exposed at an area dose of  $150 \mu\text{C cm}^{-2}$  is provided in [Figure 4.10](#).

From the figure we can see that the sidewalls of our structures are indeed very vertical. Similar observations were also made for structures that were fabricated using different area doses, and we can therefore conclude that slanted sidewall profiles is likely not a significant issue in our fabrication process. It should be noted, however, that this is based purely on a visual inspection and not numerical analyses.

### 4.2.3 Coupling efficiency

The procedures we have used to measure the output intensity of our fabricated grating coupler prototypes were briefly discussed in section 3.6.3 on page 56. In this section we will present the results of these measurements and explain how we have calculated coupling efficiencies from light intensities measured by the photodetector. We will consider some of the challenges we have encountered during the characterization procedures and assess the validity of our results.

To be able to say something about coupling efficiencies it was important to first characterize the laser source. Sweeps were therefore conducted where

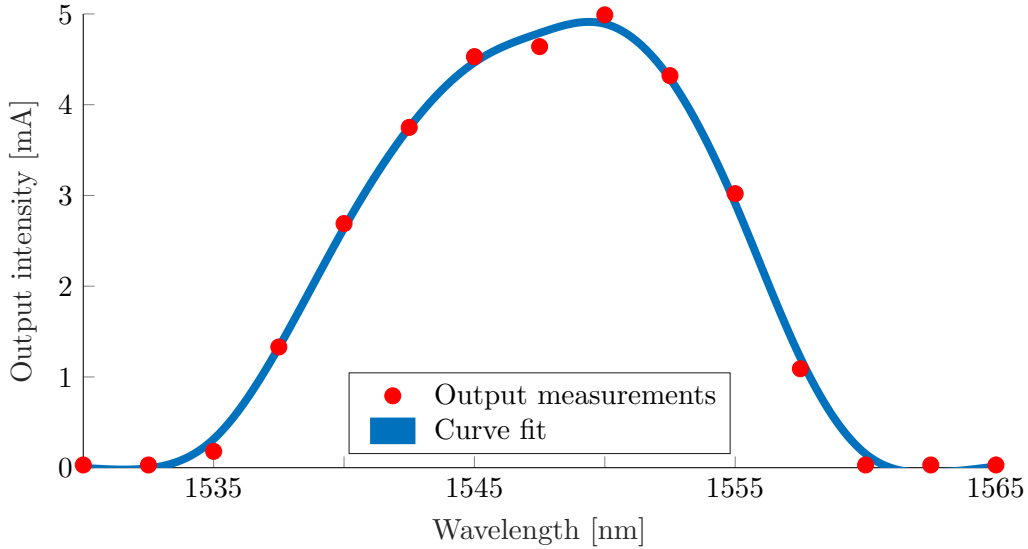
the intensity of the laser output was examined for different wavelengths and for different values of the power supplied to the laser. It turned out that the output intensity varied significantly for different wavelengths, and that the range of wavelengths the laser was able to produce was also highly dependent on the power supplied to the laser. These laser characteristics resulted in two issues for our measurements:

1. First of all, if a high-intensity laser beam is incident on our grating structures it is possible that light absorption in the silicon structures or the silica cladding could cause our device to heat up significantly and become damaged. We have not examined in detail at which intensities this occurs, but other members of the research group recommended that we kept the supplied power to the laser below 200 mW to be on the safe side. At this input power, the laser was able to produce wavelengths between approximately 1520 nm and 1590 nm. This did restrict which wavelengths we were able to test, but it was not deemed to be very problematic since the wavelength of interest, 1550 nm, was located well within this range.
2. A bigger problem arose when we discovered that the photodiode amplifier used in our setup was unable to measure signals stronger than approximately 5.3 mA without becoming saturated. This value was exceeded for almost the entire supported wavelength range when 200 mW of power was supplied to the laser. Since coupling efficiency calculations require measurements of both the direct laser output intensity, and the intensity after the laser light has coupled into and out of our grating structures, it was deemed necessary to reduce the power supplied to the laser even further.

A power of 130 mW was found to keep the laser output just below 5 mA for all wavelengths – avoiding saturation. This caused a significant reduction in the range of wavelengths supported by the laser, and limited our characterizations to wavelengths between approximately 1545 nm and 1585 nm. The fact that we are restricted to such a narrow range is very unfortunate, but it was deemed better than to be unable to calculate coupling efficiencies at all. If we had been completely unable to achieve any coupling for these wavelengths, a possibility would have been to increase the supplied power to the laser temporarily to check if our structures supported wavelengths outside this range. Luckily, this was not necessary, as will become evident from our discussions in the rest of this section.

As indicated in the flowchart on page 54, a computer is connected to both the motor controller and the photodiode amplifier in our setup. This enables fine-tuned wavelength control and accurate measurements of the output intensities as a function of the wavelength. A problem, however, is that the signal from the amplifier to the computer is capped at 1.6 mA, which is significantly less than the direct laser output. Measurements of the laser output therefore had to be conducted by first using the computer to adjust the laser wavelength and then manually reading the intensity from the amplifier display.

Measurements of the direct laser output were made at 5 nm intervals for wavelengths in the 1530 nm to 1600 nm range. Some of these wavelengths are



**Figure 4.11:** Scatter plot of the output intensities measured directly from the laser source and a plot of the curve fit that was found by performing a regression analysis on these measurements. The curve fit had an R-squared value of 0.9985, indicating a good goodness of fit. Measurements were conducted with 130 mW of power supplied to the laser.

outside the range we found to be supported by the laser at 130 mW supplied power, but were included to improve regression analyses later on. The result of our manual measurements can be seen as red circles in [Figure 4.11](#).

The intensity of the laser beam will be significantly reduced by being coupled into one grating structure and out of another. Even if we were to achieve the maximum theoretical coupling efficiency of 44% per uniform grating coupler, the maximum intensity of the output beam would be  $5 \text{ mA} \cdot 0.44^2 \approx 0.97 \text{ mA}$ , which is far below the cap of 1.6 mA between the amplifier and the computer. We were therefore able to perform automatic sweeps over different wavelengths at 0.1 nm resolution when measuring the output from our grating couplers.

To be able to calculate coupling efficiencies at the same 0.1 nm resolution, a MATLAB curve fitting tool was used to find estimated values for the laser output at all wavelengths in the 1530 nm to 1600 nm range. The curve fitting analysis was done using a “smoothing splines”-model based on piecewise polynomial regression [69]. The result can be seen in [Figure 4.11](#). The curve fit looks reasonable and feature an R-squared value of 0.9985, which indicates that it fits the measured values well. This fitted curve was therefore used as a reference in all subsequent coupling efficiency calculations. It should be emphasized, however, that the curve fit is only an approximation, and we will keep this in mind when analyzing the final results.

The characteristics of our laser have now been established and it is time to look at the results from grating coupler output measurements. As described in section 3.6.3, many different grating couplers were tested for different wavelengths and incidence angles. The measured output intensities were compared with the curve fitted data for the laser source, and coupling efficiencies could then be calculated as a ratio between the output after the laser beam had cou-



pled into and out of our structures and the intensity of the direct laser output.

Now, as mentioned in section 3.4.5.2, two sets of grating and taper couplers were connected by a 2 mm long waveguide to enable both in- and out-coupling. Since efficiencies stack multiplicatively, the coupling efficiency for one grating coupler, one taper coupler and 1 mm of the waveguide can be calculated as the square root of the coupling efficiency for the structure as a whole. Losses in the taper structure should be very small, as we discussed in 3.4.5.2, and will therefore be assumed to be negligible in our calculations.

Waveguide losses have not been characterized in this thesis, but have been examined previously by a member of the research group, Jens Høvik [70]. The losses associated with propagation in waveguides similar to ours were then found to be approximately  $2 \text{ dB cm}^{-1}$ , which corresponds to a power loss of approximately 4.5 % for our 1 mm long waveguides. This value has been used to factor out waveguide losses in our coupling efficiency calculations.

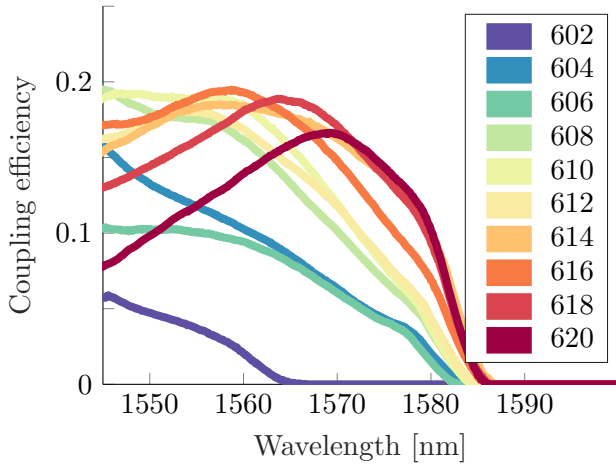
The coupling efficiency results found for one of our fabricated prototypes can be seen in Figure 4.12 on page 75. Due to alignment difficulties, we were unable to achieve coupling for all structures at all angles, and data series for some silicon grating widths are therefore missing from some of the plots. The measurements we were able to conduct are sufficient to draw some conclusions, however. Two important observations can be made from the results in Figure 4.12:

1. First of all we see that increased silicon grating widths tend to shift our coupling efficiency distributions towards higher wavelengths, which is consistent with the simulation results we presented in section 4.1.3.1. Unfortunately, very few peaks are present within the narrow wavelength range we were able to test, but some quick estimates on the available peaks seem to indicate the wavelength shift in nanometers is approximately 2.5 times the nanometer increase in silicon grating width. Returning to the corresponding simulation results in Figure 4.4 on page 61, we find a slightly lower value for this ratio: approximately 2.0.

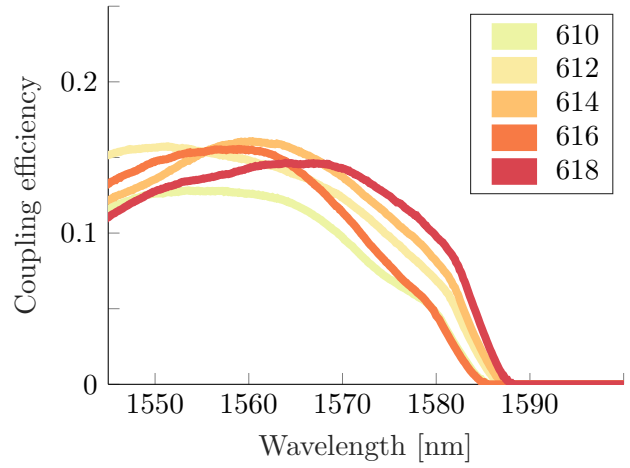
Due to the low number of peaks present in our experimental results, this difference can likely be attributed to the margin of error. Structural defects, surface roughness and similar effects are likely also contributing factors to the difference between the ideal structures in our simulations and the manufactured devices. It is therefore difficult to say whether or not our experimental results are in line with our simulations, but we can at least conclude that the correspondence is in fact quite good.

2. A second observation that can be made from Figure 4.12 is that increased incidence angles tend to shift our coupling efficiency distributions towards the left, i.e. towards shorter wavelengths. The same effect was also observed in our simulations, and was discussed in section 4.1.3.1. The lack of peaks in the included parts of the distributions makes it difficult to do any quantitative analysis, and we will therefore only conclude that the general trend is the same for both experimental and simulation results.

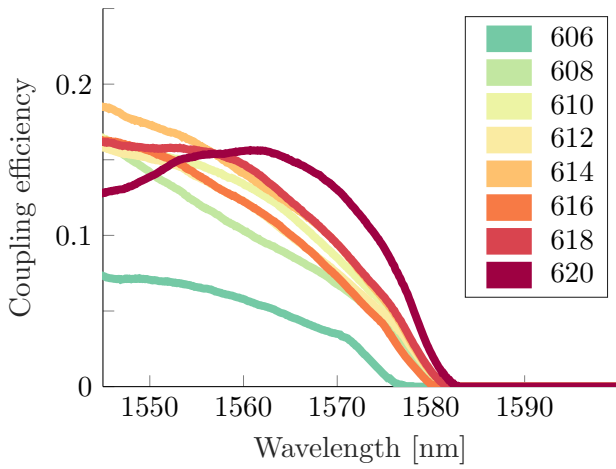
Now, the fabrication of virtually defect-free structures is difficult even for fully optimized automated systems. When prototypes are manufactured in a



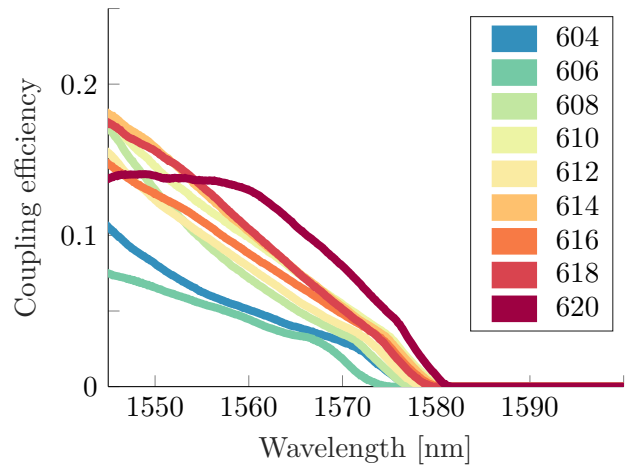
(a) 12° incidence angle.



(b) 14° incidence angle.



(c) 16° incidence angle.



(d) 18° incidence angle.

**Figure 4.12:** Plots of the calculated coupling efficiencies for a single grating coupler as a function of wavelength and the silicon grating width for four different incidence angles. Colors are used to indicate which silicon grating widths were used for the different data series, and these widths are given in nanometers. Similar colors are used for the same widths across all plots to facilitate comparisons. The sample these measurements were conducted on was a uniform grating coupler exposed at a  $150 \mu\text{C cm}^{-2}$  EBL area dose.

laboratory and many of the processing steps are done manually, a significant amount of defects is likely to be present in the resulting devices. Any light-scattering defects in our waveguides are easily observable by the infrared camera in our characterization setup. Such defects were observed for all of our structures, but the amount of defects and the intensity of the light scattered toward the camera lens varied significantly. Defects, together with alignment difficulties, makes it difficult to draw any conclusions from the relative coupling efficiencies seen in [Figure 4.12](#).

What we can say, however, is that the best result we found for the efficiency of a single, uniform grating coupler at a 1500 nm wavelength was  $\approx 19.1\%$ . This was found for a structure featuring silicon grating widths  $w_{\text{Si}} = 610$  nm and air grating widths  $w_{\text{air}} = 80$  nm, characterized at a  $12^\circ$  incidence angle. Similar coupling efficiencies have also been found for other samples manufactured using the same design files, indicating that this result should be possible to achieve fairly reliably. These other samples featured high coupling efficiencies for somewhat different angles and grating dimensions, but this is likely attributed to slight variations in the fabrication processes.

### 4.3 Comparison: simulation and fabrication

We have already compared some of the similarities that were observed between our simulation and fabrication results. In this section we will primarily focus on the difference in maximum coupling efficiency achieved for the theoretical and experimental approaches. We will discuss potential sources of error and how they could affect our results, and will also provide some suggestions as to how the effect of these errors could be reduced.

The best coupling efficiency we found in our simulations was  $62\%$ , but this was for an apodized grating structure that we have not attempted to make experimentally. We will therefore primarily discuss the maximum coupling efficiency for uniform grating couplers, which has been found to be  $44\%$  in simulations and  $19\%$  for fabricated prototypes. The performance of fabricated grating couplers relative to the simulated ones can therefore be found to be  $\eta_{\text{rel}} = 19/44 \approx 43\%$ .

As we have covered extensively in [section 3.1.3](#), the geometry of our simulation models have been simplified to two dimensions to reduce memory and processing power requirements. This led to the omission of taper couplers in our simulations. Now, taper couplers are included in our fabricated devices, but their losses are assumed to be negligible. Any non-zero taper loss would therefore be attributed to the grating structure instead of the taper structure in our calculations. If the taper loss was e.g.  $2\%$  this would imply that the coupling efficiencies of our fabricated grating couplers in reality are  $1/(1 - 0.02) - 1 \approx 2\%$  higher than our initial estimates.

The simplification to 2D also introduces a second potential source of error, since no light can leak from the waveguide along the dimension that we have assumed to be of infinite extent. This would likely not be a significant issue for an ideal waveguide, but since manufactured silicon structures will feature some



degree of surface roughness, it is not unlikely that this is a significant source of losses that are not accounted for in our simulations.

Surface roughness and suboptimal silicon quality is in general likely the primary causes of the discrepancies we have seen in the coupling efficiencies for simulated and fabricated devices. We have not characterized the quality of the deposited silicon layer and have not examined the surface properties of our silicon structures. Structural defects have only been qualitatively examined by camera-aided visual inspections, where we have looked for scattering centers in the waveguide. All of these effects result in reduced coupling efficiencies for our fabricated prototypes and are not included in our simulations at all. If they had been included in our COMSOL models, they would very likely have resulted in a lower simulated coupling efficiency result and a higher value for  $\eta_{\text{rel}}$  overall.

The quality of our silicon structures could likely be improved if the fabrication procedure is optimized further and implemented as an automatic process. Manual lab procedures are especially prone to contamination, as well as inconsistencies between runs. If the biosensing device developed by the research group reaches the mass production stage it is likely that higher-quality silicon will be used, which will probably result in increased coupling efficiencies.

Fabrication procedures are not the only procedures that are negatively affected by manual operations. The characterization equipment used to measure coupling efficiencies for our fabricated devices has also relied on manual alignment, and suboptimal fiber angles and placements could potentially affect our results as well. We estimate that the angular adjustments of our fibers should be within  $0.5^\circ$  of the intended angles, and the coupling efficiency was shown not to deviate significantly within such a narrow range of angles in the project thesis [1]. The positional alignment of the fibers, on the other hand, was shown to have a big effect on the coupling efficiency [1]. Since the resolution of the lateral adjustment knobs in our setup was limited, it is not unlikely that better coupling efficiencies could have been found with more accurate positioning systems.

The curve fit that we used in section 4.2.3 to estimate the output distribution for the laser could of course be inaccurate for some values, which would have increased or decreased calculated coupling efficiencies at different wavelengths. This would not have affected the coupling efficiencies measured at 1550 nm significantly, since the difference in output laser intensity for the measured and curve fitted value was less than 1 % at this wavelength.

Waveguide losses is another potential cause of error. We have used the values reported in [70], where similar fabrication procedures were used, to estimate the waveguide losses. If these losses are higher or lower than these values, the coupling efficiencies of our grating couplers should be higher or lower than initially calculated, respectively.

To summarize: there are a lot of different factors that could affect the coupling efficiencies for both simulated and fabricated prototypes, many of which have very limited impacts on our results. The factors that potentially have large impacts, such as structural silicon defects and surface roughness, have likely affected our fabrication results negatively and have not been included

in simulations. Improvements to the fabrication processes and the inclusion of these factors in simulations could therefore potentially bring the respective results more in line with each other.

## Chapter 5

# Summary and conclusion

The development of miniaturized laboratory systems has become an important area of research for integrated photonics in recent years. Many different types of sensors based on light modulation can be incorporated into these devices and provide low-cost, precise measurements of for example blood glucose levels. A challenge, however, is that the submicron dimensions of the integrated photonic structures makes it difficult to couple sufficient amounts of light into them. The use of high-intensity laser sources both increases production costs and has the potential to damage the structures, and high-efficiency coupling of low-intensity sources is therefore preferable.

The main objective in this thesis has been to optimize and fabricate a silicon-on-insulator grating coupler that provides high coupling efficiency between an optical fiber and a submicron waveguide. The grating coupler has been designed to be compatible with a lab-on-a-chip biosensing device currently being developed by the photonic research group at the Norwegian University of Science and Technology.

### 5.1 Simulation

Fiber-to-waveguide grating couplers were initially designed and optimized using COMSOL Multiphysics, which is a numerical simulation software based on the finite-element method. All simulations were simplified to two dimensions to reduce memory and processing power requirements, and both uniform and apodized grating structures were examined. The validity of our meshing procedures was tested before any simulations were run, and was also regularly verified to ensure that the meshing remained valid for all examined wavelengths and model geometries.

The apodized grating coupler design was optimized using a four-step algorithm that iterated over different grating dimensions and grating separations, as well as different incidence angles and lateral displacements of the optical fiber source. The algorithm was applied to two different starting points and more than 8000 simulations were run for each of these optimization processes. All simulations were conducted with a 1550 nm wavelength, and the best coupling efficiency found for the apodized design was  $\approx 62.2\%$ . This value is comparable

to other results found in literature for similar structures [19–21, 68].

A simulation model of a uniform grating coupler that was developed by the author in previous work has also been examined further in this thesis. The coupling efficiency of this design has previously been shown to be  $\approx 44\%$ , and in this thesis we have examined the wavelength-dependence of this result for different incidence angles and grating dimensions. Shifts towards longer wavelengths were observed for increased silicon grating widths and shifts towards shorter wavelengths were observed for increased incidence angles. With the exception of incidence angles smaller than  $\approx 8^\circ$ , none of these wavelength shifts were accompanied by a significant reduction in the maximum coupling efficiency.

## 5.2 Fabrication

Uniform grating couplers with different grating dimensions were made experimentally in a cleanroom environment using plasma-enhanced chemical vapor deposition, electron-beam lithography and inductively coupled plasma reactive-ion etching techniques. The wavelength-dependence of these grating couplers agreed nicely with the trends observed in our simulations, but the structures featured lower coupling efficiencies overall. The highest coupling efficiency observed for the manufactured grating couplers was 19.1%.

Our fabrication procedures were limited to a  $150\ \mu\text{C cm}^{-2}$  area dose to ensure compatibility with devices being developed by the photonic research group at the Norwegian University of Science and Technology, but dose tests were nevertheless conducted to examine if this was the optimal value. A scanning electron microscope was used to take individual images of 108 silicon lines and a MATLAB script was used for image analysis and optimal dose calculations. We were unable to reach a definite conclusion due to limited image resolution, but suspect that the aforementioned value for the area dose is too high.

## 5.3 Future research

Throughout this thesis we have discussed potential improvements of the methods and procedures that have been used for both simulations and fabrication. A condensed list of the most important suggestions is provided below, and also includes some additional ideas for future work:

- Improve the algorithm that was used to optimize apodized grating structures in our simulations. This could for example be done by using semi-randomized values or cycling through a predetermined set of values for the step parameter  $\Delta$ . Rewriting the algorithm to support parallel processing would also allow significantly faster solution convergence on computer systems with multiple processor cores or hyperthreading support.
- Fabricate grating coupler prototypes using the apodized design, which has been shown to have significantly higher coupling efficiencies in simulations than their uniform counterpart.

- Optimize fabrication procedures to reduce surface roughness and the number of material defects. A fully-automated process would be ideal, since this would make it easier to reduce contamination and get consistent results every time.
- Improving the characterization equipment to allow more accurate alignment and more precise measurements. The use of a laser source with a broader bandwidth would also be preferable.
- Incorporate the grating coupler designs into the lab-on-a-chip biosensor that is currently being developed by the photonic research group at the Norwegian University of Science and Technology.

## 5.4 Conclusion

The main goal of this master's thesis was to optimize and fabricate a silicon-on-insulator grating coupler to enable efficient coupling of light between an optical fiber and a waveguide. Coupling efficiencies of 44 % and 62 % have been demonstrated in simulations for uniform and apodized grating structures, respectively. Uniform grating coupler prototypes were also manufactured and have been shown to feature coupling efficiencies of up to 19 %, which is significantly higher than currently-employed butt coupling techniques.

Although there are many improvements to be made to both simulation and fabrication procedures, we can therefore conclude that the main goal of this thesis has been successfully achieved.

## Appendix A


# Tutorial: COMSOL Multiphysics









The goal of this tutorial is for the reader to be able to build their own model of a simple silicon-on-insulator grating coupler, run physics simulations on this model and analyze the results. The tutorial will provide step-by-step instructions, and assumes that the reader already has COMSOL Multiphysics 5.4 [36] installed on their computer. A valid license for the Wave Optics Module [38] is also a prerequisite.

COMSOL Multiphysics is a quite extensive physics modeling software, and this tutorial does not aim to cover all features in detail. The interested reader is instead referred to [71] for a general introduction to the software and to [72] for a more in-depth description of the Wave Optics Module.

To make this tutorial easier to follow, all direct references to user interface elements in COMSOL Multiphysics will be highlighted with a green background color. Where applicable, the icons used by COMSOL in conjunction with these user interface elements will also be included.

### A.1 Initial setup

Launch COMSOL Multiphysics and select  Model Wizard. The model wizard is a good starting point, as it allows us to set up some initial project configurations. We can set a dimensionality for our model, choose the physics interfaces we would like to use and add studies to define how the model should be analyzed.

1. Select  2D as the Space Dimension.
2. Select  Optics ►  Wave Optics ►  Electromagnetic waves, Frequency Domain (ewfd) as the physics interface and click Add.
3. Click  Study to proceed.
4. Select  General Studies ►  Frequency Domain as the study.
5. Click  Done to complete the initial setup.

## A.2 Parameters

When we now set out to construct our model geometry, it is important to keep in mind that we might want to change certain aspects of it later on. Perhaps we want to change the grating dimensions as part of an optimization process, or maybe we want to do a sweep over different incident angles for the laser source. It would therefore be beneficial to define some fundamental parameters that we can use as variables when we construct our geometry.

1. Select **Parameters 1** in the **Model Builder** window on the left.
2. Copy all parameter names and values from **Table A.1**. The parameter descriptions are not mandatory, but it is good practice to give parameters a clear description.

Note that it is possible to create multiple parameter groups by right-clicking **Global Definitions** in the **Model Builder** window and selecting **Parameters**. The parameter groups can also be renamed by right-clicking them directly. This is a useful organizational feature for projects that require a large number of parameters. To keep things simple, we will only use a single parameter group for now.

**Table A.1:** Names, values and descriptions of the COMSOL parameters that should be defined in this tutorial.

Name	Value	Description
wg_h	220[nm]	Waveguide height
wg_l	60[um]	Waveguide length
cl_t	1[um]	Cladding thickness
sub_t	7[um]	Substrate thickness
air_t	18[um]	Air thickness
pml_t	1[um]	PML thickness
port_h	wg_h+2*cl_t	Port height
g_w_air	0.11[um]	Grating width (air)
g_w_Si	0.58[um]	Grating width (silicon)
f_h	100[nm]	Fibre port height
f_l	40[um]	Fibre port length
f_d	3[um]	Fiber bottom-to-waveguide distance
a	16.3[deg]	Incident angle (>0)
w0	10.4[um]/2	Gaussian mode field diameter
x0	(1/2)*f_h*sin(a)	Gaussian mean in x
y0	-(1/2)*f_h*cos(a)	Gaussian mean in y
n_air	1	Refractive index of air
n_Si	3.48	Refractive index of Si
n_SiO2	1.45	Refractive index of SiO2
wl	1550[nm]	Wavelength
fq	c_const/wl	Frequency

## A.3 Geometry

In the Model Builder hierarchy on the left, all model geometries are by default located within the **Component 1** ▶ **Geometry 1** node. Geometrical elements of different shapes, such as rectangles and circles, can be added by right-clicking the **Geometry 1** node and selecting the desired shape. Shape settings, such as the width and height, can be found in the Settings window, which is located between the Model Builder and the Graphics window when the geometry element has been selected. Note that the **Position** ▶ **Base** setting should be set to **Center** for all geometry elements in this tutorial.

1. Create 9 new rectangles, which will be used to represent different aspects of the grating coupler geometry.
2. Configure the settings and labels of the rectangles as specified in the green boxes on page 85.

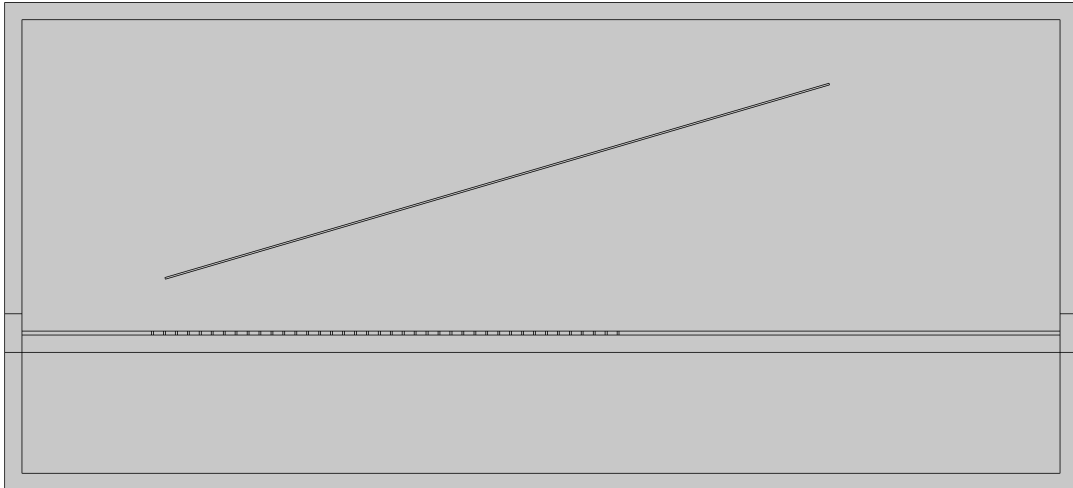
Most of the model geometry has now been defined. The only thing that remains is to duplicate the single grating we have made to make the complete grating structure. Instead of duplicating the geometry element 40 times and individually changing their positions, we use the built-in array feature:

1. Right click **Geometry 1** and select **Transforms** ▶ **Array**.
2. Assign the single grating we made previously as an **Input object** in the array settings.
  - This can be done by making sure that the switch is set to **ON/Active** under the **Input** settings, and then clicking on the single grating in the **Graphics** window. It is recommended to zoom in a bit to ensure that the correct domain is clicked on.
3. Configure the newly created **Array 1** element with the following settings:
  - **Array type:** Linear
  - **Size:** 40
  - **Displacement in x:**  $-(g\_w\_air + g\_w\_Si)$
  - **Displacement in y:** 0

The entire model geometry should now be defined, and it is time to inspect it to verify that everything works. This can be done by selecting **Geometry 1** and clicking the **Build All** button in the settings. The same button is also available on the Home tab for easy access. Make sure that the geometry is configured correctly by comparing it to **Figure A.1** on page 86. If there are deviations, verify that all the geometry elements are configured according to this tutorial and that the **Position** ▶ **Base** property is set to **Center** for all geometry elements.



Waveguide			
Width:	wg_l	x-position:	0
Height:	wg_h	y-position:	0
Rotation: 0			
Oxide cladding			
Width:	wg_l	x-position:	0
Height:	cl_t	y-position:	-(cl_t + wg_h)/2
Rotation: 0			
Substrate			
Width:	wg_l	x-position:	0
Height:	sub_t	y-position:	-(sub_t + wg_h)/2 - cl_t
Rotation: 0			
Air region			
Width:	wg_l	x-position:	0
Height:	air_t	y-position:	(air_t + wg_h)/2
Rotation: 0			
PML			
Width:	wg_l + pml_t * 2		
Height:	air_t + wg_h + cl_t + sub_t + 2 * pml_t		
x-position:	0		
y-position:	(air_t - cl_t - sub_t)/2		
Rotation:	0		
Left port			
Width:	pml_t	x-position:	-(wg_l + pml_t)/2
Height:	port_h	y-position:	0
Rotation: 0			
Right port			
Width:	pml_t	x-position:	(wg_l + pml_t)/2
Height:	port_h	y-position:	0
Rotation: 0			
Single grating			
Width:	g_w_air	x-position:	4.4[um] + g_w_air/2
Height:	wg_h	y-position:	0
Rotation: 0			
Port fiber			
Width:	f_l		
Height:	f_h		
x-position:	-sin(a)*(cos(a)*f_h + sin(a)*f_l + 2*f_d)/(2*cos(a))		
y-position:	f_d + (f_l*sin(a) + f_h*cos(a) + wg_h)/2		
Rotation:	a		



**Figure A.1:** How the geometry should look after finishing section A.3 of this tutorial.

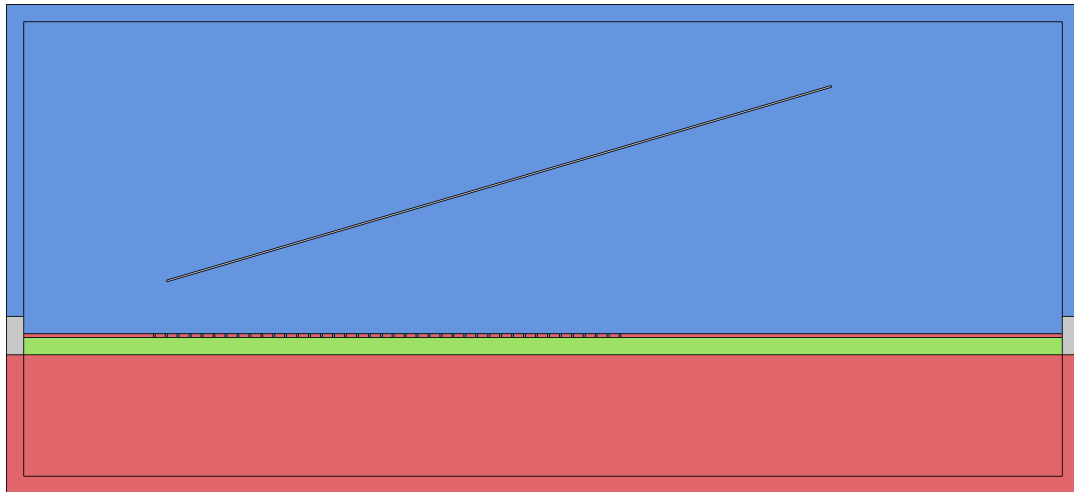
## A.4 Materials

Now that the geometry is finished, we can continue by assigning materials to the various geometry domains in our model.

1. Right-click **Materials**, located under **Component 1** in the **Model Builder** hierarchy.
2. Select **Blank Material**.
3. Repeat the above steps until a total of 3 blank materials have been created.
4. Label the materials **Air**, **Si** and **SiO<sub>2</sub>**.
5. Assign the materials to the different geometry domains as specified in **Figure A.2** on page 87.
  - The procedure for assigning materials is the same as that used to assign the single grating element to the array element in section A.3.
6. Define the real parts of the refractive indices of the materials (available under **Material Contents** ► **Refractive index, real part** when a material is selected).
  - Air:  $n_{\text{air}}$
  - Si:  $n_{\text{Si}}$
  - SiO<sub>2</sub>:  $n_{\text{SiO}_2}$



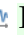

## A.5 Perfectly matched layer

To avoid light being reflected off the edges of the geometry and interfering with our simulation, we should define a non-reflecting layer that absorbs incident






**Figure A.2:** Overview of which materials should be assigned to the different domains of the model. Blue areas should be air, green areas should be SiO<sub>2</sub> and red areas should be Si. The fiber port and the ports at the left and right hand side of our model should not be assigned any materials, and are colored gray. Note that the air holes in the grating structure are colored blue, and that the air material therefore should be assigned to these geometry domains. This figure is included on page 28, but is repeated in this tutorial as well for completeness.

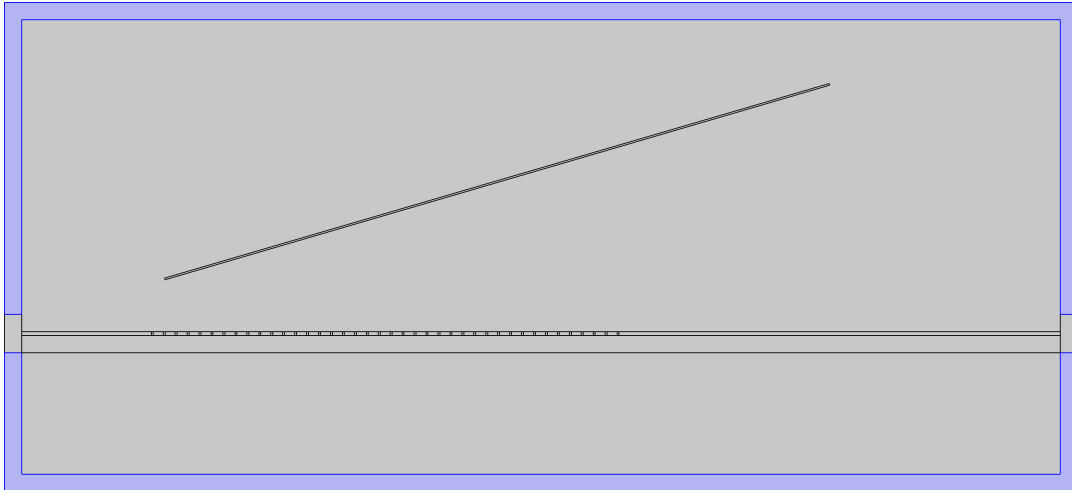
radiation. COMSOL provides perfectly matched layers (PML) that can be used for this purpose, which essentially absorb all incident radiation by virtue of having a complex-valued permittivity and permeability.

1. Right-click the  **Definitions** node located under  **Component 1** in the **Model Builder** hierarchy, and select  **Perfectly Matched Layer**.
2. Assign domains to the newly created  **Perfectly Matched Layer 1** node as specified in [Figure A.3](#).

## A.6 Physics interface

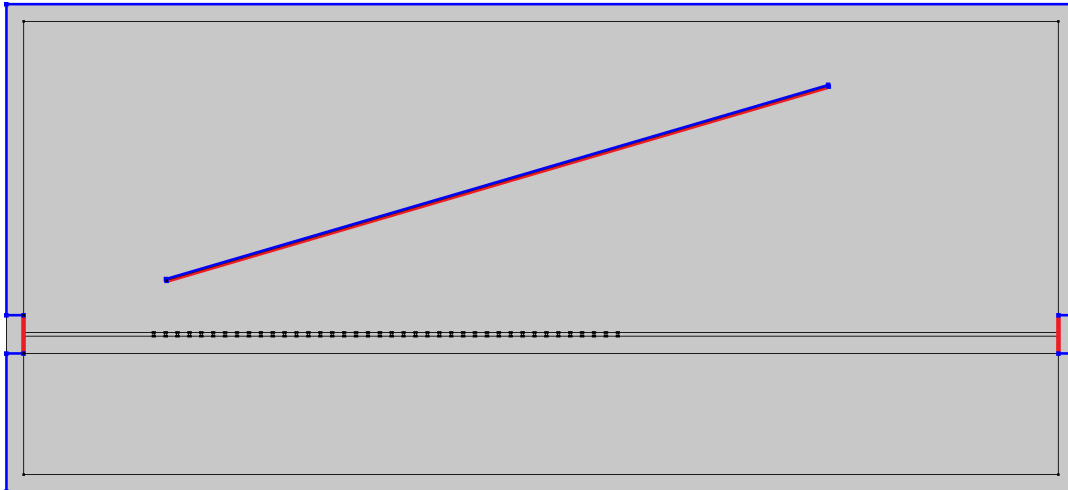
The physics interface we will be using,  **Electromagnetic Waves, Frequency Domain (ewfd)**, has already been selected during the initial setup in section [A.1](#). However, the initial configuration of the interface will have to be changed somewhat to reflect the physics in the model we are designing.

1. Select  **Electromagnetic Waves, Frequency Domain (ewfd)** in the **Model Builder** hierarchy.
2. Deselect the domains corresponding to the left, right and fiber ports from the **Domain Selection** panel.
  - To enable highlighting of the selected geometry element, click the  button close to the top of the **Settings** page when a geometry element is selected.



**Figure A.3:** Overview of which domains should be assigned to [Perfectly Matched Layer 1](#) in section [A.5](#). Note that there are no grating or fiber domains assigned, only the outermost domains.

3. Right-click [Electromagnetic Waves, Frequency Domain \(ewfd\)](#) and add a [Scattering Boundary Condition](#).
4. Assign boundaries to the newly created [Scattering Boundary Condition 1](#) as specified in [Figure A.4](#) on page [89](#).
5. Right-click [Electromagnetic Waves, Frequency Domain \(ewfd\)](#) and select [Port](#).
6. Repeat the above step until a total of three [Port](#) elements have been created.
7. Configure the settings of the newly created ports as specified in [Table A.2](#) on page [89](#).
8. Assign boundaries to the port elements as specified in [Figure A.4](#).
  - The leftmost red, highlighted boundary should be assigned to the newly created [Left Port](#), the rightmost boundary to [Right Port](#) and the topmost boundary to [Fiber Port](#).
  - The boundaries of the left and right ports are split into three pieces each – make sure to select all the pieces.
  - COMSOL will display some red arrows when the port boundaries are selected. The direction of these arrows are arbitrary, and does not matter.



**Figure A.4:** Overview of which domain boundaries that should be defined as scattering boundaries and port boundaries in the physics interface of our model. These boundaries separate the actively simulated areas from the areas which we are not actively simulating, as well as the areas outside of our defined geometry. Scattering boundaries are highlighted in blue, while port boundaries are highlighted in red. Note that three of the fiber boundaries are blue – only the bottom boundary is red.



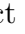



**Table A.2:** Settings used to configure the ports of the physics interface in this tutorial.

Label	Left port	Right port	Fiber port
Port name	1	2	3
Type of port	Numeric	Numeric	User defined
Wave excitation at this point	Off	Off	On
Electric mode field			x: 0 y: 0 z: $\exp(-((x-x_0)^2+(y-y_0)^2)/(w_0^2))$
Propagation constant			$2\pi/w_1$

## A.7 Meshing



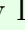
Before simulation can begin we need to define how the model mesh should be constructed. The *mesh* is a discretization of our simulation area, which enables COMSOL to use numerical methods to solve the partial differential equations defined in the chosen physics interface. The error in the numerical approximation is dependent on the size of the mesh elements, and it is therefore important that the maximum size of the mesh elements is small enough for the errors to be negligible. According to [72], the maximum mesh element size should be smaller than 1/10 of the wavelength.




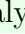

1. Right-click **Mesh 1** and select **Free Triangular**.

2. Select the newly created  Free Triangular 1 and assign all geometry domains except the left, right and fiber ports in the Domain Selection panel in the Settings window.
  - The easiest way to do this is to first change Geometric entity level to Domain, change Selection to All domains and then deselect the three domains corresponding to the ports.
3. Select the  Size node located under  Mesh 1 and configure it using the following settings:
  - Maximum element size: 130 [nm]
  - Minimum element size: 8E-10
  - Maximum element growth rate: 1.1
  - Curvature factor: 0.2
  - Resolution of narrow regions: 4
4. Verify that the meshing procedure works by clicking on  Build Mesh on the Mesh tab. This button is also available as  Build All in the Settings window when the  Mesh 1 node is selected.

The mesh settings we have listen above are chosen based on the wavelength of our fiber source and optimizations that was part of my project thesis [1].

## A.8 Study configuration


Only one thing remains before we can run our grating coupler simulation: configuration of the study. The study determines which simulations should be run and allows us to run sweeps over different parameters. When  Frequency Domain was selected as the main study during the initial setup in section A.1, COMSOL automatically added the  Study 1 node to the Model Builder hierarchy, as well as a  Frequency Domain study step. We need to alter this step slightly, and add three more steps to account for the ports we defined in section A.6.





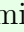
1. Select the  Frequency Domain study step and change the value of the Frequencies field in the Study Settings panel in the Settings window to  $f_q$ .
2. Right-click  Study 1 and select Study Steps ► Other ►  Boundary Mode Analysis.
  - Repeat this until a total of three  Boundary Mode Analysis steps have been created – one for each port.
3. Configure the settings of the three  Boundary Mode Analysis nodes as specified in Table A.3.





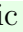
**Table A.3:** Settings used to configure the  Boundary Mode Analysis study steps.

Label	Left port	Right port	Fiber port
Port name	1	2	3
Mode analysis frequency	fq	fq	fq
Desired number of modes	<input checked="" type="checkbox"/> 1	<input checked="" type="checkbox"/> 1	<input type="checkbox"/>
Search for modes around	<input checked="" type="checkbox"/> n_Si	<input checked="" type="checkbox"/> n_Si	<input checked="" type="checkbox"/> n_air

## A.9 Simulation and results

Everything should now be ready to run our simulation. Click the  Compute button on the Home tab and wait until the simulation is completed. The current progress can be seen by clicking the Progress tab below the Graphics window. Additional information is also available in the Messages and Log tabs, located to the left and right of the Progress tab, respectively.

All results will be available in the  Results node in the Model Builder hierarchy when the simulation has finished. The first time a simulation is run, COMSOL calculates and outputs certain values by default. These are available under  Results ►  Tables ►  Table 1. We are mostly interested in the fraction of the fiber port output that is coupled into the waveguide and that propagates to the right port. This is one of the aforementioned default values, and can be seen under the Transmittance, port 2 (1) column in  Table 1. If the instructions in this tutorial have been followed accurately, this value should be 0.44789 – meaning that the grating coupler in this model yields a theoretical coupling efficiency of 44.789%.

A visualization of the norm of the electric fields in our simulation can be seen in the Graphics window when the  Results ►  Electric Field (ewfd) ►  Surface 1 node is selected. Additional plots and calculations can be found by right-clicking the  Derived Values and  Electric Field (ewfd) nodes and selecting the desired options.

## A.10 Tips and tricks

The main scope of this tutorial is finished, but I will briefly include some tips and tricks that I have found to be very useful when working with COMSOL Multiphysics.

### A.10.1 Automated domain and boundary assignment

Throughout this tutorial we have assigned geometry domains and boundaries to different nodes in the Model Builder hierarchy manually. This works great for a static model, but problems arise when the geometry (or parameters affecting the geometry) is changed. This is especially true when additional domains are added or created, as COMSOL then has to guess how the new or remaining domains should be assigned to the different nodes.

A way to remedy this is to use the built-in **Selections** feature, which can be found by right-clicking the **Geometry 1** node. By combining the different selection tools, as well as the **Selections of Resulting Entities** panel available in the settings of all geometry elements, one can automate the assignment of domains to the different nodes. This allows much more flexible parametric sweeps to take place without constantly monitoring COMSOL to look for errors.

### **A.10.2 Interfacing with third-party software**

Parametric sweeps are available as a built-in feature in COMSOL Multiphysics, but the sweeps do not allow complex calculations to be performed to determine how parameters should change between iterations. Fortunately, COMSOL can be run as a server that integrates with third-party programming languages such as MATLAB, Java and Visual Basic for Applications (VBA). These external tools allow more complex sweeps to be performed by starting simulations and analyzing data outside of COMSOL Multiphysics itself.

I have been using the interface with MATLAB throughout my master's thesis, and although there is a bit of a learning curve, I would highly recommend using this approach for other projects as well. It should be mentioned that COMSOL Multiphysics features an application builder that likely could be used in a similar fashion, but this functionality has not been examined in detail.



## Appendix B

# Matlab code

### B.1 Analysis of line widths in SEM images

```
1 %% Analysis of rectangular, straight lines in vertically
   oriented SEM images
2
3 % Set scale and dimensions of SEM image (excluding bottom
   scale bar)
4 nm_per_px = 500/554; % The 500 nm scale bar is 554 pixels
   wide in our images
5 dim.x = 1536; % Horizontal image resolution
6 dim.y = 1024; % Vertical image resolution
7
8 % Set threshold for line width measurements (0.0-1.0)
9 threshold = 0.5;
10
11 % Get all tif files in directory
12 files = dir('*.tif');
13
14 % Initialize struct to store line data
15 data.dose = [];
16 data.intended_width = [];
17 data.measured_width = [];
18
19 % Iterate over all individual files
20 for i = 1:length(files)
21     % Read values of all pixels in SEM image
22     img = imread(files(i).name);
23
24     % Average all horizontal lines in image and shift to
       zero
25     img_mean = mean(img(1:dim.y,1:dim.x));
26     img_mean = img_mean - min(img_mean);
27
```

```

28     % Find line edges by looking at the pixel value
        gradients
29     img_gradient = gradient(img_mean);
30     [~, I_max] = max(img_gradient);
31     [~, I_min] = min(img_gradient);
32
33     % Find peaks and valleys close to line edges
34     right_valley = findNextValley(img_mean, I_min);
35     left_valley = findPrevValley(img_mean, I_max);
36     right_peak = findNextPeak(img_mean, I_max);
37     left_peak = findPrevPeak(img_mean, I_min);
38
39     % Calculate average heights of peaks and valleys
40     mean_peak_height = mean([img_mean(left_peak), img_mean(
        right_peak)]);
41     mean_valley_height = mean([img_mean(left_valley),
        img_mean(right_valley)]);
42
43     % Find line widths at threshold height
44     threshold_height = mean_peak_height * threshold +
        mean_valley_height * (1 - threshold);
45     left_index = findClosestValueInArray(img_mean,
        threshold_height, left_valley:right_peak);
46     right_index = findClosestValueInArray(img_mean,
        threshold_height, left_peak:right_valley);
47     measured_width = (right_index - left_index) *
        nm_per_px;
48
49     % Extract dose and intended line width from filename
50     dose = extractBetween(string(files(i).name), "D", "-");
51     intended_width = extractBetween(string(files(i).name)
        , "L", ".");
52
53     % Add results to data struct
54     data.dose = [data.dose dose];
55     data.intended_width = [data.intended_width
        intended_width];
56     data.measured_width = [data.measured_width
        measured_width];
57 end
58
59 %% Utility functions
60
61 function index = findNextValley(array, x)
62     lowest = array(x);
63     lowest_index = x;
64
65     i = x;

```

```

66     while(1)
67         [min_in_interval, temp_index] = min(array(i:i+9));
68         if (min_in_interval < lowest)
69             lowest = min_in_interval;
70             lowest_index = temp_index + i;
71             i = i + 10;
72         else
73             index = lowest_index;
74             return;
75         end
76     end
77 end
78
79 function index = findPrevValley(array,x)
80     lowest = array(x);
81     lowest_index = x;
82
83     i = x;
84     while(1)
85         [min_in_interval, temp_index] = min(array(i-9:i));
86         if (min_in_interval < lowest)
87             lowest = min_in_interval;
88             lowest_index = i - (9-temp_index);
89             i = i - 10;
90         else
91             index = lowest_index;
92             return;
93         end
94     end
95 end
96
97 function index = findPrevPeak(array,x)
98     highest = array(x);
99     highest_index = x;
100
101     i = x;
102     while(1)
103         [max_in_interval, temp_index] = max(array(i-9:i));
104         if (max_in_interval > highest)
105             highest = max_in_interval;
106             highest_index = i - (9-temp_index);
107             i = i - 10;
108         else
109             index = highest_index;
110             return;
111         end
112     end
113 end

```

```

114
115 function index = findNextPeak(array,x)
116     highest = array(x);
117     highest_index = x;
118
119     i = x;
120     while(1)
121         [max_in_interval, temp_index] = max(array(i:i+9));
122         if (max_in_interval > highest)
123             highest = max_in_interval;
124             highest_index = temp_index + i;
125             i = i + 10;
126         else
127             index = highest_index;
128             return;
129         end
130     end
131 end
132
133 function index = findClosestValueInArray(array,value,range
    )
134     array_diff = array(range) - value;
135     [~,range_index] = min(abs(array_diff));
136     index = range_index + range(1);
137 end

```

# References

- [1] Lars Olav Skrebergene. “Optimization of a fiber-to-waveguide silicon-on-insulator grating coupler”. Project thesis. Norwegian University of Science and Technology, 2019.
- [2] Ingerid Gjeitnes Hellen. “Simulation and fabrication of two-dimensional photonic crystal drop filters for biosensing”. Master thesis. Norwegian University of Science and Technology, 2018.
- [3] Lars Grønmark Holmen. “Simulation and Fabrication of a Photonic Crystal Mach-Zehnder Interferometer”. Master thesis. Norwegian University of Science and Technology, 2016.
- [4] Eivind Jülke Røer. “Optimization and Fabrication of Photonic Crystal Drop Filters for Optical Biosensing”. Master thesis. Norwegian University of Science and Technology, 2018.
- [5] Jens Høvik. “Photonic Crystal Waveguide Fabrication”. Master thesis. Norwegian University of Science and Technology, 2012.
- [6] Vijay Srinivasan, Vamsee K Pamula, and Richard B Fair. “Droplet-based microfluidic lab-on-a-chip for glucose detection”. In: *Analytica Chimica Acta. Microfluidics and Lab - On - a - Chip* 507.1 (Apr. 1, 2004), pp. 145–150. ISSN: 0003-2670.
- [7] Bahaa E. A. Saleh and Malvin Carl Teich. *Fundamentals of Photonics*. 2 edition. Wiley-Interscience, Mar. 9, 2007. ISBN: 978-0-471-35832-9.
- [8] Xingcun Colin Tong Ph.D. *Advanced Materials for Integrated Optical Waveguides*. Springer Science & Business Media, Oct. 17, 2013. ISBN: 978-3-319-01550-7.
- [9] Ajoy Ghatak and K. Thyagarajan. *An Introduction to Fiber Optics*. Cambridge University Press, June 28, 1998. ISBN: 978-0-521-57785-4.
- [10] Pavel Nikitin, Daniel Stancil, and Elena Erosheva. “Estimating the number of modes in multimode waveguide propagation environment”. In: *IEEE Antennas and Propagation Society, AP-S International Symposium (Digest)* (July 1, 2011).
- [11] Harry J R Dutton. *Understanding Optical Communications*. 1998.
- [12] Jr. Kowalevicz, Bucholtz Andrew M., and Frank. *Beam Divergence from an SMF-28 Optical Fiber*: Defense Technical Information Center, Oct. 6, 2006. URL: <http://www.dtic.mil/docs/citations/ADA456331> (visited on 06/03/2019).

- [13] Maxim Integrated Products, Inc. *HFAN-02.0.2: Laser Diode to Single-Mode Fiber Coupling Efficiency: Part 1 - Butt Coupling - Application Note*. 2008. URL: <https://www.maximintegrated.com/en/app-notes/index.mvp/id/1816> (visited on 06/04/2019).
- [14] Corning<sup>®</sup> *SMF-28<sup>®</sup> Ultra Optical Fiber*. 2014. URL: <https://www.corning.com/media/worldwide/coc/documents/Fiber/SMF-28%20Ultra.pdf> (visited on 05/24/2019).
- [15] H. Yoda and K. Shiraishi. “A new scheme of a lensed fiber employing a wedge-shaped graded-index fiber tip for the coupling between high-power laser diodes and single-mode fibers”. In: *Journal of Lightwave Technology* 19.12 (Dec. 2001), pp. 1910–1917. ISSN: 0733-8724.
- [16] T. Tamir et al. *Integrated Optics, Second Edition (Topics in Applied Physics)*. 2nd ed. Springer-Verlag, 1979. ISBN: 9780387096735.
- [17] P. K. Tien and R. Ulrich. “Theory of Prism–Film Coupler and Thin-Film Light Guides”. In: *JOSA* 60.10 (Oct. 1, 1970), pp. 1325–1337.
- [18] C. Palmer and E. Loewen. *Diffraction grating handbook*. 7th ed. Newport Corporation, 2014.
- [19] X. Chen et al. “Apodized Waveguide Grating Couplers for Efficient Coupling to Optical Fibers”. In: *IEEE Photonics Technology Letters* 22.15 (Aug. 2010), pp. 1156–1158. ISSN: 1041-1135.
- [20] Yunhong Ding, Haiyan Ou, and Christophe Peucheret. “Ultrahigh-efficiency apodized grating coupler using fully etched photonic crystals”. In: *Optics Letters* 38.15 (Aug. 1, 2013), pp. 2732–2734. ISSN: 1539-4794.
- [21] Mikael Antelius, Kristinn B. Gylfason, and Hans Sohlström. “An apodized SOI waveguide-to-fiber surface grating coupler for single lithography silicon photonics”. In: *Optics Express* 19.4 (Feb. 14, 2011), pp. 3592–3598. ISSN: 1094-4087.
- [22] Daniel Benedikovic et al. “Subwavelength index engineered surface grating coupler with sub-decibel efficiency for 220-nm silicon-on-insulator waveguides”. In: *Optics Express* 23.17 (Aug. 24, 2015), pp. 22628–22635. ISSN: 1094-4087.
- [23] Yannong Luo et al. “Low-loss two-dimensional silicon photonic grating coupler with a backside metal mirror”. In: *Optics Letters* 43.3 (Feb. 1, 2018), pp. 474–477. ISSN: 1539-4794.
- [24] Andrew Michaels and Eli Yablonovitch. “Inverse design of near unity efficiency perfectly vertical grating couplers”. In: *Optics Express* 26.4 (Feb. 19, 2018), pp. 4766–4779. ISSN: 1094-4087.
- [25] Yunfei Fu et al. “Efficient adiabatic silicon-on-insulator waveguide taper”. In: *Photonics Research* 2.3 (June 1, 2014), A41–A44. ISSN: 2327-9125.
- [26] Laurent Vivien et al. “Light Injection in SOI Microwaveguides Using High-Efficiency Grating Couplers”. In: *Journal of Lightwave Technology* 24.10 (Oct. 1, 2006), pp. 3810–3815.
- [27] R. Topley et al. “Planar surface implanted diffractive grating couplers in SOI”. In: *Optics Express* 22.1 (Jan. 13, 2014), pp. 1077–1084. ISSN: 1094-4087.

- [28] David B. Davidson. *Computational Electromagnetics for RF and Microwave Engineering*. 2nd ed. Cambridge University Press, 2010. ISBN: 9780521518918.
- [29] F. L. Teixeira. “Time-Domain Finite-Difference and Finite-Element Methods for Maxwell Equations in Complex Media”. In: *IEEE Transactions on Antennas and Propagation* 56 (2008), pp. 2150–2166.
- [30] S. Yip. *Handbook of Materials Modeling*. 1st ed. Springer, 2005. ISBN: 9781402032875.
- [31] Edmund J. F. Dickinson, Henrik Ekström, and Ed Fontes. “COMSOL Multiphysics<sup>®</sup>: Finite element software for electrochemical analysis. A mini-review”. In: *Electrochemistry Communications* 40 (Mar. 1, 2014), pp. 71–74. ISSN: 1388-2481.
- [32] *Detailed Explanation of the Finite Element Method (FEM)*. URL: <https://www.comsol.com/multiphysics/finite-element-method> (visited on 06/05/2019).
- [33] John D. Joannopoulos. *Photonic crystals: molding the flow of light*. 2nd ed. Princeton University Press, 2008. ISBN: 978-0-691-12456-8.
- [34] COMSOL. *An Introduction to the Theory of Electromagnetic Waves*. URL: <https://www.comsol.com/multiphysics/electromagnetic-waves-theory> (visited on 06/05/2019).
- [35] A. I. Arbab. “Complex Maxwell’s equations”. In: *Chinese Physics B* 22.3 (Mar. 2013). ISSN: 1674-1056.
- [36] *The COMSOL<sup>®</sup> Software Product Suite*. COMSOL Multiphysics<sup>®</sup>. URL: <https://www.comsol.com/products> (visited on 01/10/2020).
- [37] *Guide to Frequency Domain Wave Electromagnetics Modeling*. COMSOL Multiphysics. URL: <https://www.comsol.com/blogs/guide-to-frequency-domain-wave-electromagnetics-modeling/> (visited on 06/08/2019).
- [38] *Wave Optics Software for Analyzing Micro- and Nano-Optical Devices*. COMSOL Multiphysics<sup>®</sup>. URL: <https://www.comsol.com/wave-optics-module> (visited on 11/23/2019).
- [39] *Integrate MATLAB<sup>®</sup> Code with COMSOL Multiphysics<sup>®</sup> Models*. URL: <https://www.comsol.com/livelink-for-matlab> (visited on 01/11/2020).
- [40] *MATLAB - MathWorks*. URL: <https://se.mathworks.com/products/matlab.html> (visited on 01/11/2020).
- [41] *Corning<sup>®</sup> SMF-28<sup>®</sup> Ultra Optical Fiber*. 2014. URL: <https://www.corning.com/media/worldwide/coc/documents/Fiber/SMF-28%20Ultra.pdf> (visited on 05/24/2019).
- [42] W. Bogaerts and S. K. Selvaraja. “13 - Silicon-on-insulator (SOI) technology for photonic integrated circuits (PICs)”. In: *Silicon-On-Insulator (SOI) Technology*. Ed. by Oleg Kononchuk and Bich-Yen Nguyen. Woodhead Publishing, Jan. 1, 2014. ISBN: 978-0-85709-526-8.
- [43] Edward D. Palik. *Handbook of Optical Constants of Solids*. Vol. Volumes 1-4. Academic Press Handbook. Academic Press, 1985. ISBN: 9780125444200.

- [44] *Using Perfectly Matched Layers and Scattering Boundary Conditions for Wave Electromagnetics Problems*. COMSOL Multiphysics. URL: <https://www.comsol.com/blogs/using-perfectly-matched-layers-and-scattering-boundary-conditions-for-wave-electromagnetics-problems/> (visited on 01/12/2020).
- [45] Pietro Mandracci. *Crystalline and Non-crystalline Solids*. InTech, June 29, 2016. 186 pp. ISBN: 978-953-51-2445-0.
- [46] Michael Quirk and Julian Serda. *Semiconductor manufacturing technology*. Vol. 1. Prentice Hall Upper Saddle River, NJ, 2001.
- [47] Norwegian Micro – and Nano Fabrication Facility. *PECVD*. URL: <https://www.norfab.no/technologies/deposition/ntnu-nanolab-2/pecvd/> (visited on 01/19/2020).
- [48] A. Misra and I. Fininie. “On the scribing and subsequent fracturing of silicon semiconductor wafers”. In: *Journal of Materials Science* 14.11 (Nov. 1, 1979), pp. 2567–2574. ISSN: 1573-4803.
- [49] Ismail Kashkoush and Ahmbd Busnaina. “Submicron Particle Removal Using Ultrasonic Cleaning”. In: *Particulate Science and Technology* 11.1 (Jan. 1, 1993), pp. 11–24. ISSN: 0272-6351.
- [50] Werner Kern Karen Reinhardt. *Handbook of Silicon Wafer Cleaning Technology, Third Edition*. 3rd ed. William Andrew, 2018. ISBN: 9780323510844.
- [51] Ting Xu et al. “Sub-diffraction-limited interference photolithography with metamaterials”. In: *Optics Express* 16.18 (Sept. 1, 2008), pp. 13579–13584. ISSN: 1094-4087.
- [52] Stephen Thoms and Douglas S. Macintyre. “Investigation of CSAR 62, a new resist for electron beam lithography”. In: *Journal of Vacuum Science & Technology B* 32.6 (Oct. 31, 2014), 06FJ01. ISSN: 2166-2746.
- [53] *WieWeb software – The makers of CleWin*. URL: <https://wieweb.com/site/> (visited on 01/20/2020).
- [54] GeniSys GmbH. *Advancing the standard - BEAMER*. URL: <https://genisys-gmbh.com/beamer.html> (visited on 01/20/2020).
- [55] GeniSys GmbH. *Advancing the standard - TRACER*. URL: <https://genisys-gmbh.com/tracer.html> (visited on 01/20/2020).
- [56] Laurent Vivien and Lorenzo Pavesi. *Handbook of Silicon Photonics*. Google-Books-ID: lypGfgJqSM8C. CRC Press, Apr. 26, 2013. 855 pp. ISBN: 978-1-4398-3610-1.
- [57] Norwegian Micro – and Nano Fabrication Facility. *ICP-RIE*. URL: <https://www.norfab.no/technologies/deposition/ntnu-nanolab-2/pecvd/> (visited on 01/21/2020).
- [58] *NTNU NanoLab - Cleanroom*. URL: <https://www.ntnu.edu/nano/nanolab> (visited on 01/21/2020).
- [59] Robert Sproull, Richard Lyon, and Stephen Trimberger. *The Caltech Intermediate Form for LSI Layout Description*. URL: <https://resolver.caltech.edu/CaltechCSTR:1980.2686-tr-1980> (visited on 01/20/2020).



- [60] ALLRESIST GmbH. *AR-P 6200 (CSAR 62)*. June 17, 2014. URL: <https://www.allresist.com/csar-62-ar-p-6200/> (visited on 01/23/2020).
- [61] ALLRESIST GmbH-Strausberg Germany. *ALLRESIST GmbH - Strausberg, Germany*. Allresist EN. July 26, 2007. URL: [www.allresist.com/prozesschemikalien-ar-600-50-51-55-56/](http://www.allresist.com/prozesschemikalien-ar-600-50-51-55-56/) (visited on 02/03/2020).
- [62] Emil Wolf Max Born. *Principles of optics*. 7th. Cambridge University Press, 1999. ISBN: 9780521642224.
- [63] K. D. Vernon-Parry. “Scanning electron microscopy: an introduction”. In: *III-Vs Review* 13.4 (July 1, 2000), pp. 40–44. ISSN: 0961-1290.
- [64] Joseph I. Goldstein et al. *Scanning Electron Microscopy and X-Ray Microanalysis*. Google-Books-ID: D0LDwAAQBAJ. Springer, Nov. 17, 2017. 554 pp. ISBN: 978-1-4939-6676-9.
- [65] Thorlabs. *Tunable Laser Kit User Guide*. 2014. URL: [https://www.thorlabs.com/\\_sd.cfm?fileName=21038-D02.pdf&partNumber=TLK-L1550M](https://www.thorlabs.com/_sd.cfm?fileName=21038-D02.pdf&partNumber=TLK-L1550M) (visited on 02/05/2020).
- [66] M. Passoni et al. “Grating couplers in silicon-on-insulator: The role of photonic guided resonances on lineshape and bandwidth”. In: *Applied Physics Letters* 110.4 (Jan. 23, 2017), p. 041107. ISSN: 0003-6951.
- [67] Dirk Taillaert et al. “Grating Couplers for Coupling between Optical Fibers and Nanophotonic Waveguides”. In: *Japanese Journal of Applied Physics* 45.8 (Aug. 4, 2006), p. 6071. ISSN: 1347-4065.
- [68] Jing Xu, Xin Jin, and Yanli Zhao. “Apodized fully-etched surface grating coupler using subwavelength structure for standard silicon-on-insulator waveguide”. In: *Optical and Quantum Electronics* 49.4 (Mar. 22, 2017), p. 158. ISSN: 1572-817X.
- [69] MathWorks Nordic. *Smoothing Splines - MATLAB & Simulink*. URL: <https://se.mathworks.com/help/curvefit/smoothing-splines.html> (visited on 02/12/2020).
- [70] Jens Høvik and Astrid Aksnes. “A study on the optical properties of amorphous silicon”. Poster. Nano@NTNU symposium 2017. 2017. URL: <https://app.cristin.no/results/show.jsf?id=1545273> (visited on 02/14/2020).
- [71] COMSOL® Learning Center. COMSOL Multiphysics®. URL: <https://www.comsol.com/learning-center> (visited on 10/31/2019).
- [72] COMSOL Inc. *Wave Optics Module User’s Guide*. 2019. URL: <https://doc.comsol.com/5.4/doc/com.comsol.help.woptics/WaveOpticsModuleUsersGuide.pdf> (visited on 12/08/2019).

